Mechanical behaviour of additively manufactured lattice structures

by
Georgino Kaleng Tshikwand

Thesis presented in partial fulfilment of the requirements for the degree of Master of Engineering (Mechanical) in the Faculty of Engineering at Stellenbosch University

Supervisor: Prof. Deborah Clare Blaine
Co-supervisor: Prof. Anton du Plessis

March 2020

Stellenbosch University https://scholar.sun.ac.za

Declaration

By submitting this thesis electronically, I declare that the entirety of the work contained therein is my own, original work, that I am the sole author thereof (save to the extent explicitly otherwise stated), that reproduction and publication thereof by Stellenbosch University will not infringe any third party rights and that I have not previously in its entirety or in part submitted it for obtaining any qualification.

Date: March 2020

Copyright ©2020 Stellenbosch University

All rights reserved.

Stellenbosch University https://scholar.sun.ac.za

ABSTRACT

Lattice structures are open-cell, strut-based structures made up of unit cells that are tessellated in 3 orthogonal directions. Depending on the physical design of the unit cell, the lattice structure can be designed for customized stiffness, strength, and specific strain energy absorption. This allows for the design of lightweight, load-bearing structures, suitable for functional engineering applications.

5 X 5 X 5 octet-truss and diamond lattice structures of a specified relative density were designed using equations that relate the relative density to the strut dimensions. Computer-aided design (CAD) models of the structures were created and used to produce these lattice structures of Ti6AL4V using the additive manufacturing (AM) technique: laser powder bed fusion (L-PBF).

Finite element analysis (FEA) was used to simulate the uniaxial compression of the lattice structures, yielding predictions for the stress distribution in the lattice struts, and allowing for the prediction of the deformation and failure modes. 3D solid and 1D beam elements were used for this purpose. A prediction of the global mechanical properties and deformation mechanism of the lattice structures was established for both types and compared. A comprehensive flowchart describing the FEA approach taken in order to predict the mechanical behavior of L-PBF lattice structures is provided.

Mechanical uniaxial compression of the as-built lattice structures was conducted. Global mechanical properties were determined from the load-deformation data. The progressive collapse of struts under the load was analyzed in order to categorize the failure as stretch- or bending-based.

Micro-computed tomographic (μCT) analysis of the as-built structures showed that the struts were thicker as compared to the CAD structures. Thus new CAD models were created with the strut thickness correlating to the actual average dimension. This resulted in improved prediction of the mechanical response of the as-built structures.

A comparison of the FEA predictions and the experimentally measured mechanical properties of the lattice structures was carried out. It was determined that both the 3D solid and 1D beam structures predicted the actual mechanical properties of the octet-truss lattice structure within an error margin of less than 25 %. However, for the diamond lattice structure, only the 3D solid structure predicted the actual mechanical properties with an error margin of less than 20 %.

A study of the stress distribution across individual struts in the structure was used to explain the deformation mechanisms observed in the respective lattice structures. The octet-truss structure was found to deform by a combination of 45° and 135° shear bands caused by the stretching of the horizontal struts in those planes, whereas the diamond lattice structure was found to deform by 45° shear bands caused by strut bending.

Stellenbosch University https://scholar.sun.ac.za

UITTREKSEL

Roosterstrukture is oopsel strukture waarvan stutte die basis struktuur maak, wat van eenheidselle wat in 3 ortogonale rigtings getëel word. Afhangend van die fisieseonterwerp van die eenheidsel, kan die roosterstruktuur pasgemaak word vir styfheid, sterkte en spesifieke opname van spanningenergie. Dit maak voorsiening vir die ontwerp van liggewig, las-draende strukture, geskik vir funksionele ingenieurswese-toepassings.

5 x 5 x 5 Octetstut- en diamant-roosterstrukture van ’n spesifiseerde relatiewe digtheid is ontwerp met behulp van vergelykings wat die relatiewe digtheid met die stutafmetings verwant. Rekenaargesteunde ontwerp (CAD) modelle van die strukture is gebou en gebruik om hierdie roosterstrukture te vervaardig uit Ti6Al4V, met die gebruik van die bytoevoeging vervaardiging (AM) tegniek: laserpoeierbedversmelting (L-PBF).

Eindige elementanalise (EEA) is gebruik om eenassige samedrukking van die roosterstrukture te simuleer, wat voorspellings vir die spanningsverspreiding in die roosterstutte en toelaat dat die deformasie en failingsmodusse voorspel kan word. 3D-soliede en 1D-balk-elemente is vir hierdie doel gebruik. Vir beide tipes is 'n voorspelling van die globale meganiese eienskappe en vervormingsmeganisme van die roosterstrukture vasgestel en vergelyk. 'n Omvattende vloeidiagram word gegee wat die EEA-metodiek wat geneem word om die meganiese gedrag van L-PBF-roosterstrukture te voorspel.

Meganiese eenassige samedrukking van die vervaardigde roosterstrukture is uitgevoer. Globale meganiese eienskappe is bepaal. Die opeenvolgende inval van die stutte onder die las is geanaliseer om die faling as op strek- of buig-belasting te kategoriseer.

Mikro-berekende tomografiese analise van die vervaardigde strukture het getoon dat die stutte groter was in vergelyking met die CAD strukture. Dus is nuwe CAD modelle gebou waar die stut dikte soortgelyk as die werklike gemiddelde afmeting gestel word. Dit het die voorspelling van die meganiesegedrag van die vervaardigde strukture verbeter.

'n Vergelyking van die EEA-voorspellings en die eksperimenteel gemete meganiese eienskappe van die roosterstrukture is uitgevoer. Daar is bepaal dat beide die 3D-soliede en 1D-balkstrukture die werklike meganiese eienskappe van die octet-stut-roosterstruktuur voorspel het binne 'n waarnemingsfout van minder as 25%. Vir die diamantroosterstruktuur het slegs die 3D-soliede struktuur egter die werklike meganiese eienskappe voorspel met 'n waarnemingsfout van minder as 20%.

'n Studie van die spanningsverspreiding oor individuele stutte in die struktuur is gebruik om die vervormingsmeganisme wat in elkeen van die strukture waarneem is te verduidelik. Daar is gevind dat die octet-stut struktuur vervorm is deur 'n kombinasie van skuifbande van 45 ° en 135 °, wat

Stellenbosch University https://scholar.sun.ac.za

veroorsaak word deur die strek van die horisontale stutte in daardie vlakke, terwyl dit gevind is dat die diamantroosterstruktuur vervorm is deur skuifbande van 45 ° wat veroorsaak is deur stutbuiging .

Stellenbosch University https://scholar.sun.ac.za

ACKNOWLEDGEMENTS

I would like to thank the almighty God for allowing me to pursue my dreams. For my mom, Mweny Kaleng Esperance, whose love and support has nurtured me and raised me in the man I am today.

For my brothers and sisters, Sandra Katshung, Heureux Katshung, Edouard Mpialu, Leandrine Mweny, Leandro Fwamba, and Victoire Mbombo, whose brotherly and sisterly love and prayers have contributed to my growth as a man.

For my dad, Timothee Mpialu, and my stepdad, Fwamba Kasongo, whose support has contributed to my growth as a man.

For two supportive supervisors in Prof Deborah Blaine and Prof. Anton du Plessis, whose contribution to the completion of this research project is invaluable.

For the fellow research colleagues from the Materials Engineering research group and the CT facility for continued and mutual support.

For everybody who has contributed to my development as a researcher.

For the Department of Science and Innovation that gave me a bursary under the Collaborative Program for Additive Manufacturing (CPAM).

Stellenbosch University https://scholar.sun.ac.za

TABLE OF CONTENTS

Stellenbosch University https://scholar.sun.ac.za

Stellenbosch University https://scholar.sun.ac.za

Stellenbosch University https://scholar.sun.ac.za

Stellenbosch University https://scholar.sun.ac.za

LISTS OF FIGURES

Stellenbosch University https://scholar.sun.ac.za

Stellenbosch University https://scholar.sun.ac.za

Stellenbosch University https://scholar.sun.ac.za

Stellenbosch University https://scholar.sun.ac.za

LIST OF TABLES

Stellenbosch University https://scholar.sun.ac.za

Stellenbosch University https://scholar.sun.ac.za

1 Introduction

This study concerns the analysis of the mechanical behavior of additively manufactured (AM), by selective laser melting, Ti6Al4V octet-truss, and diamond lattice structures. The behavior of these structures is evaluated using standard finite element analysis methods implemented in commercially available FEA software packages, as well as experimentally through compression testing. A review of the prediction of mechanical properties of lattice structures and the motivation of the present study is presented below. The objectives, scope, and limitations of this study are also given below.

1.1 Background and motivation

Lattice structures are cellular structures classified under the open-cell foam category from the study of Ashby and Gibson [1]. They are strut-based and can be designed and produced as a unit through additive manufacturing techniques. Their use is rapidly expanding due to their exceptional functional properties, such as high strength and stiffness to weight ratios, as well as high strain energy absorption [2].

The use of lattice structures in lightweight, load-bearing applications is quickly expanding. Biomedical, aerospace and automotive industries are beginning to consider these structures to optimize material economy and to have control of their functional properties [3,4].

Lattice structures are frequently produced through AM techniques that build highly intricate structures through the fusion of metal powder in a layer by layer fashion. This helps to maintain structural integrity as the material is continuously connected throughout the lattice structure. However, these processes can induce many imperfections in the final produced structure. This can result in the as-built part exhibiting measurable differences from the original CAD model used for the build. The quantification and qualification of these production-related imperfections, and their influence on the functional properties of the produced structure, are an active field of research [5,6]. Micro-computed tomographic (Micro-CT) analysis of the as-built structure helps in the determination of different parameters, such as the as-built density, final geometric dimensions, pores and defects, and surface roughness. Some other studies have investigated the mechanical behavior of Ti6Al4V octet-truss and diamond lattice structures and reported on the effect of the production techniques on these properties [2–5].

Mathematical relationships describing the mechanical properties of porous structures are usually derived through experimentation, linking effective properties to the relative density, equivalent to the ratio of the mass of struts to total unit cell volume [11]. However, these empirical equations are often over-simplified formulations and result in inaccurate, limited predictions that are not suitable for critical engineering applications [7].

Stellenbosch University https://scholar.sun.ac.za

Numerical methods such as finite element analysis (FEA) offer the opportunity to model the mechanical response of structures in more detail, providing information such as the predicted deformation of, and stress distribution in lattice structures under compression. These methods transform the differential equations for force equilibrium, constitutive relations, and compatibility equations into systems of linear or nonlinear equations, that are then solved by computers. In order to achieve an acceptable prediction of mechanical behavior, the structure is discretized into many elements. This leads to higher computational power and time.

The accuracy of the prediction of the FEA model depends on a wide range of factors, including the choice of the FEA approach, level of mesh discretization, and the accuracy of the CAD model used to represent the physical structure. Choosing appropriate FEA approaches for modeling the mechanical response of lattice structures is complex. Factors such as the lattice structures are comprised of a network of long, thin struts, that small deviations of the as-built structure from the original CAD model could significantly influence the response, as well as the large deformations that occur during deformation of the structure as a whole add to the complexity.

There are no international testing standards for lattice structures, therefore the existing few standards for porous metals are used to conduct mechanical compression testing on the lattice structures [12]. Ongoing research work in the investigation of the mechanical properties of lattice structures will lead the way into better setting up testing standards for these structures in the future. Such standards will consider the various production bound imperfections and allow to better formulate FEA models that better represent the produced structures.

This project builds on the existing knowledge base regarding the mechanical behavior of AM Ti6Al4V octet-truss and diamond lattice structures. Different FEA approaches were implemented in order to determine their suitability in terms of accurately and efficiently predicting the mechanical response of these lattices under compression. The dominant deformation mechanisms of the two lattice designs that were chosen were confirmed both experimentally and using FEA. A clear assessment of the stress and strain distributions of the selected lattice structures was studied and reported in this project.

1.2 Objectives

The main objective of this research study was to evaluate feasible FEA approaches that can be used to predict the mechanical behavior of octet-truss and diamond lattice structures, built from Ti6Al4V powder using the L-PBF AM technique. As there are numerous FEA approaches available, the relative efficiency and accuracy of different approaches were assessed. This was accomplished by performing the following tasks:

Stellenbosch University https://scholar.sun.ac.za

- Design two lattice structures, based on the octet-truss and diamond unit cells, that are suitable for manufacture using L-PBF and that are of similar relative density (~20%) and fixed unit cell size;
- Manufacture the lattice structures using L-PBF according to the design and evaluate the accuracy of the as-built dimensions by using x-ray computed tomography;
- Conduct non-linear static FEM analysis to simulate the compression of lattice structures, using two different meshing techniques – 1D beam and 3D solid elements;
- Conduct mechanical compression testing on the lattice structures and record the load-deformation response;
- Use the mechanical testing results in order to determine the global mechanical properties of the respective lattice structures, as well as to observe the dominant deformation mechanisms that lead to strut failure under compression;
- Compare the FEA simulation results and the compression testing results in order to evaluate the suitability and capability of the FEA approaches in the prediction of the mechanical behavior of the lattice structures.

1.3 Scope and limitations

The present work is limited to the assessment of the suitability of two FEA approaches in the prediction of the mechanical behavior of lattice structures, one using beam elements and the other using 3D solid elements in order to discretize the mesh. FEA compression simulations were conducted using ANSYS academic research Mechanical and CFD (structural/LS-Dyna). The study was focused on two cubic lattice structures, the octet-truss, and diamond unit cell structures. For the FEA simulations, an elastic-plastic material model was used, and no damage model was considered. An L-PBF machine was used to produce the structures from Ti6Al4V. X-ray computed tomographic analysis of produced structures was conducted but limited to an analysis of the dimensions of the as-built lattice structures. No image-based simulations from micro-CT images were included in the scope of this work.

Stellenbosch University https://scholar.sun.ac.za

2 Literature review

Many studies have focused attention on the investigation of the mechanical properties of lattice structures produced through laser powder bed fusion (L-PBF) due to the huge potential of these structures. Lattice structures are desired in industries requiring lightweight, loadbearing capability. Most lattice structures are designed through the tessellation of unit cells. The unit cell design can be manipulated in order to control properties such as the density, the elastic response and the strength of the lattice structure. A review of the previous studies on the production of lattice structures, their mechanical properties, deformation mechanisms, heat treatment processes, and material behavior are presented in this chapter.

2.1 Additive manufacturing

2.1.1 Introduction

Subtractive manufacturing (SM), where a component is manufactured through the removal of material until the final part is obtained, is a well-established technology. A common drawback of SM is high material wastage.

Metal additive manufacturing, through L-PBF, is a process of building a component through the fusion of metal powder, layer by layer, until the complete part is produced [13]. This process achieves a great amount of material economy through the reduction of metal scrap. Additive manufacturing (AM) has introduced a new perspective to the manufacturing industry by allowing the designer to build intricate parts for a range of different applications, such as medical, aerospace, and automotive [14].

Many engineering applications have started to rely on AM to produce certain parts that require customization, which can be costly and time-consuming to produce using conventional manufacturing techniques [15]. AM has significantly increased the ease and economy of complex part manufacture, especially showing great potential with biomimetic design approaches [16].

Before AM became a viable manufacturing technique, complex parts were typically produced through assemblies of multiple sub-parts that were manufactured by conventional methods. Conventional manufacturing techniques are suitable for mass production of simple medical implants, and a range of simple automotive and aerospace components. However, when the geometry of these parts becomes more complex or must be produced by the assembly of two or three component parts, advanced manufacturing techniques must be applied. One concern with conventional techniques is the structural performance and integrity of the assembled parts. Assembled parts used in the automobile and aerospace industries are subjected to vibrations which can cause these components to come loose after a certain number of operation cycles, resulting in failure. An assembled part has a limited life span compared to a non-assembled part [17]. AM technologies

Stellenbosch University https://scholar.sun.ac.za

allow the production of these vibration-sensitive parts as a unit thereby increasing their resistance to vibrations and their life span.

AM technologies such as selective laser melting (SLM), selective laser sintering (SLS), and electron beam melting (EBM) are currently being used to manufacture intricate parts. Selective laser melting (SLM) is the most commonly used of the above-mentioned AM technologies. A description of the SLM technology is presented in the next section.

2.1.2 Selective laser melting process and applications

Selective laser melting is one of AM technologies that is mostly used in the production of parts with complex geometry.

Figure 1 shows the operating principle of the technology. An SLM machine consists of a high-power laser source, a scanning system, a chamber with metal powder, a roller, and a substrate or builds plate.

The SLM process consists of a 3D CAD that is converted into a stereolithographic file (.stl file). This file is an SLM software readable format that describes the surface (2D slice) geometry of the 3D CAD model and provides coordinates to the laser scanning system. This file is the input to the SLM system.

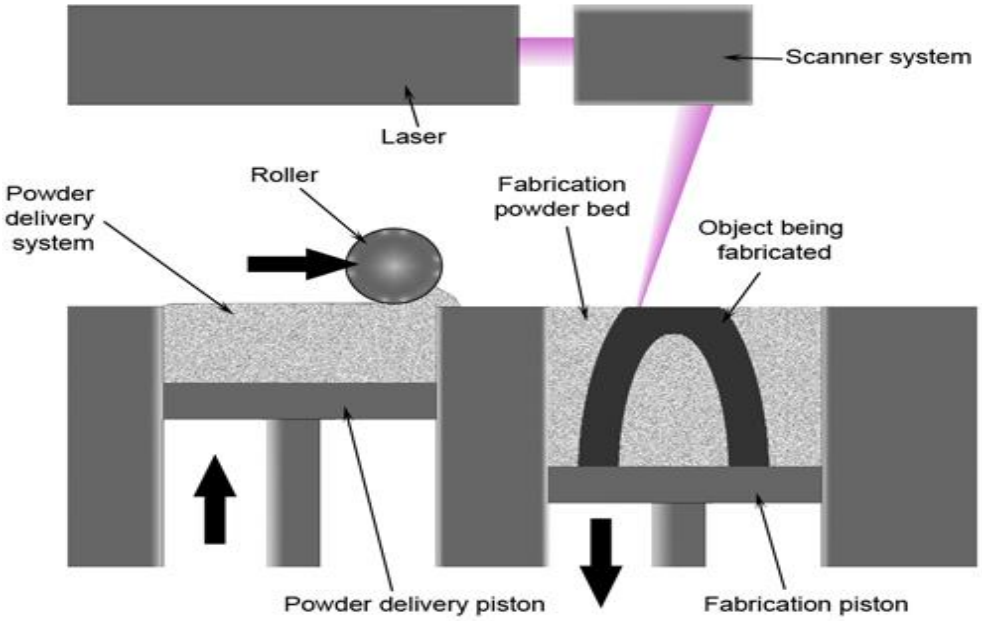

Figure 1: Selective laser melting process

©: https://www.spilasers.com/

Stellenbosch University https://scholar.sun.ac.za

The metal powder from the powder chamber is spread over the build plate with the help of a servo-controlled roller. A high-power laser-guided by the scanning system fuses a 2D slice of the part by selectively melting the metal powder. The build plate moves down to an amount equal to the thickness of one layer. Another layer of metal powder is spread over the fused slice and the same process is repeated until the part is built.

This process takes place in a controlled environment inside the SLM machine. Often time, parts with overhanging features are built with support structures that are removed after the build process.

SLM find application in many industries such as biomedical, aerospace, automotive, and manufacturing. In the medical industry, SLM is used to produce various types of implants. Examples of medical implants are dental restoration, hip implants, and surgical instruments. In the aerospace industry, lightweight structures and fuel injectors can be produced. In the automotive industry, the prototype of valves can be produced through SLM. In the manufacturing industry, high precision tooling and molds can be produced [18].

SLM is being considered as the future manufacturing technology for products requiring less processing time and low production cost when compared to the conventional machining processes. Hollow to high intricate structures requiring customization with adapted properties can be produced through SLM.

Despite all the benefits SLM offers, there are some disadvantages that need to be considered while producing a component through SLM. The influence that SLM has on the mechanical properties is discussed next.

2.1.3 SLM influence on mechanical properties

During the additive manufacturing process, some metal powders fail to fuse due to inadequate and non-optimal process parameters and this produces pores, flaws, and defects in the struts of the produced structure. This raises the importance of quantification and analysis of these pores, flaws, and defects. This helps to understand the influence they have on the mechanical properties of the structure. This quantification can be achieved with the help of micro CT-scanning.

An outline of the different pore morphologies and extents due to typical process parameter imperfections is presented in [19]. Strut porosity typically has a negative effect on mechanical properties. However, the optimization of process parameters can minimize the formation of pores.

These induced imperfections are usually not considered when defining the material properties to set up the stiffness matrix for FEA. This is a possible source of the deviation between the FEA simulations and the mechanical compression results. The FEA considers a perfect CAD design whereas, for

Stellenbosch University https://scholar.sun.ac.za

the mechanical testing, the test sample has additional features inherent to the SLM process.

Strut waviness, surface roughness, and strut pores induced during the manufacturing process lead to a difference in the cross-section between the designed CAD structure and the SLM produced structure. This not only affects the functional properties of the produced structure but also the reliability of FEA approximations to predict the mechanical properties of these structures. Therefore, the quantification of the strut waviness and surface roughness, and strut pores is essential in order to relate them to possible deviations between the mechanical testing and FEA results.

Studies on the treatment of surface roughness and strut waviness have been conducted to understand how their influence can be minimized. Pyka et al. showed how reducing surface roughness features of SLM Ti6Al4V lattice structures influenced the mechanical response of these structures [6]. This was attributed to the removal of sharp surface crack initiation sites which should improve resistance to failure; however, the etching procedure used to remove the rough surface features also reduced the cross-section dimensions of the struts, which had resulted in reduced strength and stiffness of the structure. Figure 2 shows the result of the protocol introduced in the same study to reduce the strut waviness and surface roughness. The SLM part was chemically etched to remove the powder particles on the strut surface and it was polished through an electro-chemical process.

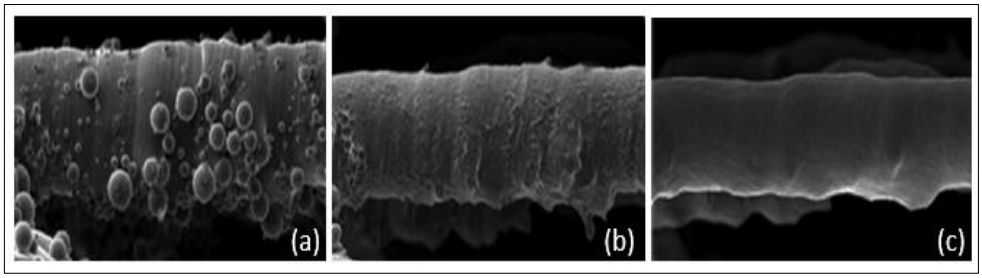

Figure 2: SEM micrographs of the SLM strut (a) as-produced (b) after chemical etching (c) after electrochemical polishing [6].

Figure 3 shows the effect of surface modification of the SLM structure on its mechanical properties. A significant decrease in both the compressive strength and stiffness was observed.

Stellenbosch University https://scholar.sun.ac.za

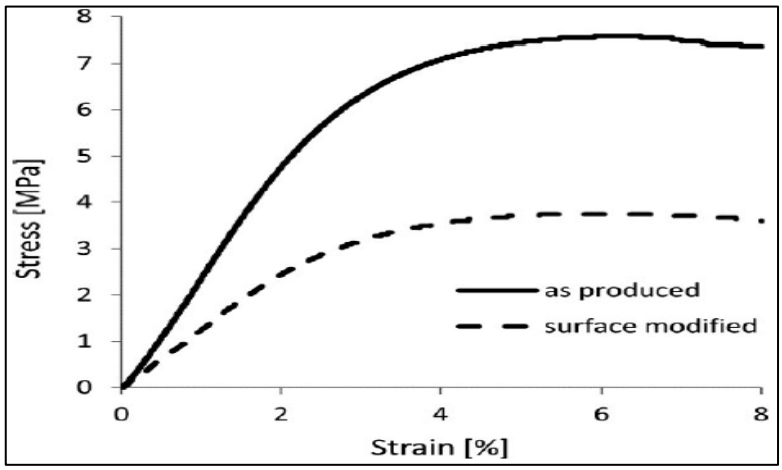

Figure 3: Stress-strain diagram of the SLM part before and after surface modification [6]

Other influences on the properties of SLM produced materials have been studied, such as post-SLM heat treatment. Vrancken conducted a comparative study between the heat treatment of an SLM Ti6Al4V specimen (SLM material) and a wrought Ti6Al4V specimen (reference material) [20]. An acicular martensitic microstructure is observed in the untreated SLM parts [6,7] due to the high operating temperature and fast cooling rate.

Figure 4 shows the stress-strain diagram of the SLM Ti6Al4V specimen and the wrought specimen before heat treatment. A lower Young's modulus, higher tensile strength, and lower fracture strain were observed for the SLM

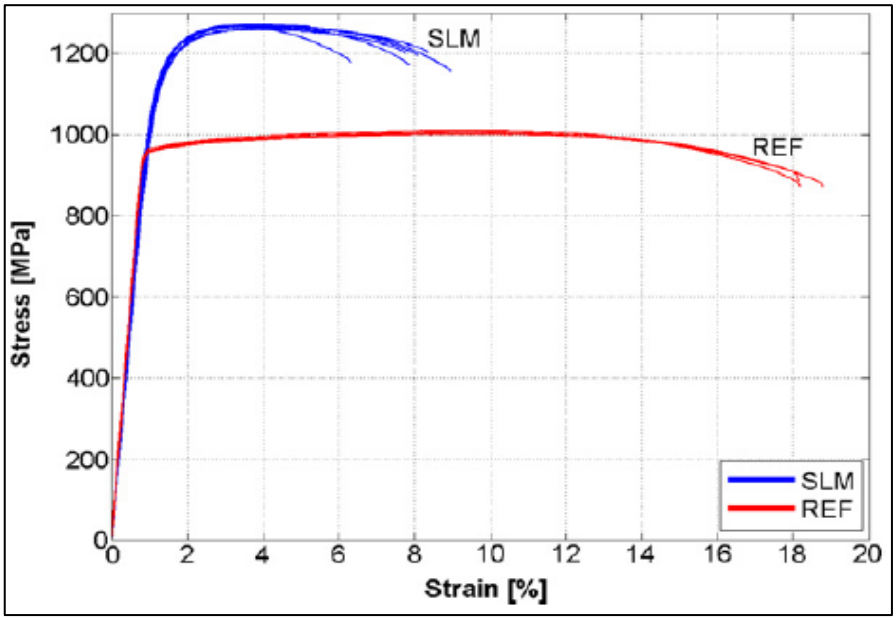

Figure 4: Stress-strain diagram for the untreated SLM specimen and wrought specimen (reference material) [20]

Stellenbosch University https://scholar.sun.ac.za

material as compared to the reference material. Upon heat treatment, it is reported that heating the as-built SLM specimen below the β-transus temperature (995^{o} C) decomposed the martensitic phase into a lamellar α-β phase [20].

From Figure 5, it can be seen that the heat treatment of the Ti6Al4V specimen influences its mechanical properties. When the specimen is manufactured through the SLM process, it has high strength and a lower failure strain (see Figure 4).

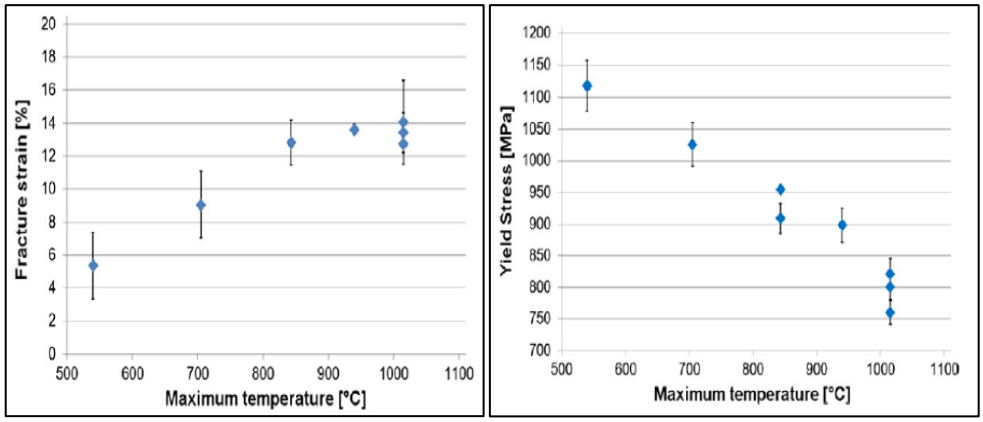

Figure 5: Mechanical properties as a function of heat treatment temperatures [20]

However, upon heat treatment, the yield strength of the SLM specimen decreases as the temperature increases and the failure strain increases (see Figure 5). This increases the ductility of the SLM material. This was also observed in [23].

The SLM process also induces residual stresses in parts due to the high thermal stresses. Mercelis et al. studied the SLM process and its effect on inducing residual stresses in parts [24]. Residual stresses are not desirable in the application of load-bearing structures and medical implants. This is because residual stresses reduce the strength of the structure and can cause the part to warp during the build process causing build failure and damage to the system. In the same study, two sources of residual stresses induced in SLM parts were determined. The first being the thermal gradients developed around the laser beam during the heating process of the powder. This process, as it would be expected, tends to expand the layer being heated but the powder material around it prevents this expansion and induce in it, compressive strain. The second source being the cooling process. Figure 6 shows how, during the cooling process, the top layer tends to contract, and this contraction is resisted by the surrounding material thereby inducing tensile stresses in it.

Stellenbosch University https://scholar.sun.ac.za

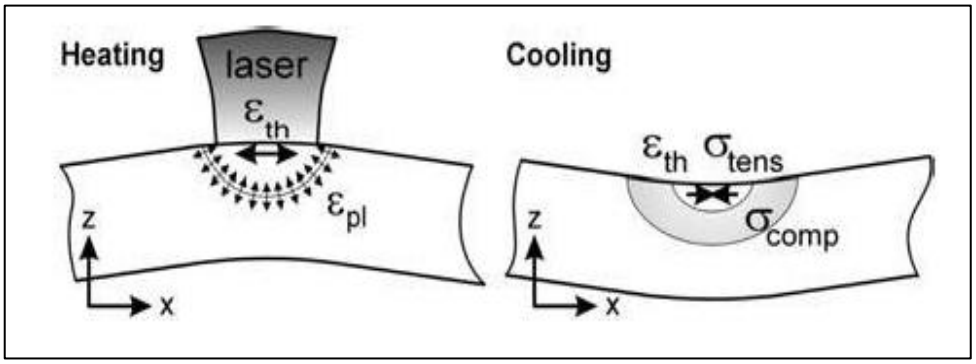

Figure 6: Sources of residual stresses during the selective laser melting and selecting laser sintering processes [24]

As the part is being built, from the first bottom layer to the final top layer, the process seen in Figure 6 repeats itself throughout the entire build. The intermediate layer during the build process induces tensile stress on the bottom layer which tends to contract upon cooling, compressive stress on the top layer which tends to expand under thermal stresses from the laser beam.

Relieving these stresses is highly important in load-bearing and medical applications. Processes followed in [25] can be employed to relieve the residual stresses in the SLM printed structures.

2.2 Lattice structures

Lattice structures are gaining interest in the manufacturing industry owing to the ability to control their functional properties. The control over design that design engineers have with regards to the density and mechanical properties make the investigation of lattice structures an interesting topic for many research studies.

2.2.1 Introduction

Lattice structures are structures with controlled porosity and mechanical properties. They are typically constructed by repeating a specific unit cell (building block) in all 3 dimensions. This results in a 3D cellular structure that is symmetric about all 3 axes. Lattice structures are classified under the “open cell foams” group because they mainly consist of a network of struts. This classification is a result of extensive research works conducted by Ashby and Gibson [1].

Due to the increased interest in their mechanical behavior, many unit cell types have been investigated to understand how they deform and behave when subjected to various loading conditions [12–14].

Figure 7 shows a list of unit cells used to build lattice structures that have been included in research studies to understand their mechanical behavior.

Stellenbosch University https://scholar.sun.ac.za

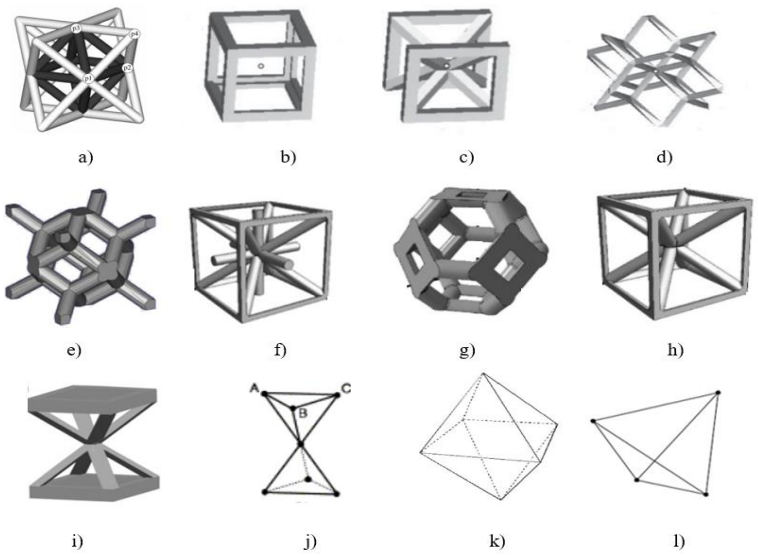

Figure 7: Examples of unit cell geometries: a) octet truss [27] h) b-c-d) G6 structure, G7 structure, Dode thin [4] e) rhombic dodecahedron [28] f-g-h) reinforced body-centered cubic (RBCC), body-centered cubic (BCC), kelvin structure [29] i) G7R structure [28] j) kagome structure [30] k) Octahedron [31] l) tetrahedral lattice [32].

2.2.2 Design of lattice structures

The design of lattice structures is mainly governed by its required functionality, for instance, whether the structure will be used for load-bearing, medical implant, or energy absorption. This will guide in the choice of the unit cell topology of the lattice structure.

The required mechanical properties and dominant deformation mechanism of the lattice structure are also factors that influence the choice of the unit cell topology. A wide variety of unit cells exists, based on their mechanical properties, deformation mechanisms and functional applications [4], [33].

A key concept in the design of lattice structures is the relative density, $\bar{\rho}$, which is the ratio of the density of the lattice structure, ρ_l, to the density of the solid material used to manufacture the lattice structure, ρ_s. The relative density corresponds to the ratio of the lattice strut volume, v_l, to the total lattice structure volume, v_{tot}.

Gibson and Ashby [34] have conducted extensive studies on naturally occurring irregular porous or cellular structures. They derived a relationship between the mechanical properties of the porous structure and the relative density as follows

$$\frac{E}{E_s} = \alpha \left(\frac{\rho}{\rho_s}\right)^n \quad (1)$$

Stellenbosch University https://scholar.sun.ac.za

$$\frac{G}{G_s} = \frac{3}{8}\alpha\left(\frac{\rho}{\rho_s}\right)^n \quad (2)$$

$$\sigma_{pl} = (0.25\ to\ 0.35)\,\sigma_{y,s}\left(\frac{\rho}{\rho_s}\right)^m \quad (3)$$

Where E and E_s are Young's modulus of the porous structure and that of the solid material from which the porous structure is made, respectively. G and G_s are the shear modulus of the porous structure and that of the solid material, respectively. σ_{pl} is the plateau stress and $\sigma_{y,s}$ is the yield stress of the solid material. n, α, and m are constants whose values vary between 1.8 and 2.2, 0.1 and 4, and 1.5 and 2, respectively.

When a porous structure is loaded in compression, the cell walls fail first, causing the cells to collapse in on themselves, resulting in the densification of the porous material. This initial failure occurs at the plateau stress and continues until the densification strain is reached. Beyond this strain, the collapsed and densified material behaves similarly to the solid material and a sharp rise in stress is observed [34].

Equation (1), (2), and (3) define the relationship between the porous structure's effective properties and relative density [34]. These relationships were developed based on the behavior of metal foams with > 50% porosity. They can be used to design porous structures with specific mechanical properties by controlling the relative density. Lattice structures can be viewed as porous structures. In doing so, geometric relationships between the dimension of the struts of the lattice structure and the relative density can be calculated by noting that the relative density is also the volume ratio of the lattice struts to unit cell volume. This opens the possibility to fine-tune the mechanical properties of porous structures and their additive manufacturing.

2.2.3 Yield behavior of porous structures

Solid (fully dense) parts yield by slip mechanisms which result in distortion (change of shape) of the part while its volume remains constant. A slip mechanism occurs as a result of the deviatoric stress (i.e. shear stress), while the incompressible property of the solid parts means that there is no volumetric change due to the hydrostatic stress. Details on the yield criteria and hardening laws of solid parts are presented in Appendix A.

Porous parts, however, are subjected to both shape and volume change during yielding due to their inherent porosity that is present both by design and due to the residual porosity induced by manufacturing [34]. As the porous material yields, cells collapse, causing both densification (volume change) and distortion. Thus, both the deviatoric and hydrostatic stresses control yielding in porous parts.

Stellenbosch University https://scholar.sun.ac.za

In order to define the elastic behavior of porous materials, a modification of the constitutive equations governing the elastic response of dense parts was developed that takes porosity into account [34]. This model describes the constitutive behavior of the porous material up to the point of yielding.

The Von Mises yield criterion dictates that yielding occurs when the Von Mises equivalent stress σ_e exceeds the yield stress, σ_y, of the material. This yield criterion is represented as a yield surface, Φ. The Von Mises yield criterion can be adjusted to define yielding in porous materials, by using an effective Von Mises equivalent stress $\hat{\sigma}_e$, that takes porosity into account, defined as,

$$\hat{\sigma}_e{}^2 = \frac{1}{\left(1+\left(\frac{\alpha}{3}\right)^2\right)}\left(\sigma_e{}^2 + \alpha^2\sigma_h^2\right) \quad (4)$$

Where σ_e is the Von Mises equivalent stress of the solid part, σ_h is the hydrostatic stress, as defined in Appendix A, and α is the aspect ratio defined by the shape of the yield surface. Thus, the effective Von Mises yield criteria surface for porous materials is defined as

$$\Phi \equiv \hat{\sigma}_e - \sigma_y \leq 0 \quad (5)$$

Equation (5) produces an elliptical yield surface, Φ, in the $\sigma_h - \hat{\sigma}_e$ stress space, where the aspect ratio of the ellipse, α, varies between 1.35 and 2.08.

The hydrostatic strength of the porous material is then given by

$$|\sigma_h| = \frac{\sqrt{\left(1+\left(\frac{\alpha}{3}\right)^2\right)}}{\alpha}\,\sigma_y \quad (6)$$

The yield surface shape Φ varies with respect to the plastic Poisson's ratio υ^p. The plastic Poisson's ratio is the ratio of the transverse strain to axial strain measured from a uniaxial compression test. It is given as,

$$\upsilon^p = \frac{\frac{1}{2}-\left(\frac{\alpha}{3}\right)^2}{1+\left(\frac{\alpha}{3}\right)^2} \quad (7)$$

The aspect ratio of the yield surface, α, can then be obtained from its relationship with υ^p as,

$$\alpha = 3\left(\frac{\frac{1}{2}-\upsilon^p}{1+\upsilon^p}\right)^{\frac{1}{2}} \quad (8)$$

Stellenbosch University https://scholar.sun.ac.za

The constant α determines the shape of the yield surface and therefore yielding of porous materials can be obtained.

The above equations were tested for the Alulight and Alporas structures successfully [34].

On the basis of the deformation and failure mechanisms of cellular structures, empirical equations determining the mechanical properties and yield criteria of cellular structures as a function of their relative density (including their inherent porosity), were derived. These are presented in Table 1.

Table 1: Mechanical properties of cellular structures [11]

Relative stiffness	Relative shear modulus	Elastic collapse stress	Plastic collapse stress	Brittle crushing strength
$\frac{E}{E_s} = a\,(\frac{\rho}{\rho_s})^2$	$\frac{G}{G_s} = \frac{3}{8}(\frac{\rho}{\rho_s})^2$	$\sigma_{el} = a_1\,(\frac{\rho}{\rho_s})^2$	$\frac{\sigma_{pl}}{\sigma_y} = a_2\,(\frac{\rho}{\rho_s})^{1.5}$	$\frac{\sigma_{cr}}{\sigma_{fs}} = a_3\,(\frac{\rho}{\rho_s})^{1.5}$
Proportionality constants				
$a = 2$ [35]		$a_1 = 0.05$	$a_2 = 0.3$	$a_3 = 0.2$

2.2.4 Additive manufacturing of lattice structures and their effects

The manufacture of lattice structures is now possible through laser powder bed fusion (L-PBF) technologies, a subset of additive manufacturing (AM). Technologies such as selective laser melting (SLM), selective laser sintering (SLS) and electron beam melting (EBM) are examples of powder bed fusion (PBF) technologies that are being used extensively in various industries. These manufacturing technologies allow a range of potential materials and products to be built, with varying mechanical properties and dimensional accuracy. One thing that all these technologies have in common is the ability to produce parts with intricate geometry such as lattice structures. Of these technologies, SLM has been used extensively to manufacture lattice structures.

Due to the layer by layer methodology of L-PBF technologies, lattice structures, and their geometric intricacies can be produced. Furthermore, certain properties of lattice structures can be obtained when they are built at certain angles. This gives the designer or the analyst a choice of features, such as the build direction and types of the unit cell, in order to design for specific functional properties of the lattice structure. The effects of build direction, unit cell direction, and different unit cell types for the same density, achievable through L-PBF technologies, have been widely researched.

Stellenbosch University https://scholar.sun.ac.za

Weißmann et al. [36] studied the effect of the unit cell orientation on the mechanical properties of scaffolds. The unit cell was rotated at 45^{o} and 90^{o} about the y-axis and about both the x and y-axes. The unit cell orientation resulted in different positioning of struts in the unit cell. Some strut positions resulted in an improvement of the structure properties while some show no difference as compared to the un-rotated unit cell.

Uniaxial mechanical compression was conducted on the SLM scaffolds to determine the mechanical properties. It was reported that the structure that reached the highest stiffness is the T1-I 0^{o} oriented structure with 26.3 GPa and the lowest stiffness being the 90^{o} and 45^{o} with 3.4 GPa. The lowest compressive strain was recorded in the T1 structure and the highest compressive strain in the T2 structure showing high ductility in the T2 orientations. These results give additional input in the understanding of the regular porous structure and the ability to tune their mechanical behavior to a specific application. This can be achieved either by varying the strut thickness, the pore size or, as is shown in this study, the unit cell orientation. Figure 8 shows the different cell orientations analyzed in the study.

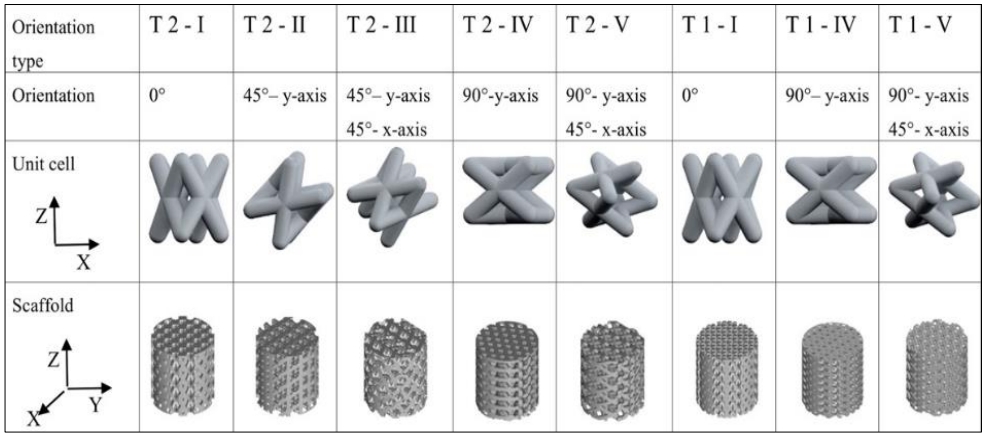

Figure 8: Unit cell orientation variations [36]

The effect of cell shape on the mechanical properties of porous structures of similar densities was studied by Li et al. [28]. The study shows different deformation mechanisms of structures made of three different unit cells: cube, G7, and rhombic dodecahedron. The structures were manufactured through EBM and compression testing was conducted on them.

It is reported that the deformation behavior can mainly be characterized around the plateau region of the stress-strain diagram obtained from the mechanical testing. A smooth plateau region was recorded for the G7 cell shape which is indicative of a predominantly bending deformation mode while the cubic and the rhombic dodecahedron cell shapes show a rough plateau region (stress fluctuations) which is indicative of a predominantly brittle deformation mode characterizing a high compressive strength as compared the G7 cell shape. Figure 9 shows the cell shapes of the study.

Stellenbosch University https://scholar.sun.ac.za

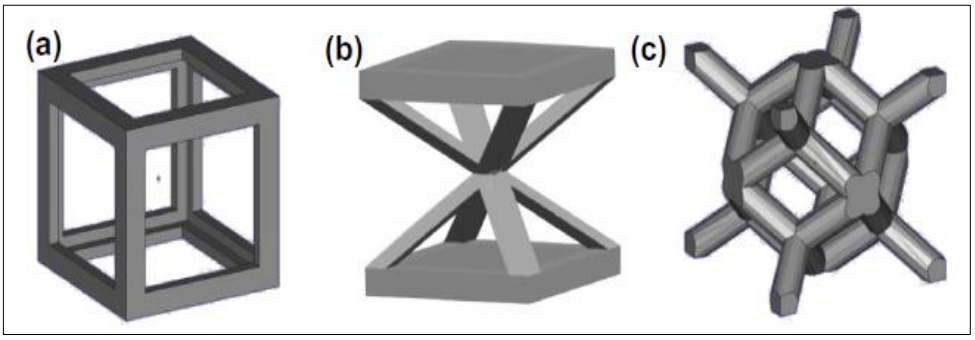

Figure 9: Cell shapes: cubic (a), G7 (b), and rhombic dodecahedron (c) [28]

Wauthle et al. studied the effect of the build direction and heat treatment processes of the SLM produced cylindrical diamond lattice structures [37]. The structures were built vertically, diagonally and horizontally. The samples were subjected to stress relief (SR) and hot isostatic pressing (HIP) heat treatments and some were tested as they were built (AB). The samples were then subjected to mechanical compression testing.

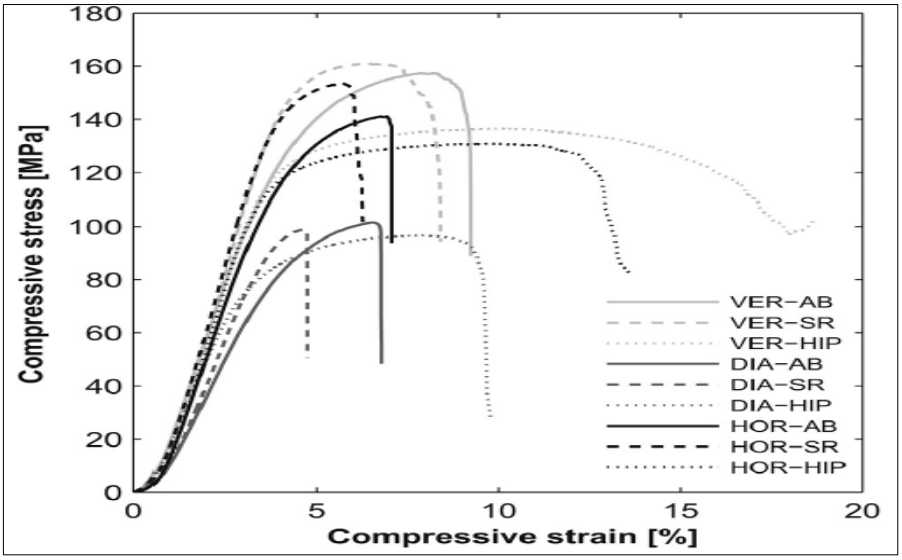

Figure 10: Stress-strain diagrams for different build directions and heat treatment conditions [37]

The results of the testing can be observed in Figure 10. When the as-built structures are heat-treated for the purpose of stress relief, they show a decrease in both the compressive strength and the compressive failure strain. However, when the structures were subjected to the HIP process, they show a high increase in the compressive strain, increasing the structures' ductility by a large margin and the process decreases the structure's strength considerably.

Stellenbosch University https://scholar.sun.ac.za

The effects of SLM on produced parts developed in section 2.1.3 apply to SLM lattice structures.

2.2.5 Mechanical behavior of lattice structures, bending and stretch dominated

Open-cell or strut-based structures like lattice structures can be classified based on their structural rigidity. It has been determined by many research studies that the stiffness and strength of these structures are governed by cell wall bending when subjected to all load conditions [11, 23,24].

Maxwell classified these structures based on the predominant cell wall failure mode [38]. The Maxwell criterion states that strut-based cells can either be stretch or bending dominated.

$$M = m - 3j + 6 \quad (9)$$

Where m and j are the numbers of struts and joints respectively.

Equation (9) is the Maxwell criteria, from which a unit cell is classified as bending-dominated when M is less than 0 and as stretch-dominated when M is approximately 0. A periodic structure made of stretch or bending dominated unit cells will necessarily have a stretch or bending dominated behavior.

Many studies have been conducted on the behavior of lattice structures to determine the characteristics of both stretch and bending-dominated structures [35, 36]. The consensus is that stretch-dominated structures are stiffer and stronger but show low fracture strain whereas bending dominated structures are less stiff and less strong but show high ductility.

2.3 Micro-computed tomography (CT) Scan

X-ray CT is now increasingly used in additive manufacturing as reviewed in [39]. As outlined in this review paper, besides geometrical measurements, it is also possible to directly simulate CT-scanned geometries using voxel-based structural simulation. This capability was used to compare different lattice structures previously [40]. The CT scanning processes are conducted following the guidelines and procedures set out in [27–30]. Deformation of micro-lattice structures can be imaged under load using CT scanning, showing in-situ deformation of lattice structures with struts nearing the limit of commercial L-PBF systems [39]. A short description of the scanning process and image analysis is given below.

Stellenbosch University https://scholar.sun.ac.za

2.3.1 CT-scanning process

The CT-scanning process involves the preparation and mounting of the sample, scanner set-up, scanning procedure, image reconstruction, and image visualization.

The sample can be scanned without any special preparation. The sample is mounted at a slight angle in a low-density material (floral foam, plastic bottles). The sample is so positioned to minimize the number of parallel surfaces to the x-ray beam. This allows the x-rays to better penetrate the surface and avoid image artifacts [44]. The sample should be mounted to allow no movement during the scanning process. This is to avoid blurry images.

Scanner set-up consists of selecting certain parameters such as the resolution of the image based on the sample size, the voltage, the voxel size, the distance of the detector from the x-ray source (FDD) and the distance of the sample from the x-ray source (FOD), etc. The optimal resolution for a sample of 100 mm width is 100 µm for a typical micro-CT system. For light metallic materials, the optimal voltage varies between 60 and 150 kV. More details about the scanner parameters can be found here [44].

Figure 11 shows a schematic of the scanning process. A sample is mounted and rotates as the x-ray beam projects 2D images of the sample onto the planar detector. This process continues until the sample has rotated 360° step by step. This results in a large number of 2D images. This number can be set before the scanning process.

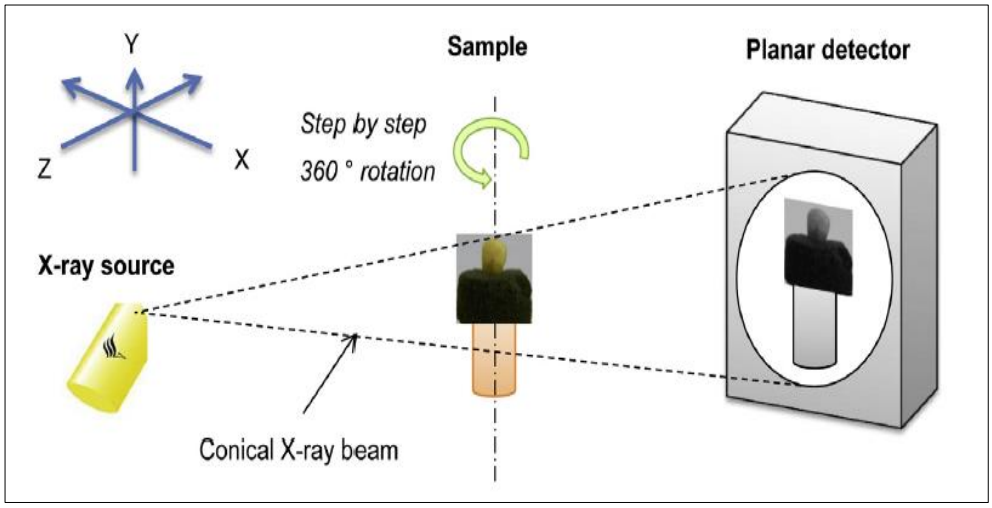

Figure 11: CT-scan set-up for sample scanning process [45]

Stellenbosch University https://scholar.sun.ac.za

2.3.2 Image analysis

2D images obtained during the scanning process can be reconstructed into a 3D volume

Analysis of 3D volumetric data such as wall thickness, porosity and nominal to actual comparison can be done using Volume graphics software.

2.4 Metallurgy, applications of Ti6Al4V

Ti6Al4V is the most commonly used titanium alloy in both the medical and aerospace industries for its attractive mechanical properties. Ti6Al4V is light in weight, has high strength and stiffness to weight ratios, good strength, and fatigue resistance even under high operating temperature and high corrosion resistance.

For the medical industry, Ti6Al4V is found to be biocompatible and corrosion resistant and is approved for biomedical use. These properties are desired in implant engineering.

In the aerospace industries, strength to weight ratio is crucial to the overall economy. The structure strength is equally crucial. Ti6Al4V is used for the manufacture of various components in the aerospace industry.

Ti6Al4V is an alloy of titanium composed of 90% titanium (Ti), 6% aluminum (Al) and 4% vanadium (V). In the chemical composition, on one hand, Al acts as the α-phase stabilizer. It increases the alloy strength without affecting the ductility. On the other hand, vanadium acts as the β-phase stabilizer. Figure 12 shows the phase diagram of titanium alloys.

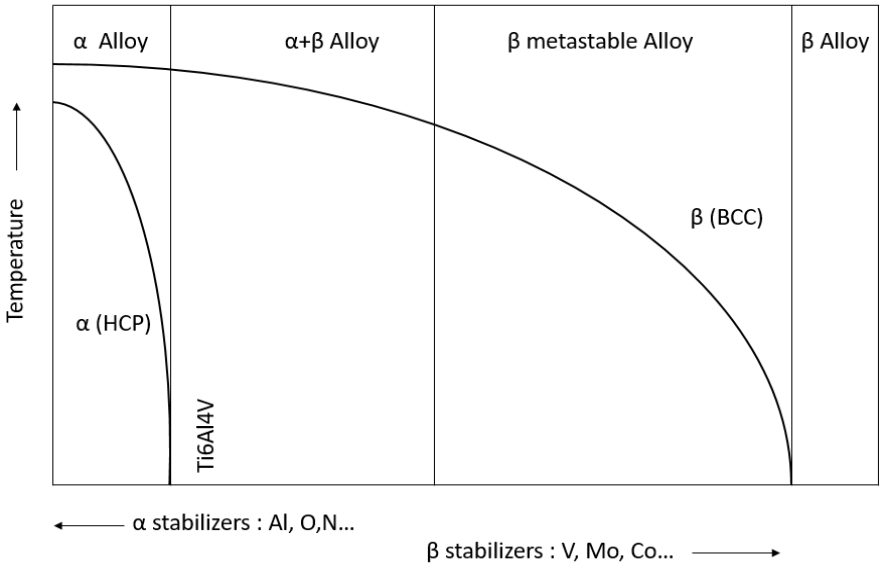

Figure 12: Adapted phase diagrams of titanium alloys [46]

Stellenbosch University https://scholar.sun.ac.za

2.5 Finite element method

FEM approximations have been used in solid and structural mechanics for the assessment and prediction of mechanical behaviors of solids and structures without having to manufacture the structure.

FEM approximations of mechanical, thermal and fluid behaviors of simple structures have proven successful. Simple structures have less modeling and discretization errors. However, it is not straight forward to approximate the behavior of complex structures such as lattice structures. These structures are prone to have both modeling and discretization errors. In addition to these errors is the numerical error, arising from the assumptions associated with numerical solutions. The modeling and approximation errors can be minimized through careful designing and extreme mesh refinement schemes. The latter requires high computational power.

Complex structures are now possible to build as a unit through AM techniques. As mentioned in section 2.1.3, these AM techniques have influences over the mechanical properties of structures by affecting their microstructure. There is a considerable difference in the CAD model used for FEM simulation and the L-PBF manufactured structure used for mechanical testing. There is a need to derive new material models or scaling laws for reliable approximations of the properties of lattice structures; materials models that accounts for the various changes the material and structure undergo during their production and scaling laws to scale the simulation result to better approximate the actual mechanical testing results.

As mentioned in section 2.2.2, lattice structures are built by repeating unit cells in all 3 dimensions. Therefore, the material behavior is assumed to be isotropic, that is, the material will have identical behavior in all three dimensions. This assumption has been proven admissible in many research studies [40-43]. Another consideration is to consider whether the mechanical properties can be accurately approximated through a linear or non-linear FEA analysis. Lattice structures consist of a network of many struts that undergo large deformation. The determination of mechanical properties and deformation from a linear static analysis, where only small deformations are considered and the stiffness is independent of the deformation, is not appropriate for the FEA simulation of lattice structures. Therefore, a non-linear static analysis is appropriate for the FEA approximation of mechanical properties and deformation of complex structures.

Another consideration is the type of nonlinearity to implement in the FEA simulations. There are three types of nonlinearities: material nonlinearity, geometric nonlinearity, and contact nonlinearity. Since many lattice structures are not designed with any contact conditions, only material and geometric nonlinearity are considered. Material nonlinearity refers to a material that experiences large strain as a result of material plasticity behavior. Geometric nonlinearity refers to the large deformation that a structure can experience during loading.

Stellenbosch University https://scholar.sun.ac.za

The simulation procedure for the nonlinear static analysis will consist of solving a system of nonlinear static equilibrium equations derived through a consideration of equilibrium equations, constitutive equations, and the compatibility equations as explained in [51].

$$[K(X)]\{X\} = \{F\} \tag{10}$$

With initial conditions $X_{(0)}^{t+\Delta t} = X^t$, $K_{(0)}^{t+\Delta t} = K^t$, $F_{(0)}^{t+\Delta t} = F^t$

where K is the structure stiffness coefficient matrix, X is the displacement vector and F is the load vector.

The solution to equation (10) is found through numerical iteration, using the Newton-Raphson method, to establish a relationship between the load and displacement as shown in Figure 13 The solution is obtained through a series of linear approximations with correction.

The Newton-Raphson method is the most used iteration method for many FEA codes. Figure 13 presents a graphical explanation of the implementation of the Newton-Raphson method, where the total load F_t is applied fully or incrementally. Considering the initial conditions, the intermediate load F_1 is calculated from the initial result X_1 and the stiffness, $K(x_1)$ is also obtained. The stiffness matrix is continuously updated until the residual $F_t - F_n$ is small enough, for n = 1,2,3 . . . n. The solution (curve) is obtained when the convergence criteria (force or displacement) is reached.

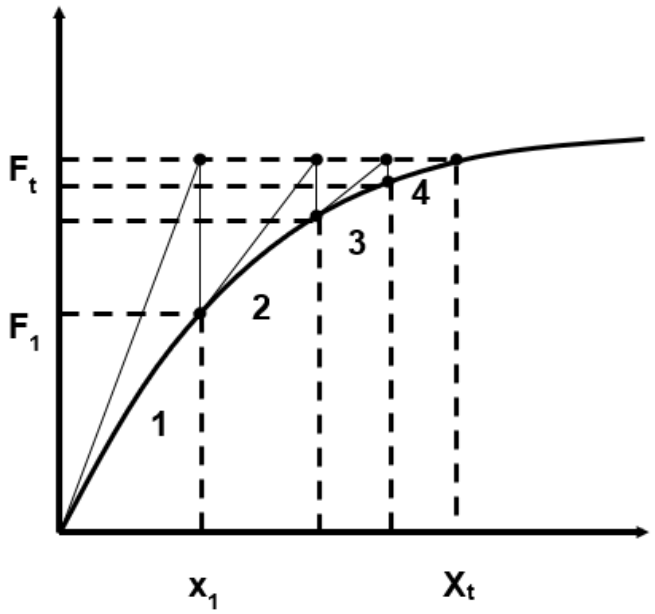

Figure 13: Newton-Raphson Method: load-displacement diagram

The computational size of the problem (Equation (10)) and therefore the accuracy of the solution will depend on the chosen discretization method and

Stellenbosch University https://scholar.sun.ac.za

its shape or interpolation function. Many research studies on the FEM simulation of mechanical properties of lattice structures have used tetrahedron and beam elements.

2.5.1 3D solid elements

Tetrahedron elements with ten nodes or tet10 are solid elements with quadratic interpolation functions. This allows the element to capture most of the deformation behavior of the structure as compared to tet4. These elements can be used to represent the mesh of the 3D solid structure to be manufactured without altering its density. For accurate or acceptable results, a fine mesh is required when using these elements. This leads to a high computational time for the solution to the problem defined by equation (10). In certain cases, 1D beam elements are used instead to reduce the computational time requirement.

2.5.2 1D beam elements

Beam elements are also used to represent the lattice struts during the simulation process. The deformation behavior that the beam element reports is based on beam theories implemented in FEA software. Euler-Bernoulli and Timoshenko beam theories are commonly used. The struts of the structure can be modeled as beams and beam results such as axial force, shear force and bending moments, about the strut can be reported. Because of the difficulty in the modeling of beam elements to fully represent the physical lattice structure, there is an increase in the structure's density due to the inability to merge the material at strut joints. This results in an increase of the mechanical properties as described by equations (1), (2), and (3).

2.5.3 Mesh sensitivity analysis

Equation (10) is a displacement-based problem. Here, displacements are solved at each node of each element of the discretized model continuously. From the computed displacements, nodal stresses are computed in each element discontinuously using Hooke's law. In order to obtain a continuous stress field across the model, the computed stresses in every element are averaged and this is the source of potential discretization error. Equation (11) illustrates the concept of discretization error from the stress calculation [52]

$$\left[\Delta\sigma_n^i\right] = \left[\sigma_n^a\right] - \left[\sigma_n^i\right] \qquad (11)$$

Where,

$\left[\sigma_n^i\right]$ is the stress vector at node n of element i;

$[\sigma_n^a]$ is the averaged stress vector at node n = $\frac{\sum_{i=1}^{N_e^n}\sigma_n^i}{N_e^n}$;

Stellenbosch University https://scholar.sun.ac.za

$\left[\Delta\sigma_n^i\right]$ is the stress error at node n of element i;

N_e^n is the number of elements connecting to node n.

It should be noted that as further mesh refinement is applied, there will be less and less difference between the stress vector and the averaged stress vector. $\left[\Delta\sigma_n^i\right]$ will approach zero and this will give a continuous stress field across the model. This results in the minimization of the discretization error.

It is not always easy to have a much smaller element size in order to obtain good approximations as this leads to extremely long processing time and requires high-performance computing which is not economical [52]. With intricate designs such as lattice structures, it is important to rely on the mesh convergence analysis to determine the right element size that leads to acceptable results. However, it is not easy to estimate correctly a smooth convergence since stress values can keep jumping between values. Pointer recommends to graphically establish the convergence and run the simulation multiple times [53]. In addition to this, the analysis quality check provided in the simulation code of NX Nastran is introduced here as an important tool to ensure the right element size. The quality analysis calculates the strain energy error norm and determines the confidence level of the result and recommend further mesh refinement if needed. This can provide a hint as to what element size, mesh convergence is achieved. According to the analysis quality check, most engineering applications require the strain energy error norm to be less than 5%.

2.6 Mechanical testing

ISO standard 13314 presents the standardized testing method for evaluating the ductility of a porous or cellular metal using compressive testing [12]. This standard is commonly used to determine the mechanical properties of metal lattice structures [53–56]. The properties represent the global behavior of the lattice structure, not the mechanical properties of the strut material.

Ashby et al. recommend determining the elastic modulus of porous structures from loading the structure to 75% of the compressive strength and unloading it - the elastic modulus can be determined from the unloading curve [34].

Figure 14 and Figure 15 show a typical stress-strain curve obtained using this standard, with the construction lines for the determination of the relevant mechanical properties. The plateau stress, σ_{pl}, is obtained by taking an arithmetic average of stresses measured between 20% and 40% strain. Young's modulus is calculated from the slope of the secant line of the unloading curve between 70% and 20% of the plateau stress value. The yield strength is calculated using the 0.2% offset strain method, as shown in Figure 15.

Stellenbosch University https://scholar.sun.ac.za

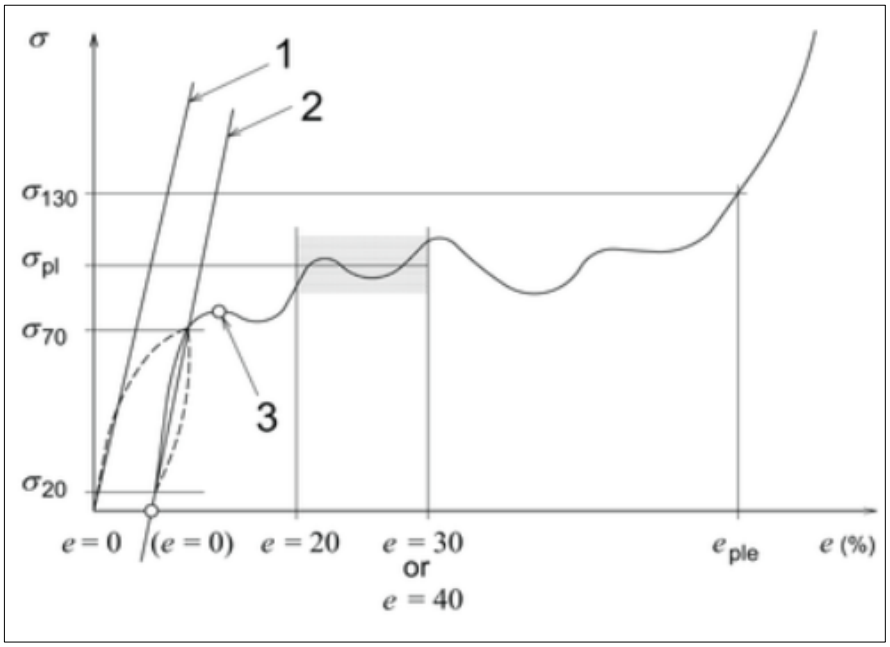

Figure 14: Stress-strain curve for porous or cellular metals, showing the determination of the mechanical properties according to ISO 13314:2011[12].

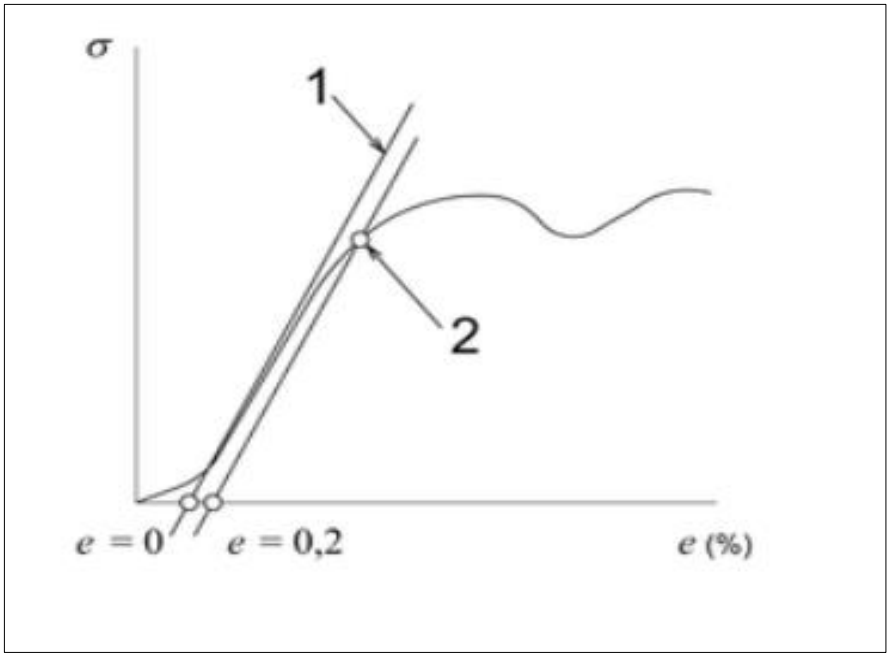

Figure 15: Portion of the stress-strain curve for porous or cellular metals, showing the determination of the 0.2% offset strain yield strength according to ISO 13314:2011 [12].

Stellenbosch University https://scholar.sun.ac.za

3 Methodology

This chapter will outline the methods and procedures that were followed to study the mechanical and deformation behavior of the selected lattice structures.

3.1 Design of lattice structure

The design process of lattice structures involves the consideration of specific parameters. These parameters are the selection of the building block, unit cell topology, and the desired relative density, which defines the material fraction for the lattice structure and its dimensions.

3.1.1 Selection of unit cell

The selection of the unit cell topology is fundamental to the application requirements of the lattice structure. A specific unit cell has a unique combination of deformation mechanism and mechanical properties. Open-cell, strut-based unit cells were chosen as the building blocks for the design of the lattice structures that were studied.

The unit cells were selected based on the Maxwell criteria, static stability, and determinacy, as given in section 2.2.5. Two structures were chosen, one defined as stretch-dominated and the other bending-dominated, as per the Maxwell criteria. These structures were chosen as benchmark studies in order to confirm whether experimental data support the Maxwell criterion and to determine which FEA formulation represents the actual primary deformation mechanisms most accurately.

5 X 5 X 5 lattice structures made from the tesselation of the unit cells, 125 unit cells in total, were considered.

3.1.2 Relative density

The relative density, $\bar{\rho}$, a key concept in the design of lattice structures, is the ratio of the density of the lattice structure, ρ_l, to the density of the solid material used to manufacture the lattice structure, ρ_s , as given in equation (12).

$$\bar{\rho} = \frac{\rho_l}{\rho_s} \tag{12}$$

The relative density also corresponds to the ratio of the lattice volume, v_l, to the total lattice structure volume, v_{tot}, $\bar{\rho} = \frac{v_l}{v_{tot}}$.

The determination of the relationship between the relative density and the lattice structure parameters involves the consideration of specific unit cells

Stellenbosch University https://scholar.sun.ac.za

for each topology, as well as the number of repeating unit cells in the entire lattice structure under review. This is critical as the location of unit cells in the structure, whether the cell is internal or on an outer surface, influences the relative density of the lattice structure. This is because the cells on the outer surface do not share boundaries with other cells on all of their sides. For this reason, we categorize different types of lattice unit cells according to their position in the lattice, namely

- Core;
- Side;
- Corner or vertex;
- Edge.

Figure 16 indicates the general position and terminology for each cell type in a 5 x 5 x 5 lattice of 125 unit cells. Each block represents a single unit cell, containing the repeating lattice structure within its volume

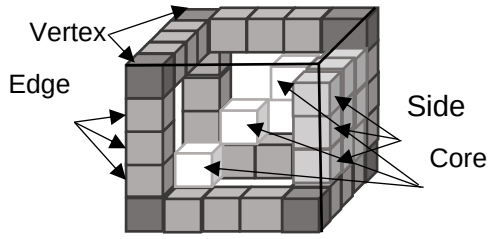

Figure 16: Schematic showing the different types of lattice unit cells, named for their positions in a 5 x 5 x 5 lattice.

The 5 X 5 X 5 lattice structure contains 3 X 3 X 3 core unit cells and 98 idiosyncratic edge, vertex, and side unit cells. The vertex, edge, and side unit cells contain full cross-section struts located at the outer sides.

The lattice volume, v_l, is calculated as the sum of the volume of each of the struts over all of the lattice cells. As the relative density corresponds to the ratio of the lattice volume to the total volume of the lattice structure (the 5 x 5 x 5 lattice total volume, including both strut and open space), it was used as a design parameter in order to determine the strut dimensions.

3.2 AM of lattice structures

The selected lattice structures in this study were manufactured using a Concept Laser M2 cusing machine at the laboratory for advanced manufacturing of Stellenbosch University. This machine uses the L-PBF AM technique to build parts layer by layer. It is a single laser machine with the capability to handle reactive materials such as titanium and can build finer

Stellenbosch University https://scholar.sun.ac.za

dimensions as compared to other L-PBF techniques. The machine's specifications are provided in Appendix D.

Parameters such as laser power, spot size, and scan speed can influence the dimensional accuracy and the mechanical properties of the final part. The optimal values of these parameters based on the manufacturer's recommendation will be selected for the manufacture of the selected structures of the present study. A fusion power of 110 W, scanning speed of 600 mm/s, and spot size of 0.15 mm were chosen to produce the selected designs.

The build process induces residual stresses in the final part due to thermal gradients as described in section 2.1.3 Post-processing heat treatments help in reducing the residual stresses and decompose the martensitic phase into an α-β phase. The heat treatment process chosen for this study followed the ASTM standard F2924-14 and SAE H81200D standard specification.

Five 5 x 5 x 5 lattice structures, of each lattice design were built on a Ti6Al4V wrought base plate. The manufactured structures were subjected to a stress relief heat treatment process, under flowing argon, while still on the titanium building plate to avoid warping. The heat treatment process used is summarized in Table 2.

Table 2: Stress relief heat treatment parameters

Material	Stress relief temperature	Soaking time
Ti6Al-4V	650 °C	180 min

After heat treatment, the structures were wire-cut from the build plate and subjected to CT scanning before conducting mechanical tests. The top and bottom platens were cut flat and parallel to allow for correct alignment of the uniaxial compressive load during testing.

3.3 Finite element analysis

Finite element analysis allows for the prediction of the mechanical and deformation behavior of the lattice structures. Simulations using both 3D solid elements and 1D beam elements, respectively, were chosen for this study in order to compare the suitability and efficiency of these approaches. ANSYS Workbench Mechanical was used for both approaches.

The simulation was set up to simulate the uniaxial compression experiment. The lattice structure was modeled as a 5 x 5 x 5 unit cell lattice, connected to two compression platens at the top and bottom surfaces. A displacement boundary condition was specified at the top platen in the negative z-direction while the z-axis translation of the bottom platen was fixed. Reaction forces on the bottom platen were used to calculate the global normal stress by dividing the reaction forces by the bottom platen area. The global normal strain was calculated by dividing the displacement in the z-direction by the original length between the two platens.

Stellenbosch University https://scholar.sun.ac.za

Since lattice structures are porous structures, their failure occurs due to both deviatoric and hydrostatic stress. Thus, both the deviatoric and hydrostatic stresses were recorded for these simulations.

Initial simulations used the CAD design lattice geometries as input. For final simulations, the geometry of the lattice was updated to take into account geometric deviations that were measured using CT scanning of the as-built structures.

3.3.1 3D solid element simulation

Solid elements such as tetrahedron elements with 10 nodes and hexahedron with 20 nodes provide full stress and strain results for structures. Due to restrictions on computational time, the tetrahedron elements with 10 nodes are usually preferred over the hexahedron elements. ANSYS solid elements, type Solid187 tetrahedron elements with 10 nodes (tet10), were selected for the solid element simulation of the lattice structures in this study.

As noted in section 2.5.3, it is important to use an appropriate mesh size in order to reduce the discretization error to a reasonable level. This is essential for producing valid and accurate FEA simulations. It is common practice to conduct a mesh sensitivity analysis to obtain the appropriate mesh size. In the present study, graphical mesh analysis, aspect ratio analysis, and strain energy error norm were used to evaluate the appropriateness of the mesh size.

Graphical mesh analysis consists of a comparison of the force-displacement or stress-strain results for different mesh sizes. The convergence of these results will occur when different mesh sizes give the same results.

For a tetrahedron element, the aspect ratio is the ratio of the longest dimension to the shortest dimension of the element's edges. When this value is 1 or close to 1, the mesh size is acceptable; a poor mesh size will have an aspect ratio of 0 or close to 0.

Running a linear-static analysis in NX Nastran will give the stress-strain result from which the strain energy error norm is automatically calculated. Many engineering applications recommend a strain energy error norm of less than 5%.

These parameters were used in order to conduct the mesh sensitivity analysis for the simulations in this study.

3.3.2 1D beam element simulation

Beam elements are commonly used in the FEM simulations of lattice structures as a substitute for solid elements. This is in response to the high computation power required for solid elements as a result of a highly refined mesh that is required for accurate results. Beam elements can provide

Stellenbosch University https://scholar.sun.ac.za

accurate approximations without the need for mesh refinement, using far fewer elements than a solid element analysis, but can only be used if appropriate for the physical scenario that they are simulating.

The formulation of these elements is usually carried out by considering beam theories. Euler-Bernoulli and Timoshenko beam theories are commonly implemented in different FEM software for the formulation of beam elements.

In the present study, ANSYS Timoshenko beam elements (beam188) were used for the beam element simulation. This allowed the shear deformation of the struts in the structure to be captured. This is not possible when the Euler-Bernoulli beam elements are used.

The beams were modeled in ANSYS SpaceClaim, using line bodies with the strut cross-section assigned to the line bodies. The top and bottom platen were modeled as 3D solid plates. The plates were meshed using hexahedron elements.

The same boundary conditions as in the solid element simulation were applied to the top and bottom platens, with the global stress and strain calculated similarly.

3.4 Mechanical testing: compression

Compression tests of lattice structures were conducted by following the ISO standard test method for compressive properties of porous metals, as presented in section 2.6. The compressive stress is calculated from the applied force divided by the original area of the top compression platen and the compressive strain is calculated from the crosshead displacement divided by the original length between the platens. The stress-strain diagram is obtained from these values and other compressive behaviors, such as the compressive yield stress, the compressive proof stress, and the maximum compressive stress are calculated according to the standard.

A total of 10 specimens were produced for each lattice structure, 5 of circular cross-section and 5 of square cross-section. 2 of the 5 specimens per lattice structure design were tested up to the first point of yielding, and the remaining specimens were fully compressed.

3.5 Computed tomography (CT) scan of manufactured lattice structures

The manufactured structures were CT scanned for geometrical analysis using the Phoenix nanotom S, a Nano-CT system available at the CT facility of Stellenbosch University [42]. The scan process was conducted following the guidelines and procedures set out in [4-7].

Lattice structures were scanned before the mechanical testing to determine the as-built geometrical parameters. This was important because the

Stellenbosch University https://scholar.sun.ac.za

mechanical properties have a proportional relationship with the relative dimensions of the porous structure. Therefore, any variation in the relative dimension will cause a variation in the mechanical properties of the porous structure. Features such as surface roughness and strut waviness were studied and compared to the CAD geometry used as input for the L-PBF manufacturing process.

The two specimens tested up to the first yield were scanned in order to determine the regions of crack initiation and the deformation mechanisms of the structures.

A line of connected struts from the other 3 specimens that were tested to 50% strain was cut off in order to CT scan the collapsed structures and determine the failure initiation regions.

Stellenbosch University https://scholar.sun.ac.za

4 FEM and experimental results

This chapter outlines the results of the project, following the methodology presented in Chapter 3. Results are presented for the design of the selected lattice structures, the manufacturing process, computed tomographic analysis, FEA compression simulation, and for the mechanical testing.

4.1 Design of lattice structures

This section reports on all aspects regarding the selection and CAD design of the lattice structures.

4.1.1 Selection of unit cells

Two common lattice design unit cells were chosen for this study: the octet-truss and diamond topologies, which are stretch-dominated and bending dominated, respectively. Figure 17 shows the synthesis of the octet-truss and diamond lattice structures' unit cells, respectively.

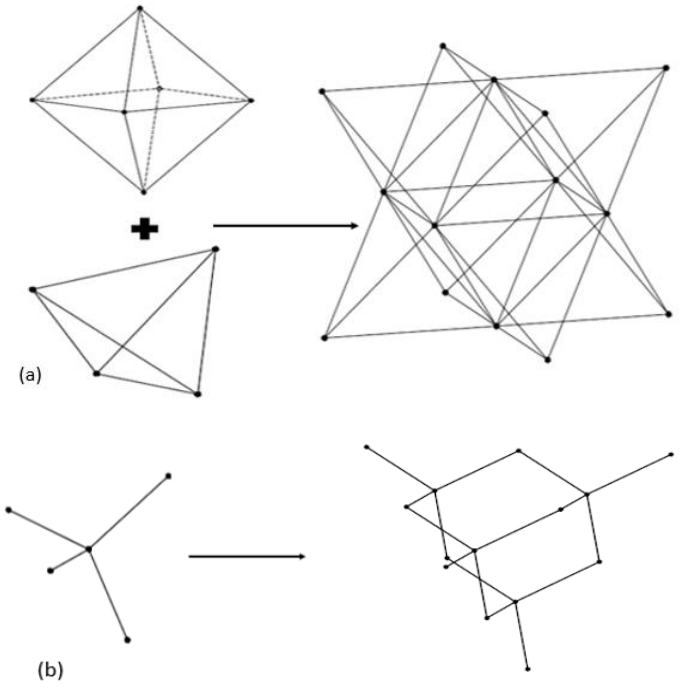

Figure 17: Synthesis of the octet truss (a) and diamond (b) structures

Figure 17(a) shows the octet-truss unit cell. It is constructed from the combination of the octahedron unit cell and the tetrahedron unit cell at each of the 8 faces of the octahedron unit cell. The octahedron and tetrahedron unit cells both satisfy the stretch-dominated condition, thus making their combination, the octet-truss structure, stretch-dominated. The octahedron

Stellenbosch University https://scholar.sun.ac.za

with 12 struts and 6 joints and the tetrahedron with 6 struts and 4 joints, both have a Maxwell criterion M value of 0, as calculated using Equation (9).

The diamond unit cell is constructed from 4 diamond unit structure as shown in Figure 17(b). The diamond unit cell satisfies the bending-dominated condition, thus making the whole diamond structure bending-dominated. The diamond unit cell has 4 struts and 5 joints, resulting in a negative Maxwell criterion M value, as calculated by Equation (9).

4.1.2 Relative density

Selected octet-truss and diamond lattice structures of fixed porosity and strut thickness were designed using an iterative process of calculating the strut volume as a function of thickness until the desired structure was obtained, design equations were derived based on this process.

As defined in section 3.1.2, the relative density of a lattice structure, $\bar{\rho}$, is the ratio of the volume of the lattice structure, v_l, to the total structure volume, v_{tot}. For a 5 x 5 x 5 lattice structure, a fixed unit cell length of $l = 2\ mm$, the total structure volume $v_{tot} = (5l)^3$. As mentioned in section 3.1.2 determination of the lattice volume will require the consideration of the location of the unit cell in the lattice structure. The nomenclature used to define the unit cells based on the location was as follows: the core, the side, the vertex, and edge unit cells.

Core unit cells

Core unit cells are every unit cells located inside the lattice structure, that are not exposed to an outer surface or edge, as defined in Figure 18. They are the true repeating units of the lattice structure and are mirrored in all three dimensions, on all six sides. They share their diagonal struts with the six adjacent unit cells.

Stellenbosch University https://scholar.sun.ac.za

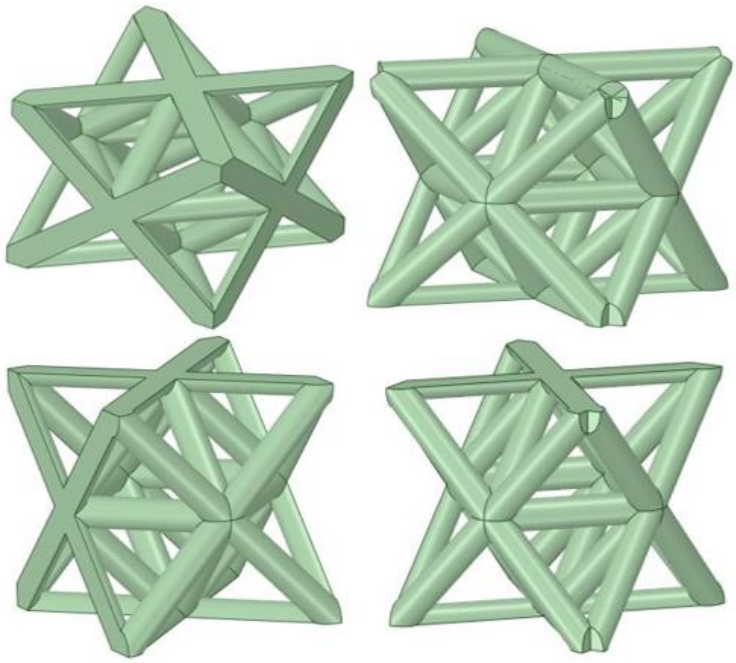

Figure 18: Core unit cell (top left), vertex unit cell (top right), side unit cell (bottom left), edge unit cell (bottom right)

Vertex unit cells

The corner or vertex unit cells are the unit cells located at the 8 vertices of the lattice structure. They share material with three adjacent unit cells as seen in Figure 18.

Side unit cells

Side unit cells are every cell located on outer surfaces of the lattice structure, excluding the cells at the edges. They share material with the five adjacent unit cells. This is seen in Figure 18.

Edge unit cells

The edge unit cells are the unit cells located along the 12 edges of the lattice structure. They share material with the four adjacent unit cells. This is seen in Figure 18.

The relative density of the lattice structure is then obtained by considering the volume of each strut in each group of unit cells and considering how the strut material is shared. Using Equation (13), the relative density can be obtained.

$$\overline{\boldsymbol{\rho}} = \frac{\boldsymbol{v_l}}{\boldsymbol{v_{tot}}} \tag{13}$$

Stellenbosch University https://scholar.sun.ac.za

5 X 5 X 5 diamond and octet-truss structures contain 3 X 3 X 3 core unit cells and idiosyncratic 36 edge, 8 vertex, and 54 side unit cells. Thus, the total lattice strut volume, v_l, is

$$v_l = 27\, v_c + 54\, v_s + 8\, v_v + 36\, v_e \tag{14}$$

The vertex, edge, and side unit cells contain full cross-section struts located at the outer sides. The relative densities for the octet-truss and diamond lattice structures were obtained as below,

$$\bar{\rho}_{octet} = \frac{1650.03}{125}\sqrt{2}\frac{A}{l^2} \tag{15}$$

$$\bar{\rho}_{diamond} = \frac{(375+348\sqrt{2})}{125}\frac{A}{l^2} \tag{16}$$

Equation (15) and Equation (16) were used to calculate the design strut thickness for a fixed relative density. These equations are suitable for 1D beam element design where at the strut joint, the material was not merged. However, for the solid element design, this material was merged and Equation (15) and (16) over-estimated the 3D solid lattice volume by about 20 %. Figure 19 shows the joints of an octet-truss unit cell where the joint material was merged between struts of the entire lattice structure.

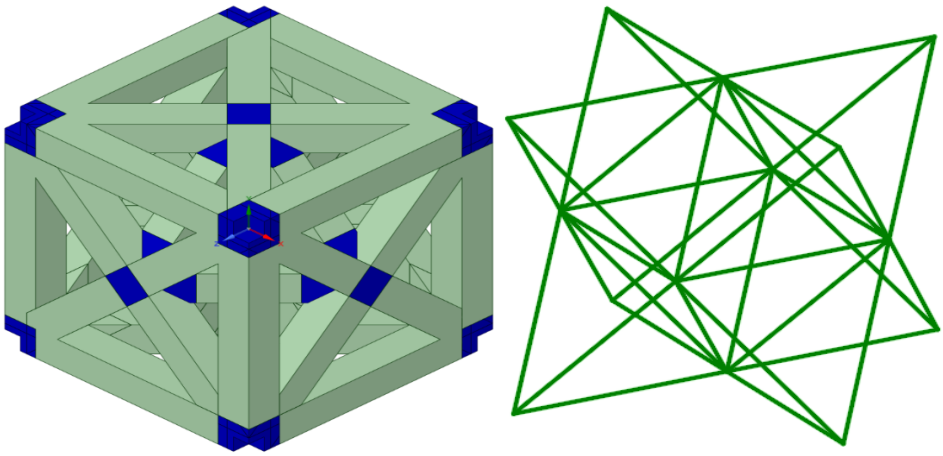

Figure 19: Rectangular octet-truss unit cell design showing the shared joint material, solid design (left), beam design (right)

All lattice structures, solid and beam structures were designed using SpaceClaim designing software available in the ANSYS software package. Both solid and beam lattice structures were modeled through the pattern of a unit cell in 3 dimensions to obtain a 5 X 5 X 5 lattice structure. The solid unit cell was modeled as a network of 3D solid struts which were merged for both topologies whereas the beam unit cell was modeled as a network of 1D line bodies to which a cross-section was assigned. Figure 19 shows both solid and beam unit cells that were used to model the solid and beam lattice

Stellenbosch University https://scholar.sun.ac.za

structures. Table 3 shows the geometric parameters for the beam and solid lattice structure design used for the designs.

Table 3: Geometric parameters of the beam and solid lattice structures (C: circular cross-section, R: rectangular cross-section)

	1D Beam structure			3D Solid structure		
	Strut thickness [µm]	Lattice volume [mm^3]	Relative density [%]	Strut thickness [µm]	Lattice volume [mm^3]	Relative density [%]
Diamond-C	423	243.0	24.30	423	201.2	20.12
Diamond-R	375	243.6	24.35	375	201.8	20.18
Octet Truss-C	268	263.3	26.33	268	215.0	21.50
Octet Truss-R	237	262.1	26.21	237	212.1	21.21

It is important to note that the 3D solid designs were the physical models used as input to the manufacturing process software. It is possible to export solid structures into stereolithography (STL) files that are readable to the manufacturing software package. It is not possible to convert the 1D line bodies used to model the beam structures in the STL files. Therefore, the 3D solid structure was more representative of the manufactured structure in terms of the relative density and the nature of strut joint material. The strut joint material was merged in the 3D solid design and fused during the production process. Figure 20 shows the designed 3D solid and 1D beam structures, for both lattice designs, respectively. For the 3D solid structure, the final lattice was merged using Boolean operation. For the 1D beam structure, the unit cell was built as a line body. The beams in the entire structure were merged using a share topology option in the design software package (SpaceClaim). This ensured a bonded connection between the beams. Detailed steps of the CAD modeling of lattice structures are provided in Appendix E.

Stellenbosch University https://scholar.sun.ac.za

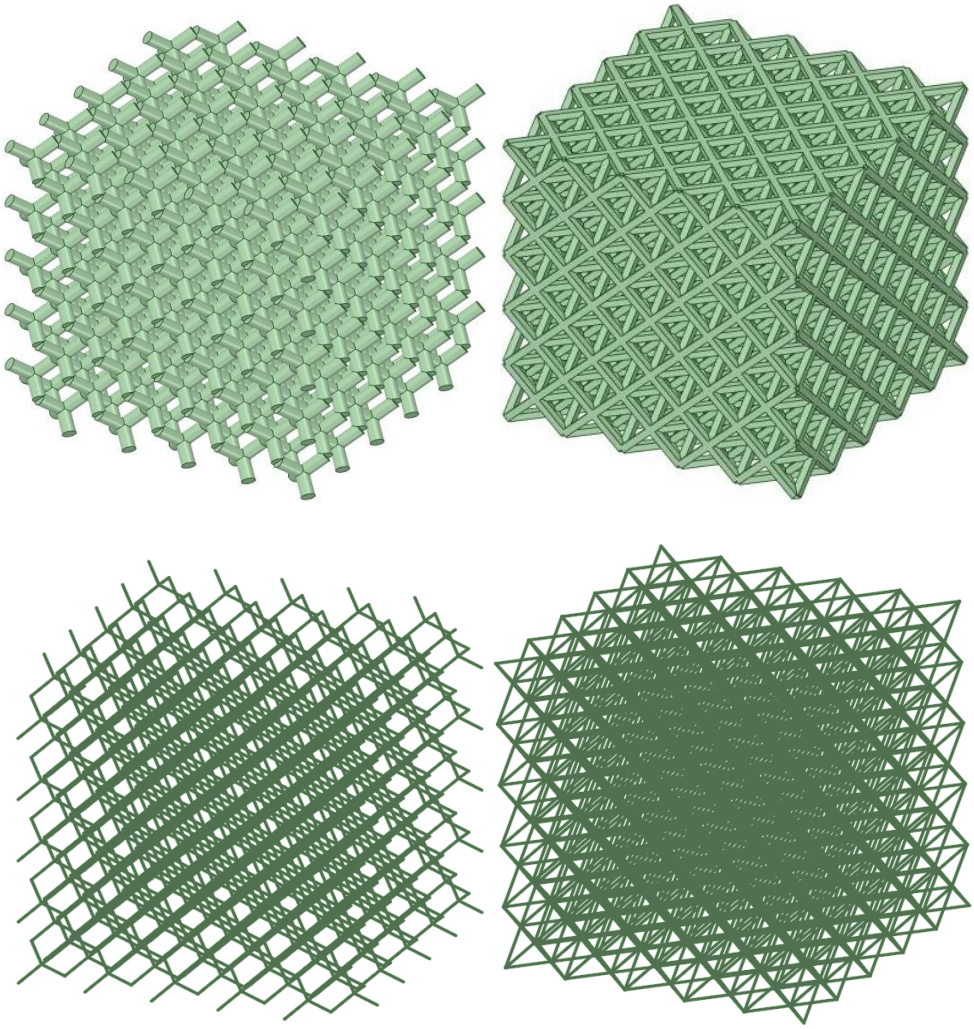

Figure 20: Designed lattice structures: solid circular diamond (top left), solid rectangular octet-truss (top right), beam circular diamond (bottom left), beam rectangular octet-truss (bottom right)

4.2 Finite element analysis (FEA)

In order to conduct FEA compression simulations on the lattice structures, the full lattice structure was bound at its upper and lower surfaces by rigid platens (10.2 x 10.2 x 0.2 mm) with an area of 108.16 mm^2. The platens were modeled as 3D solid plates which were merged to the 3D solid lattice structure; whereas, in the case of the 1D beam lattice structure, the 3D solid platens were bonded, through a bonded connection, one to the topmost edges and the other to the bottommost edges of the structure. The distance between the top and bottom plates was 10 mm. These plates allow for uniaxial compression as prescribed in the ISO (13314) standard.

The tangent modulus for Ti6Al4V at room temperature was obtained from the ANSYS material library. Table 4 shows the yield strength and tangent modulus of Ti6Al4V at different temperatures. The yield strength used in this

Stellenbosch University https://scholar.sun.ac.za

study was obtained from a study that reported the tensile behavior of an SLM-produced Ti6Al4V that was stress relieved (SR) [58]. Figure 21 shows the tensile stress-strain diagram obtained in this study. Yield strength of 1145±17 MPa was obtained in the study for the SR Ti6Al4V. However, it should be noted that this value is approximate as the properties of as-built and stress relieved material varies depending on the specific production process parameters.

Table 4: ANSYS Ti6Al4V material properties

Temperature (C)	Yield Strength (MPa)	Tangent Modulus (MPa)
20	1098	1332
204	844	1207
427	663	1033
538	527	943
815	60	708
944	21	596

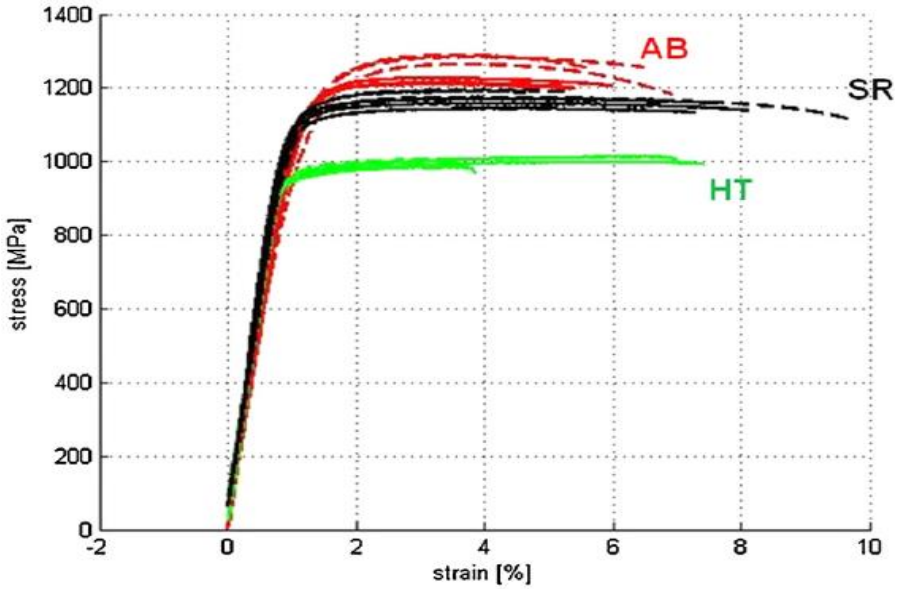

Figure 21: Tensile stress-strain diagram of SLM-Ti6Al4V for the as-built (AB), stress relief (SR) and the annealed (HT) conditions [58]

Young's modulus and Poisson's ratio of 110 GPa and 0.3, respectively, were selected for the Ti6Al4V material as indicated in Table 5.

The material properties defined in Table 5 were used for the nonlinear static analysis. An isotropic hardening model was used to define the plastic behavior of the material.

Stellenbosch University https://scholar.sun.ac.za

Table 5: Material properties of SR Ti6Al4V as input for the FEM simulation

Properties	Density [Kg m^{-3}]	Yield Strength [MPa]	Poisson's ratio	Modulus of Elasticity [GPa]	Tangent modulus [MPa]
Value range	4430	1145	0.3	110	1332

An FEA compression simulation was conducted following the test method set in ISO (13314) standard for mechanical compression testing of porous metals. ANSYS academic research Mechanical and CFD (structural/LS-Dyna) was used to conduct the FEA compression simulation. Detailed procedures of the use of ANSYS Mechanical to conduct compression FEA simulations are provided in Appendix F.

To simulate the compression of the lattice structures, a displacement of 1mm was applied on the top platen in the negative z-direction while the bottom platen was constrained to zero translation in the z-direction and free to translate in both the x and y-directions. This can be seen in Figure 22 below.

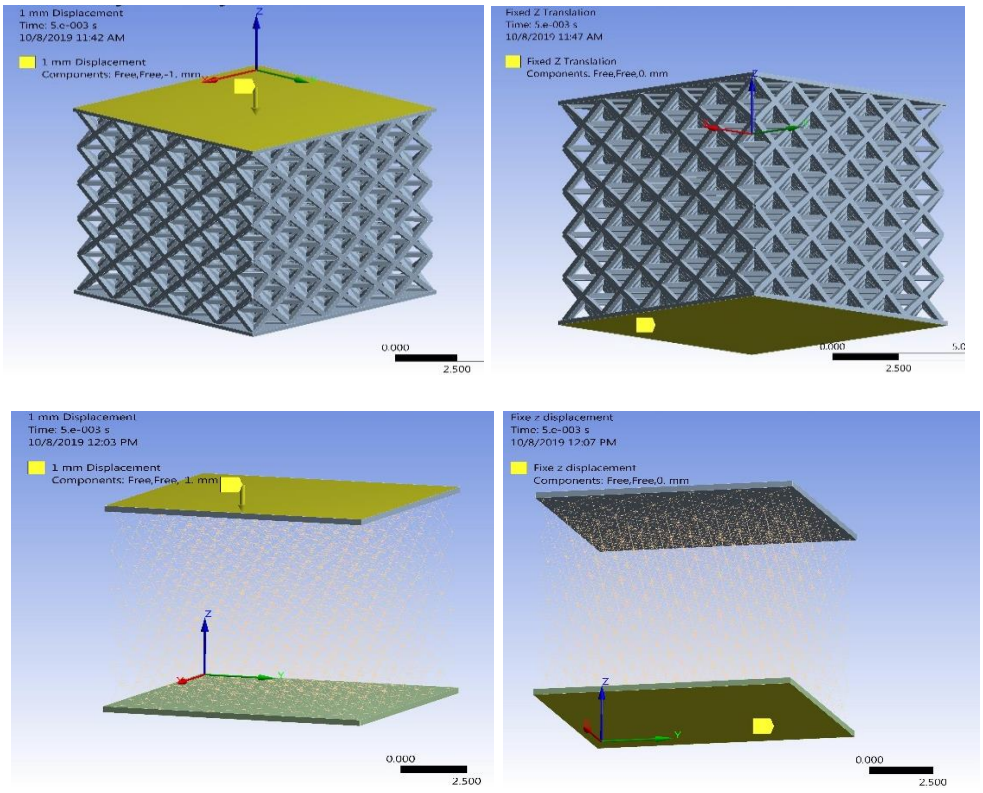

Figure 22: Boundary conditions for the FEA compression simulations: 3D solid structure (top), 1D beam structure (bottom)

To ensure that the results obtained for the 3D solid elements were accurate and within the allowable range of the strain energy error norm, a mesh

Stellenbosch University https://scholar.sun.ac.za

sensitivity analysis was conducted. It is important to note that this is not required when using 1D beam elements. 1D beam elements are usually used as a substitute for the 3D solid elements for their benefit in reducing the computational time.

4.2.1 Mesh sensitivity analysis

Section 2.5.3 outlined the importance of mesh refinement for the 3D solid element, in the improvement of FEA results. A graphical mesh sensitivity analysis was conducted for both topologies. Mesh sizes of 75 µm, 100 µm, 150 µm, and 100 µm, 150 µm, 200 µm were used to discretize the CAD models for the diamond and octet-truss lattice structures, respectively. Figure 23 and Figure 24 show the 3D models meshed with the chosen mesh sizes.

For the diamond lattice structure, the stress magnitudes for the 75 µm and 100 µm mesh sizes show a similar trend. However, the stress magnitude for the 150 µm mesh size was higher by 3 to 4 MPa than the other two mesh sizes.

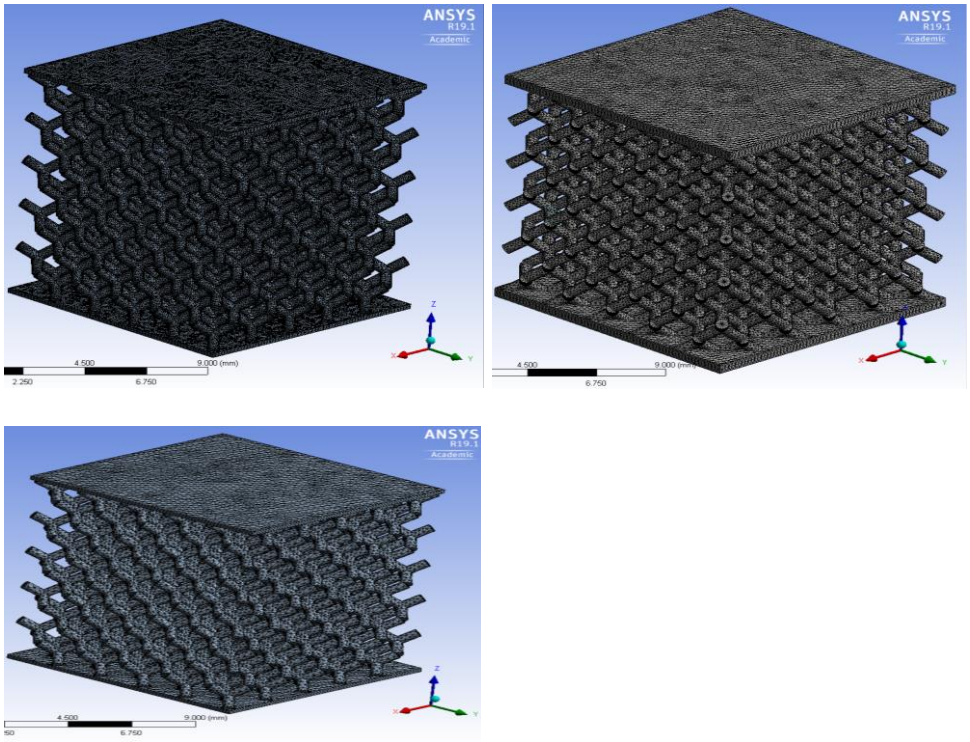

Figure 23: Diamond lattice graphical mesh sensitivity analysis with mesh sizes: 75 µm (top left), 100 µm (top right), 150 µm (bottom left)

Stellenbosch University https://scholar.sun.ac.za

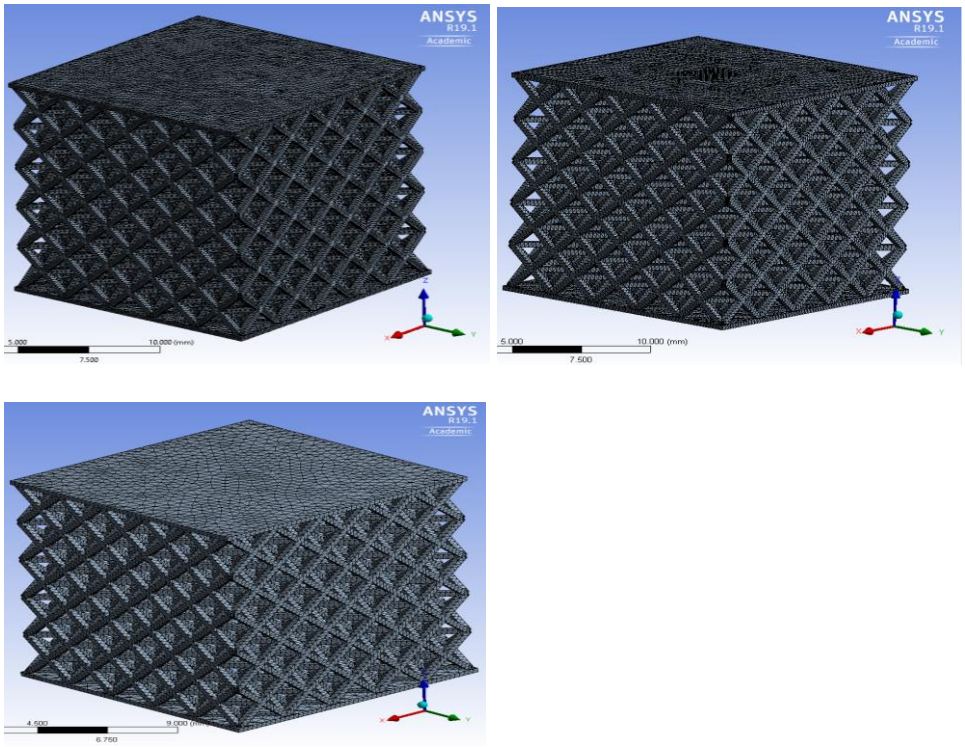

Figure 24: Octet-truss lattice graphical mesh sensitivity analysis with mesh sizes: 100 µm (top left), 150 µm (top right), 200 µm (bottom left)

For the octet-truss lattice structure, all three mesh sizes converged to the same magnitudes of the normal stress. This can be seen in Figure 25 and the stress error for the bigger element mesh size was also closer to zero. As reported in section 2.5.3, the stress error at node n of element i, $[\Delta\sigma_n^i]$, is the difference between the stress vector at node n of element I, $[\sigma_n^i]$, and the average stress vector at node n, $[\sigma_n^a]$. The accuracy of stress results is achieved when $[\Delta\sigma_n^i]$ approaches zero.

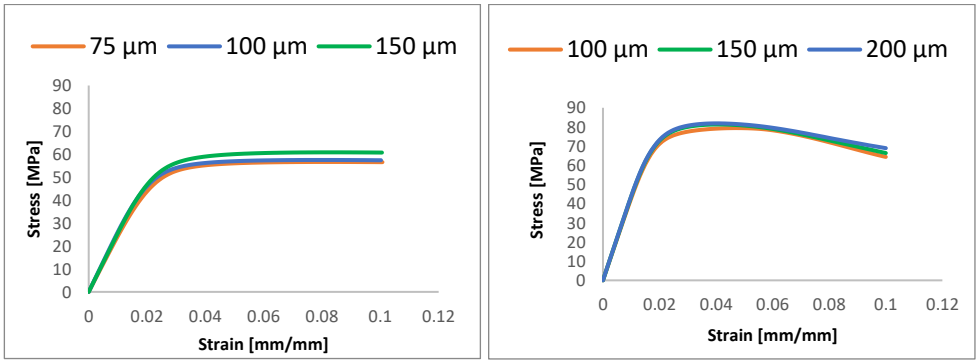

Figure 25: Stress-strain diagram for mesh sensitivity analysis: diamond structure (left), octet-truss (right).

Stellenbosch University https://scholar.sun.ac.za

Figure 26 shows that the stress error for both topologies is sufficiently closer to zero. Mesh size of 150 µm is chosen in the following study both to reduce the computational time and increase results accuracy.

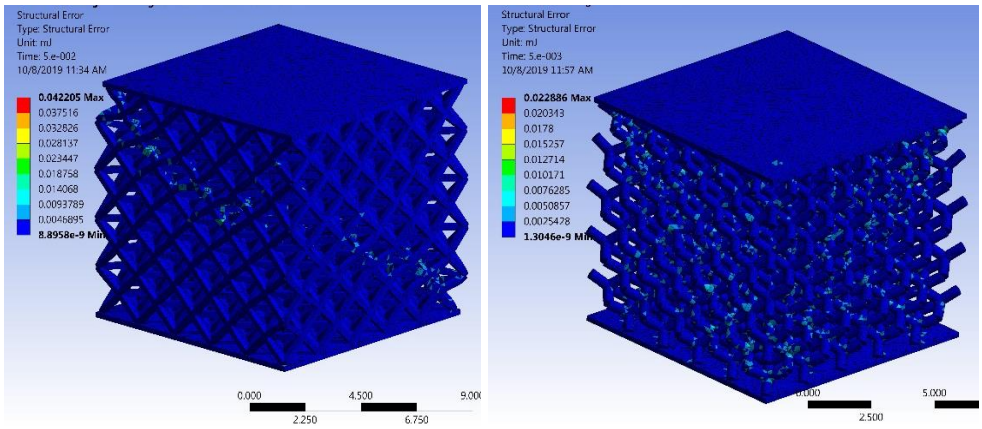

Figure 26: Stress error for 200 µm octet-truss mesh size and 150 µm diamond structures

The FEM results provide the stress distribution across the individual struts in response to the compressive load. This behavior of the individual struts contributes to the global response of the entire lattice structure. The global response of the entire structure is obtained by calculating the mechanical properties as described in ISO (13314) standard. The nature of the stresses against which the strut is resisting can be determined by carefully studying these stress distributions. These stress distributions in the individual struts can also give an indication of the failure initiation region and deformation mechanisms.

4.2.2 3D solid elements (Solid187) results

This section outlines the global stress and strain results of both the octet-truss and diamond lattice structures, with the global stress and strain calculated according to section 3.3.

Octet-truss lattice structure

The FEM results show the octet-truss lattice structure experiencing high normal stress across its struts. This is seen in the maximum principal stress result in Figure 27. A close observation of the maximum principal stress distribution shows that the horizontal struts in the octahedron section of the structure experience high tensile stresses whereas the struts in the tetrahedron section of the structure experience high compressive stresses.

Horizontal struts of the octahedral section, in the vertex unit cell, experience the highest tensile stress. Failure is expected to occur in this region (indicated by arrows).

Stellenbosch University https://scholar.sun.ac.za

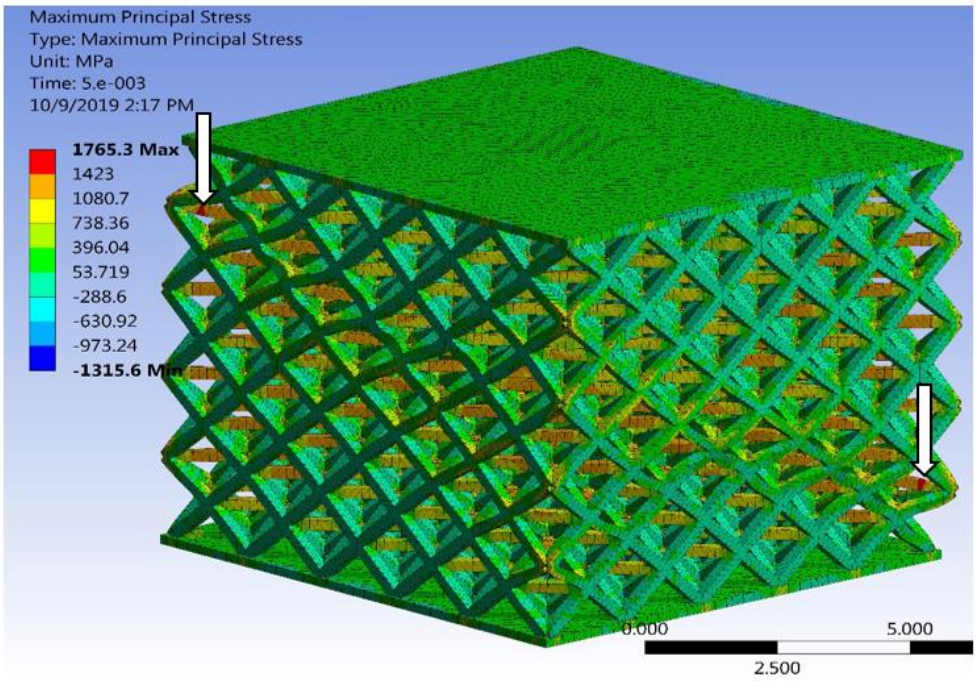

Figure 27: Maximum principal stress: 3D solid octet-truss lattice structure

The equivalent plastic strain results show the region of the high probability of failure. As seen in Figure 28, these regions of high failure probability are the horizontal struts in the octahedral section of the structure in unit cells located along the diagonal planes of the structure. This is shown in Figure 28 by the arrows. The struts in the octahedral section seem to be experiencing high plastic strain. The struts along these diagonal planes can be seen to be experiencing some bending.

Stellenbosch University https://scholar.sun.ac.za

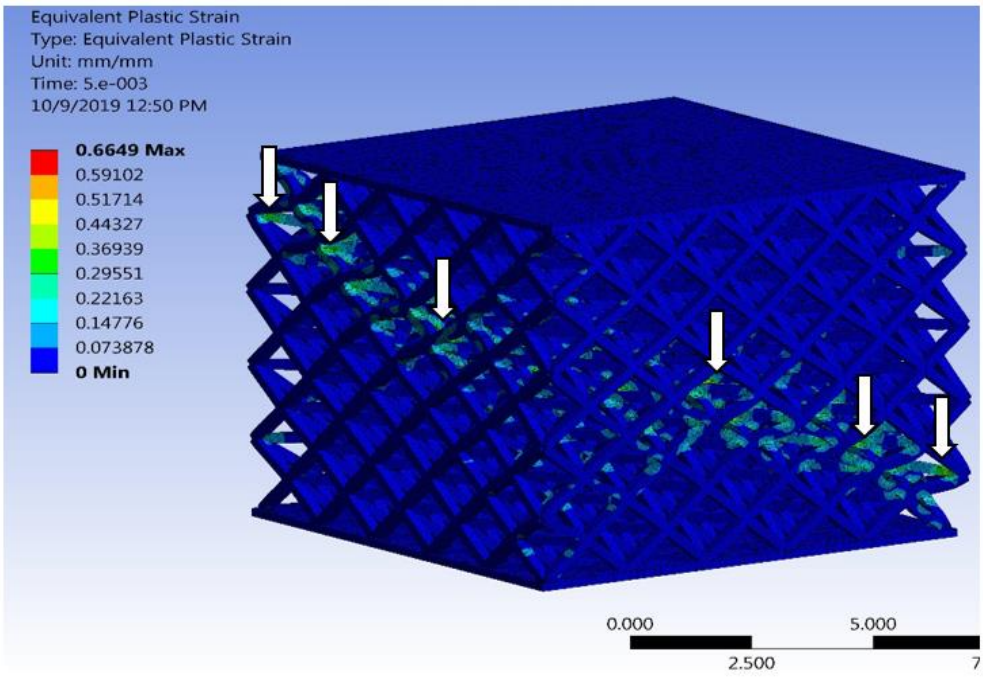

Figure 28: Octet-truss lattice structure: equivalent plastic strain

Figure 29 shows the global stress-strain behavior of the octet-truss lattice structure in response to a compressive load (see Figure 22) as predicted by the finite element analysis. The global stress-strain diagram was plotted for both a circular and rectangular strut cross-section. The naming convention is as follows: the first letter denotes the cross-section and the number denotes element size used to mesh the CAD model for the FEM simulation purpose.

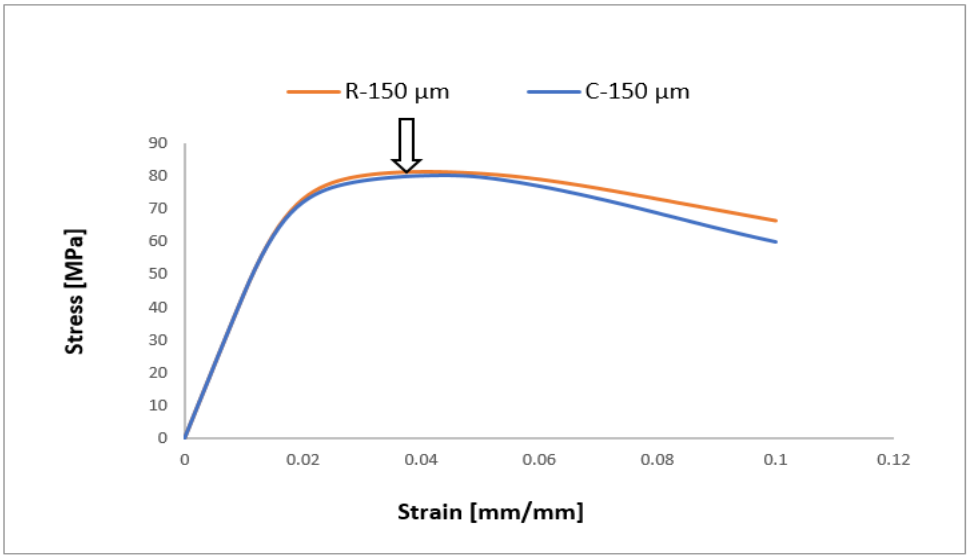

Figure 29: Direct stress-strain diagram of the octet-truss lattice structure of the rectangular and circular cross-section

Stellenbosch University https://scholar.sun.ac.za

The mechanical properties of the octet-truss lattice structure were determined as described in section 2.6 and as presented in Table 6.

From Figure 29, it can be seen that the octet-truss lattice structure reaches its maximum stress at a lower strain. A comparison between the two cross-sections is established. The slope of the curve after reaching the maximum stress decreases rapidly. This is an indication of lower strain energy and brittle failure of struts.

Table 6: Mechanical properties of the octet-truss lattice structure

Topology	Cross-section	Young's modulus [GPa]	Yield strength [MPa]	Maximum stress [MPa]	Strain at maximum stress
Octet-truss	Rectangular	3.98	72.85	81.28	0.041
	Circular	4.22	72.11	80.38	0.044

Diamond lattice structure

Figure 30 shows the maximum principal stress distribution across the struts of the diamond lattice structure. This distribution can be seen to be even across all struts. The region of high-stress concentration can be seen to be the strut joints of any of the unit cells in the entire structure. This is indicated by the arrows in Figure 30. A close look at an individual strut cross-section shows high tensile stress at the bottommost side of the strut while the topmost is subjected to high compressive stress. This is seen in the opposite order in other struts across the structure based on their location. This arrangement of high tensile and compressive stress at the topmost and bottommost side of the neutral axis of the strut cross-section is an indication of dominant bending behavior.

Stellenbosch University https://scholar.sun.ac.za

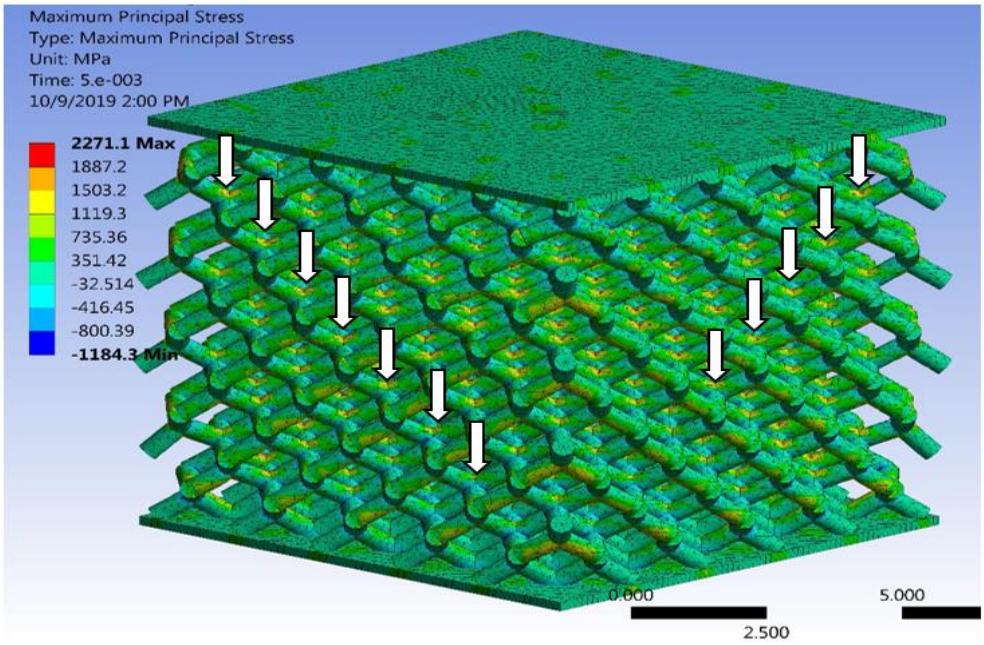

Figure 30: Maximum principal stresses: 3D solid diamond lattice structure

Figure 31 shows the equivalent plastic strain induced in the struts of the structure. It can be seen that the regions of high plastic strain are the strut joints in all the unit cells of the structure. The arrangement of the unit cells in the entire structure is such that the strut joints are located at 45° diagonal planes. This is shown in Figure 31 as indicated by the arrows, pointing to a diagonal plane where high plastic strain is induced.

The global behavior of the diamond lattice structure was obtained using the same equations as for the octet-truss lattice structures.

The mechanical properties describing this global behavior are tabulated in Table 7. In contrast to the octet-truss lattice structure, the diamond structure reaches its maximum stress at a higher strain. This behavior is typical of a structure with struts that bend before fracture, thus supporting the results obtained from the principle stress analysis earlier.

Stellenbosch University https://scholar.sun.ac.za

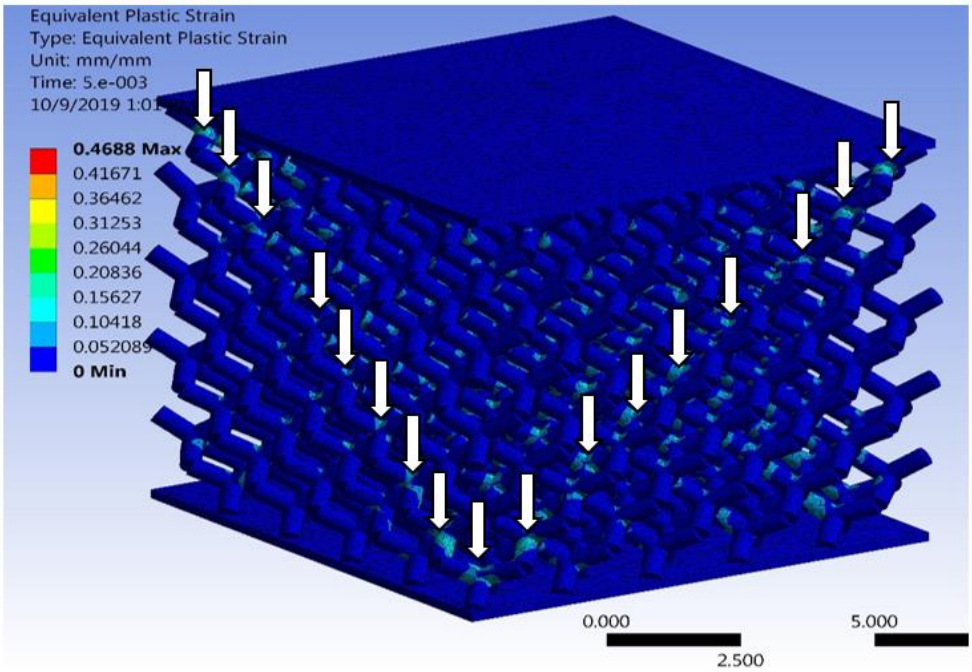

Figure 31: Diamond lattice structure: equivalent plastic strain

Figure 32 shows the global stress-strain response of the diamond lattice structure. Comparing this diagram to Figure 29 for the octet-truss lattice structure, it can be seen that the diamond lattice absorbs more strain energy before reaching the maximum stress. It reaches about 8% strain at the maximum stress, almost double that of the octet-truss at its maximum stress.

It can also be seen that the circular cross-section was stronger than the rectangular cross-section. However, both cross-sections show a similar stiffness.

It is important to note that the area under the stress-strain graph (see Figure 32) increases with a further displacement of the top platen.

Stellenbosch University https://scholar.sun.ac.za

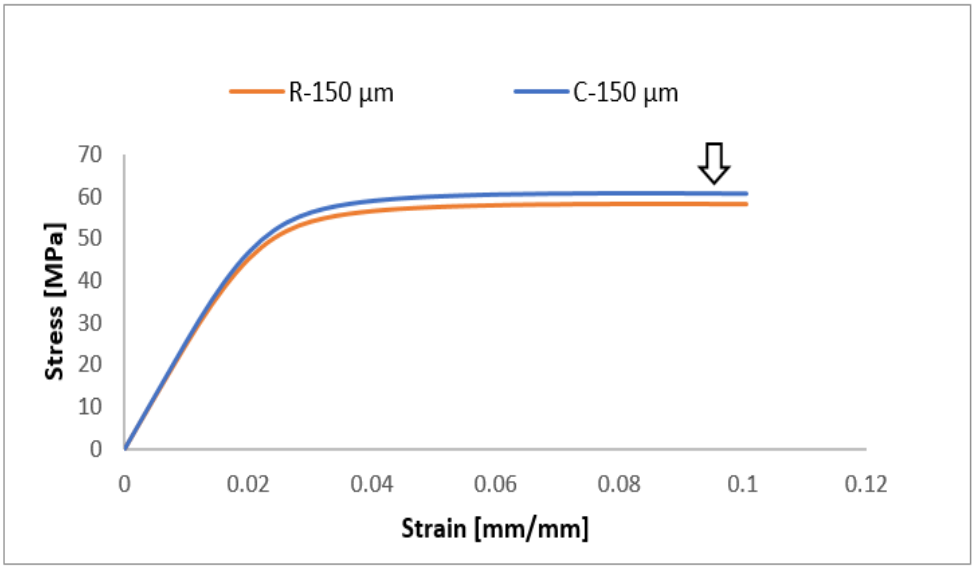

Figure 32: Direct stress-strain diagram of the diamond lattice structure of the rectangular and circular cross-section

The results reported here are associated with an applied displacement of 1 mm on the top platen. This can be seen in Figure 32 where the highest strain reached is 0.1, which is the induced deformation divided by 10.

Table 7: Mechanical properties of the diamond lattice structure

Topology	Cross-section	Young's modulus [GPa]	Yield strength [MPa]	Maximum stress [MPa]	Strain at maximum stress
Diamond	Rectangular	2.34	47.89	58.14	0.087
	Circular	2.36	52.05	60.85	0.083

4.2.3 1D beam element (Beam188) results

This section outlines the FEM results of both the 1D beam octet-truss and diamond lattice structures.

Octet-truss lattice structure

Figure 33 shows the maximum principal stress distribution across all struts in the octet-truss lattice structure modeled as a 1D beam structure. These results give an indication of the stress-induced in the struts when subjected to a compressive load in the negative z-direction. The results show on one hand, that the struts, in the 27 core unit cells, experience high tensile stress for the horizontal struts of the octahedral section whereas the inclined struts of the tetrahedron section are subjected to compressive stress.

Stellenbosch University https://scholar.sun.ac.za

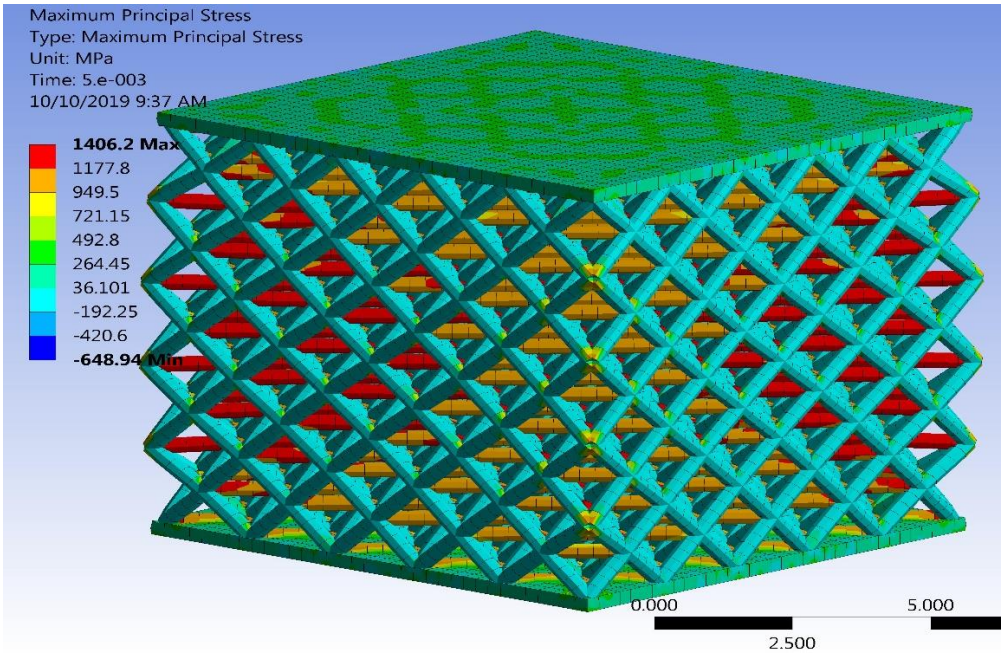

Figure 33: Maximum principal stress: 1D beam octet-truss lattice structure

On the other hand, the inclined struts in the side, edge and vertex unit cells are predominantly subjected to compressive stresses.

These results are similar to those of the 3D solid octet-truss lattice's maximum principal stress results. However, the magnitude of both the tensile and compressive stresses are higher for the 3D solid octet-truss lattice structure than those of the 1D octet-truss lattice structure.

Figure 34 shows the bending stress distribution for the 1D beam octet-truss lattice structure. From this figure, the horizontal struts in contact with the top and bottom platens experience the greatest amount of bending as compared to the rest of the struts.

Struts on the edge unit cells are also subjected to high bending stress whereas those of the side unit cells rather experience lower bending stresses.

Stellenbosch University https://scholar.sun.ac.za

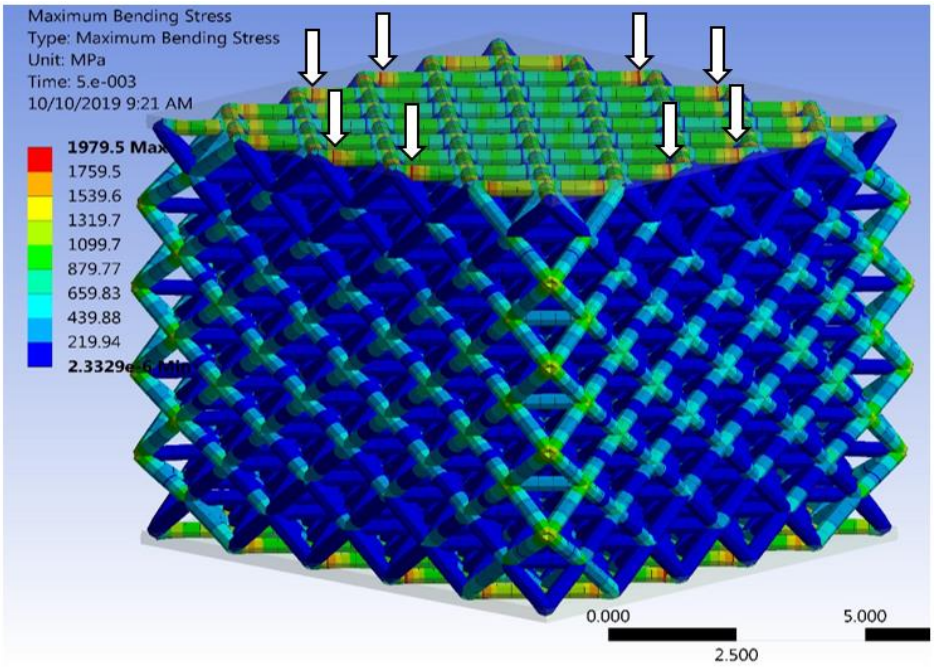

Figure 34: Maximum bending stress: 1D beam octet-truss lattice structure

The global behavior of the octet-truss lattice structure as predicted by the 1D beam design shows that the rectangular cross-section is slightly stiffer and stronger than the circular cross-section.

It also shows that, contrary to the octet-truss 3D solid results, the area under the stress-strain diagram for the 1D beam octet-truss increases as the loading increases. This increases the strain energy absorption of the structure before failure. This can be seen in Figure 35.

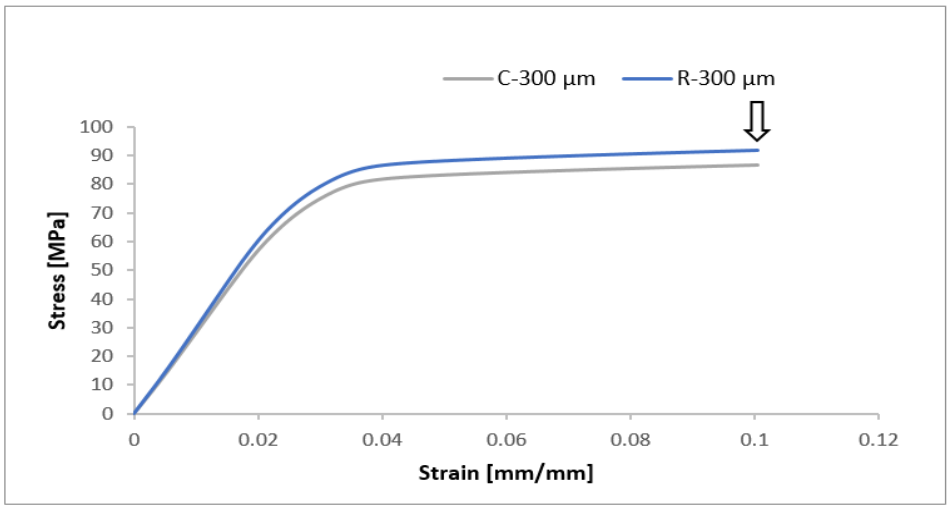

Figure 35: Direct stress-strain diagram: 1D beam octet-truss lattice structure

Stellenbosch University https://scholar.sun.ac.za

It is also important to note that there is a similarity in the global behavior of the octet-truss lattice structure as predicted by both the 3D solid and 1D beam design (see Table 6 and Table 8). This is very useful because a 1D beam structure can be used instead of the 3D solid structure to reduce the computational power and time required for acceptable approximations.

Table 8: Global mechanical properties: 1D beam octet-truss lattice structure

Topology	Cross-section	Young's modulus [GPa]	Yield strength [MPa]	Maximum stress [MPa]	Strain at maximum stress
Octet-truss	Rectangular	3.10	72.19	91.99	0.10
	Circular	2.95	67.16	86.87	0.10

Diamond lattice structure

Figure 36 shows the maximum principal stress distribution of the 1D beam diamond structure. From this figure, the struts in all unit cells in the structure show symmetric and even high-stress distribution. High tensile stress was observed along the length of the struts. The high compressive stress distribution is observed along the struts in the vertex and edge unit cells.

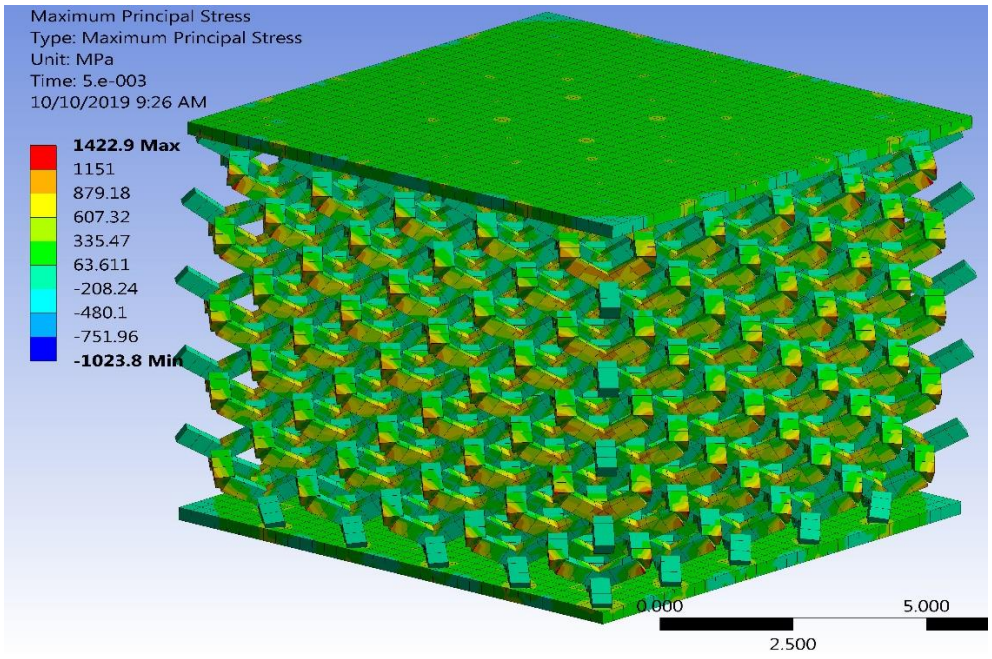

Figure 36: Maximum principal stress distribution: 1D beam diamond lattice structure

This is similar to the stress distribution of the 3D solid diamond structure result where the region of high-stress concentration was also determined to be the strut joints. However, the struts in the 3D solid structure sustain higher stresses than the 1D beam structure.

Stellenbosch University https://scholar.sun.ac.za

Figure 37 shows the maximum bending stress distribution across struts in the whole structure. This distribution is even, and the bending stresses are higher than the tensile and compressive stresses seen in Figure 36. This is an indication that deformation and failure of struts in the diamond lattice structure is caused by their bending behavior induced by the compressive load.

Comparing this result to that of the 3D solid lattice structure shown in Figure 30 allows a comparison of the two FEM modeling approaches. Figure 36 indicates that the struts were subjected to high tensile and compressive stress on either side of the strut cross-section neutral axis. This was an indication of strut bending, which is confirmed in Figure 37 with the high bending stresses induced in the 1D beam structure.

Additionally, both the 3D solid and 1D beam simulations of the diamond structure indicate high-stress concentrations at strut joints. The bending stress concentration can be seen at the strut joints as shown in Figure 37 by the arrows. This corresponds to the region of high-stress concentration of the maximum principal stress of the 3D solid structure in Figure 30.

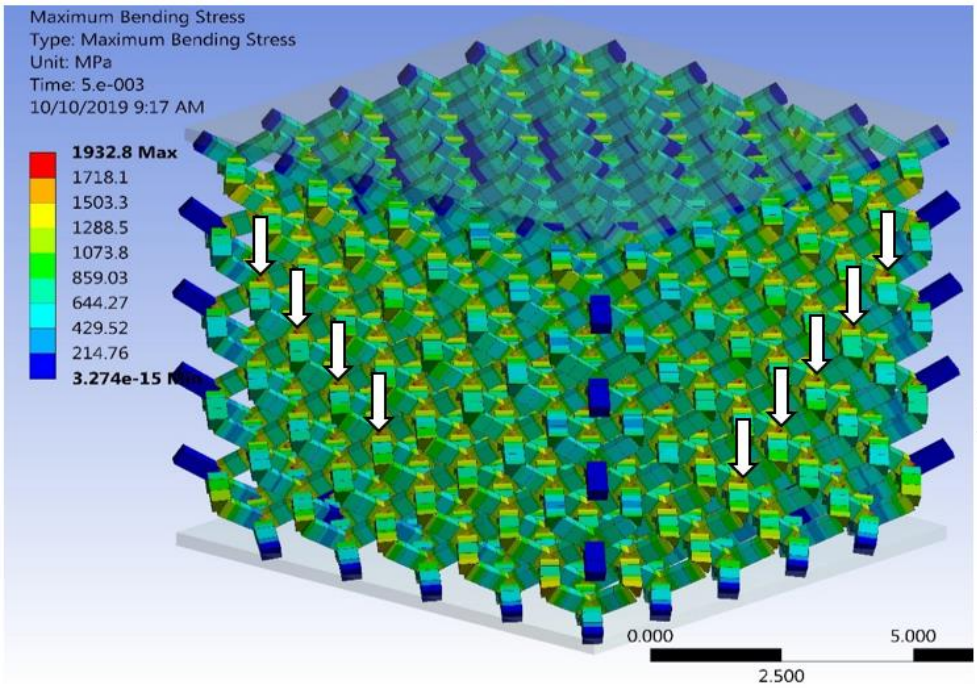

Figure 37: Maximum bending stress: 1D beam diamond lattice structure

The global behavior of the 1D beam diamond lattice structure can be seen in Figure 38 where the stress-strain diagram is given. Both cross-sections show similar results although the rectangular cross-section is slightly stronger than the circular cross-section.

Stellenbosch University https://scholar.sun.ac.za

The maximum stress is reached at the maximum strain for the applied compressive load. This behavior is similar to that of the 1D beam octet-truss lattice structure.

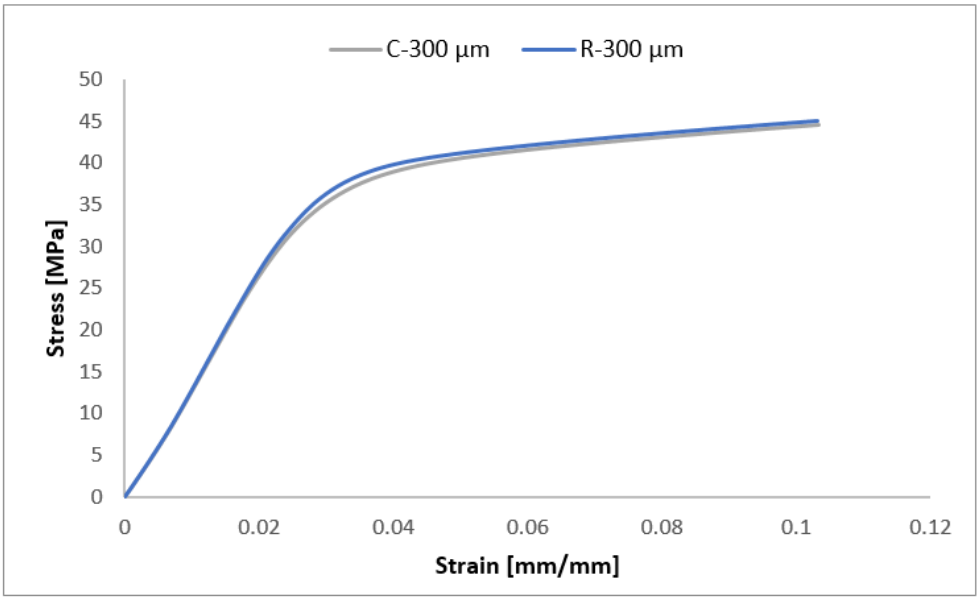

Figure 38: Stress-strain diagram: 1D beam diamond lattice structure

However, the slope of the strain hardening curve is steeper for a 1D beam diamond than that of the 1D beam octet-truss lattice structures. This indicates high specific strain energy.

The global mechanical properties are tabulated as seen in Table 9.

Table 9: Global mechanical properties: 1D beam diamond lattice structure

Topology	Cross-section	Young's modulus [GPa]	Yield strength [MPa]	Maximum stress [MPa]	Strain at maximum stress
Diamond	Rectangular	1.40	33.66	44.60	0.103
	Circular	1.43	31.67	45.10	0.103

Stellenbosch University https://scholar.sun.ac.za

4.3 Additive manufacturing (AM)

In this section, details about the production process of the lattice structures are presented, along with the powder characteristics and post-processing of the produced structure.

4.3.1 Powder characteristics

The lattice structures were produced through the fusion of grade 5 Ti6Al4V powder. The chemical composition of the powder, as provided by the supplier, is as presented in Table 10.

Table 10: Ti6Al4V powder chemical composition

Chemical composition	
Elements	Weight percentage (wt %)
Aluminum	6.32
Oxygen	0.11
Hydrogen	0.002
Nitrogen	0.03
Carbon	0.01
Iron	0.05
Titanium	Balance
Vanadium	4.06

The certificate of analysis and conformity from the supplier is provided in Appendix C.

4.3.2 Process technique and parameters

The CAD models of the lattice structures designed with the top and bottom compression platens as in Figure 23 and Figure 24 were converted into STL files and loaded into the software of the production machine.

The process parameters specified for L-PBF and heat treatment provided in section 3.2 were used to manufacture the samples. After the heat treatment, the structure and the build plate were cooled naturally for about 6 hours. The structures were then wire-cut from the build-plate.

Figure 39 and Figure 40 show the manufactured structures after heat treatment, diamond and octet-truss lattice structures, respectively.

Stellenbosch University https://scholar.sun.ac.za

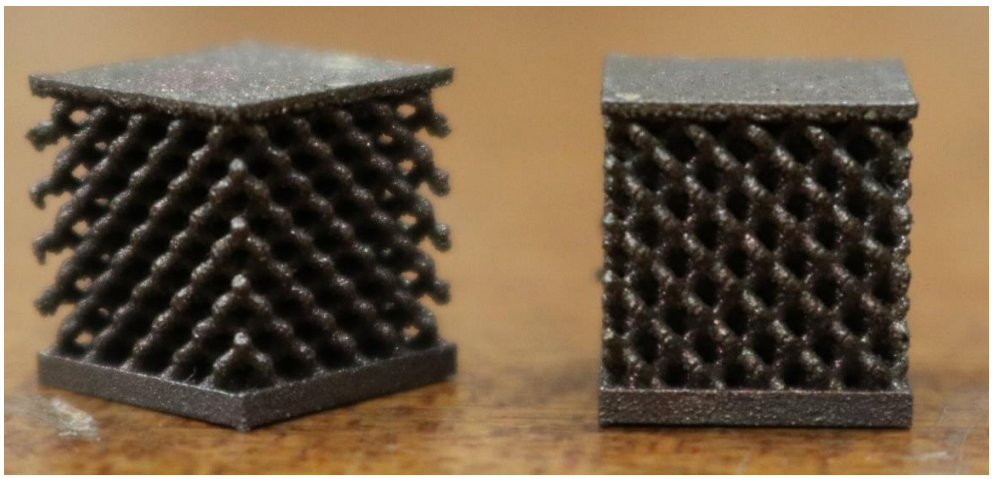

Figure 39: Additively manufactured (SLM) and heat-treated diamond lattice structure

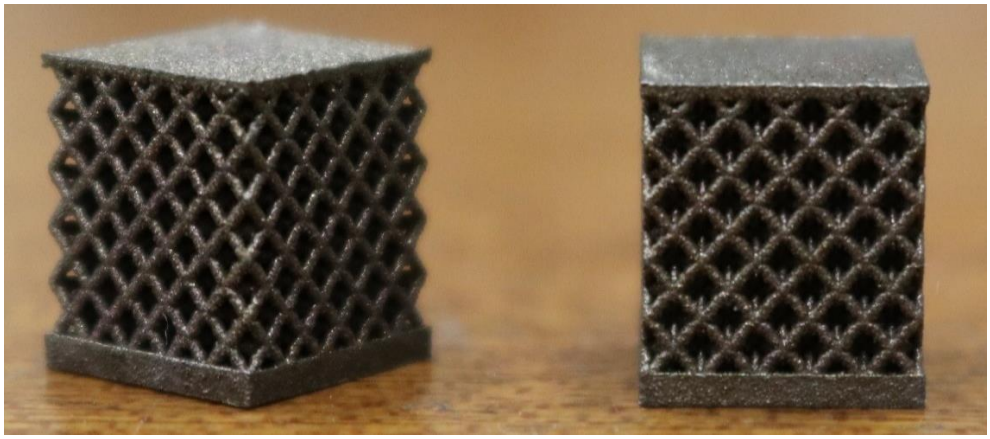

Figure 40: Additively manufactured (SLM) and heat-treated octet-truss lattice structure

4.4 Computed tomographic scan (CT-Scan)

The manufactured structures were CT-scanned for geometrical analysis using the Phoenix nanotom S (General Electric Sensing and Inspection Technologies/Phoenix X-ray, Wunstorff, Germany), a Nano-CT system available at the CT facility of Stellenbosch University [42].

4.4.1 CT-scanning process

As mentioned in the literature study, the scanning process was conducted using the guidelines provided in [38, 41]. However, based on the information provided in those studies, a brief explanation about the scanning process followed for the samples in this project is given here.

Stellenbosch University https://scholar.sun.ac.za

No special preparation was conducted on the lattice structure prior to the scanning process. The lattice structure was mounted on a low-density material (i.e. floral foam). The sample was tilted slightly to avoid parallel surfaces to the X-ray beam. This allows the X-ray to penetrate the sample and avoid artifacts in the captured images [44]. Table 11 shows the geometric data of the mounting of the lattice structure in the CT-scan machine and the X-ray data.

Table 11: Set-up data for CT-scanning of the lattice structure.

Geometric set-up					CT-scans		X-ray	
FDD [mm]	FOD [mm]	Magnification	Voxel size (X-axis)	Voxel size (Y-axis)	No. of images	Rotation of sample	Voltage (KV)	Current (µA)
219.99	52.79	4.17	0.0119	0.0119	2000	360	140	180

2D images of the lattice structure were projected to the detector by the X-ray. This continued until the entire lattice structure was rotated 360°. This allows for the capture of 2D images of the entire sample. These 2D images were then reconstructed using the system-supplied Datos reconstruction software package to produce a 3D volume of the CT-scanned lattice structure. Image Visualization and analysis were performed in Volume Graphics VGStudioMax 3.3.1.

Figure 41 and Figure 42 shows the 3D image of the diamond and octet-truss lattice structures as reconstructed and visualized.

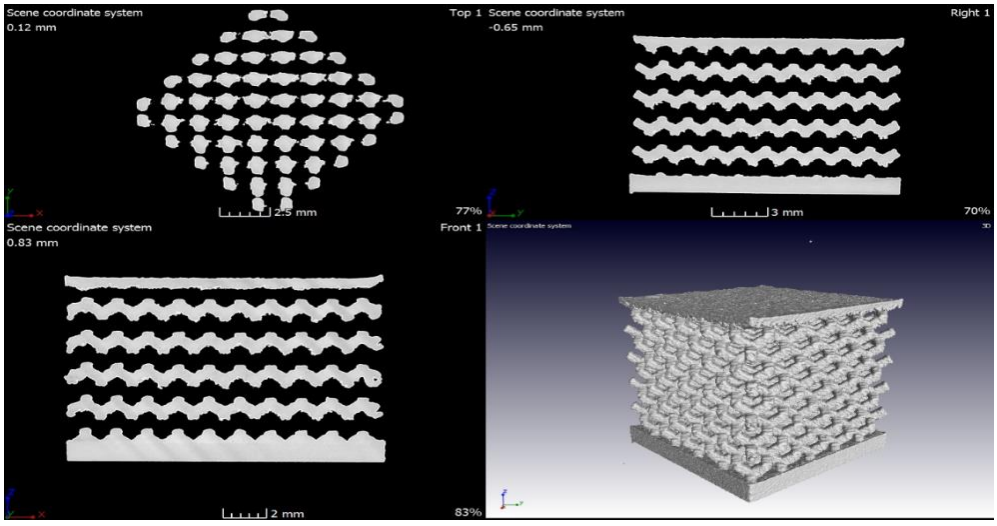

Figure 41: CT-scan data of diamond lattice structure

It is important to note that, for both diamond and octet-truss lattice structures, no apparent difference was observed between the circular and rectangular cross-sections as the CAD meshes show. This raises concerns about the

Stellenbosch University https://scholar.sun.ac.za

ability of the manufacturing technique and process parameters used to manufacture structures with different cross-sections.

Uneven distribution of the strut thickness was observed for both topologies, which is characteristic of the surface roughness produced by the manufacturing process.

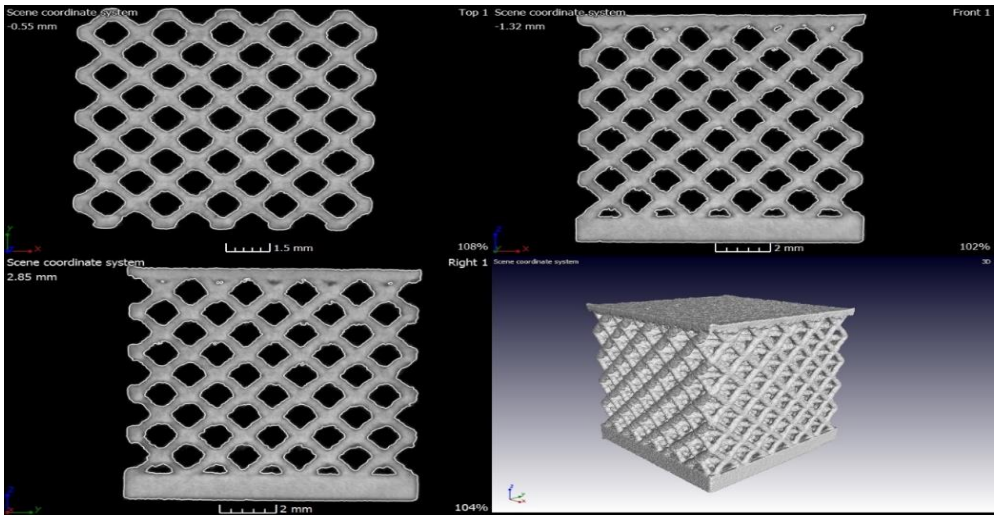

Figure 42: CT-scan of the octet-truss lattice structure

4.4.2 Geometric analysis of AM lattice structures

Using the geometric analysis module of Volume Graphics Max, a wall thickness analysis was conducted for both structures.

A region of interest (ROI) was created to focus our attention on the network of struts in the structures. Therefore, the dimensions are shown in both Figure 43 and Figure 44 are a variation of the strut thickness across all struts in the selected ROI.

Stellenbosch University https://scholar.sun.ac.za

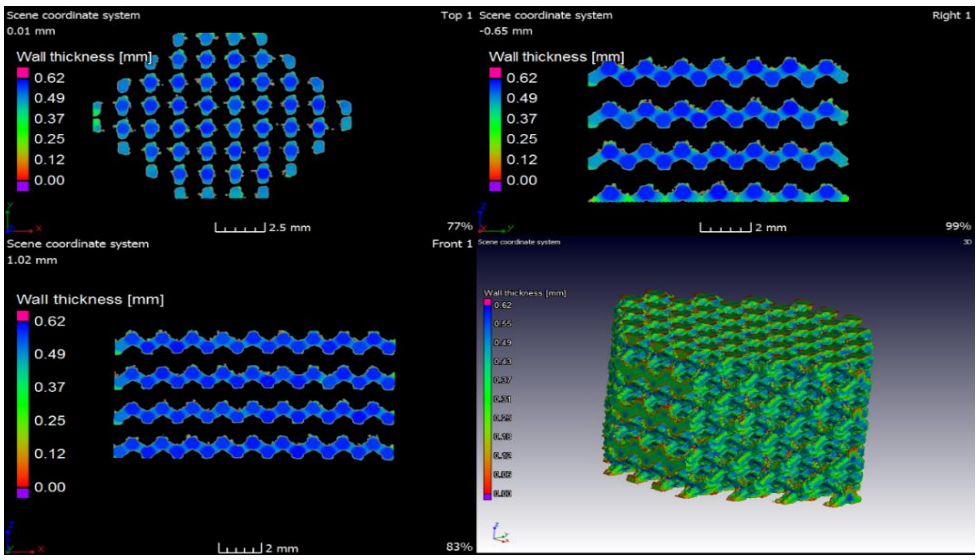

Figure 43: Wall thickness analysis result: Diamond lattice structure

For the diamond lattice structure, the manufactured strut thickness is observed to vary between 0.4 mm to 0.5 mm whereas that of that the octet-truss lattice structure varies between 0.32 mm and 0.45 mm.

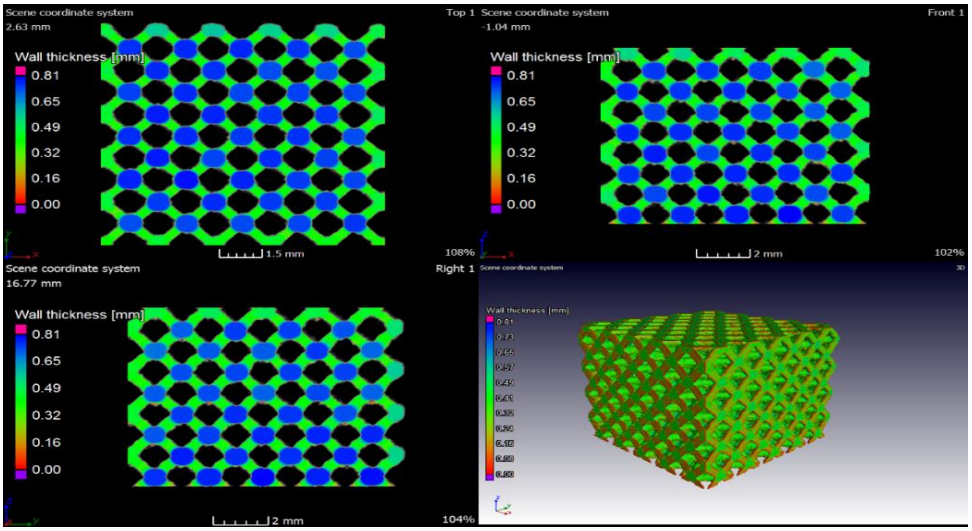

Figure 44 Wall thickness analysis result: octet-truss lattice structure

4.4.3 Comparison of AM lattice structure with CAD mesh

In order to obtain a clear idea of the geometrical difference between the CAD meshes and manufactured parts, a strut thickness deviation analysis that compares the actual produced parts' dimensions to those of the CAD models was conducted. The CAD mesh was imported into the VGStudioMax software space and registered. This registration helps to fit the CAD mesh with the CT-scanned and reconstructed structure as seen in Figure 45 and

Stellenbosch University https://scholar.sun.ac.za

Figure 46. Only the ROI was used in this case since the focus is on the struts. Using the nominal to actual comparison module of VGStudioMax, this comparison was conducted.

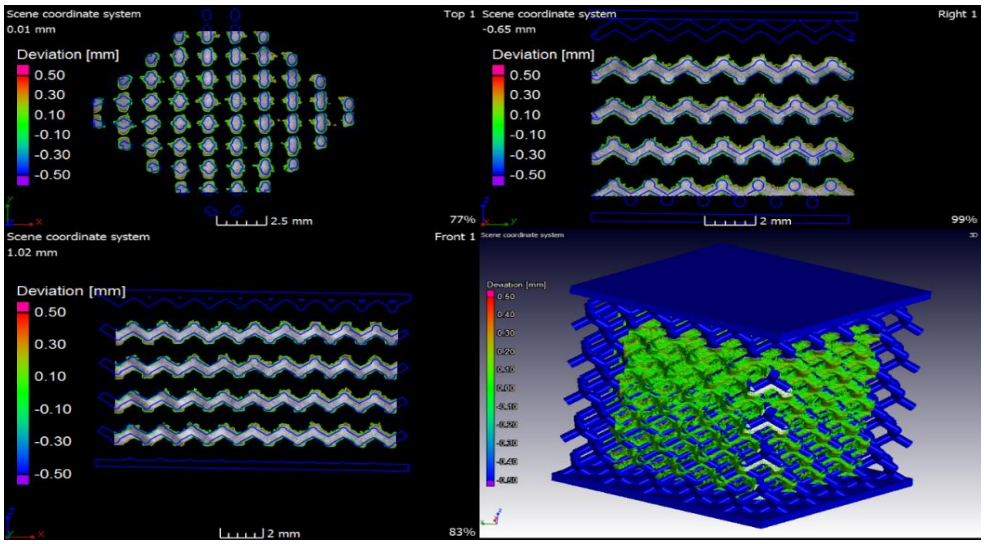

Figure 45: Strut thickness deviation analysis of the CT-scan volume of the manufactured structures and the 3D CAD mesh for diamond structure

A mean deviation of 79 µm and 66 µm was observed for the octet-truss and diamond lattice structures, respectively. This means that the strut thickness of the manufactured structures was bigger than that of the CAD meshes.

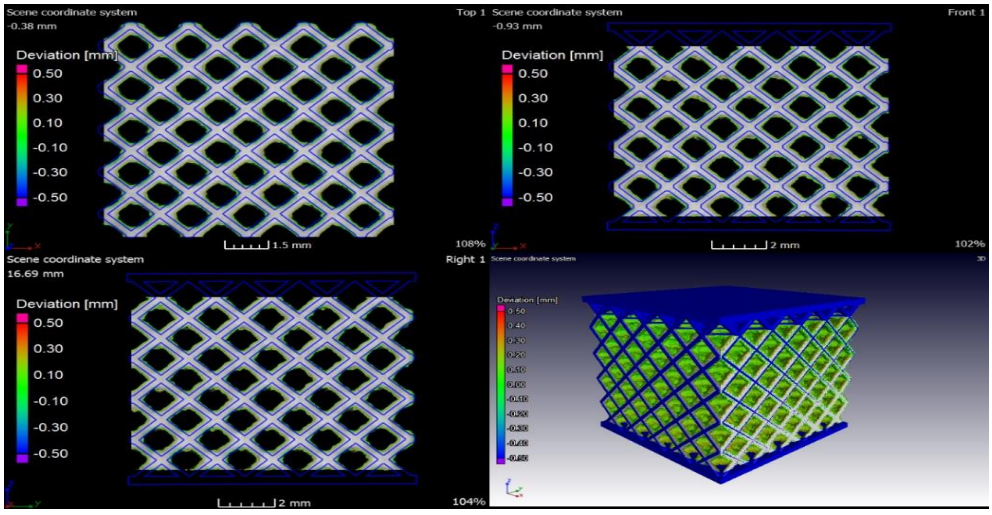

Figure 46: Strut thickness deviation analysis of the CT-scan volume of the manufactured structures and the 3D CAD mesh for the octet-truss structure

Stellenbosch University https://scholar.sun.ac.za

4.4.4 Design and FEA of manufactured dimensions

The results from the strut thickness analysis and the nominal to actual comparison analysis were used to design new lattice structures based on the manufactured dimensions. Exactly the mean deviation values reported above in section 4.4.3 were added to the strut thickness of Table 3.

The preliminary FEA results reported in section 4.2 show no major difference in the results for the circular and rectangular cross-sections and the CT-scan volume also show no apparent difference between the two manufactured cross-sections. Due to this reason, only circular cross-section was designed using the new dimensions.

New CAD models were obtained and new FEA compression simulations were conducted. The models were discretized with solid187 for the 3D solid models and beam188 for the 1D beam models. The same boundary conditions used in section 4.2 were used for the FEA compression simulation of the new models.

The maximum principal stress distribution and the plastic strain distribution across the strut network of the new models showed similar results as those reported in section 4.2.2 and section 4.2.3. However, their respective magnitudes varied proportionately with the variation in density.

The global response of the entire lattice structures is the only results reported in this section.

Octet-truss lattice structure

Figure 47 shows the global mechanical behavior of the new octet-truss lattice structure, as predicted by the 3D solid and 1D beam elements simulation. In terms of stiffness, the 3D solid structure is stiffer than the 1D beam while the 1D beam is stronger than the 3D solid structure.

Table 12 shows the global mechanical properties of the 3D solid and 1D beam structures

Stellenbosch University https://scholar.sun.ac.za

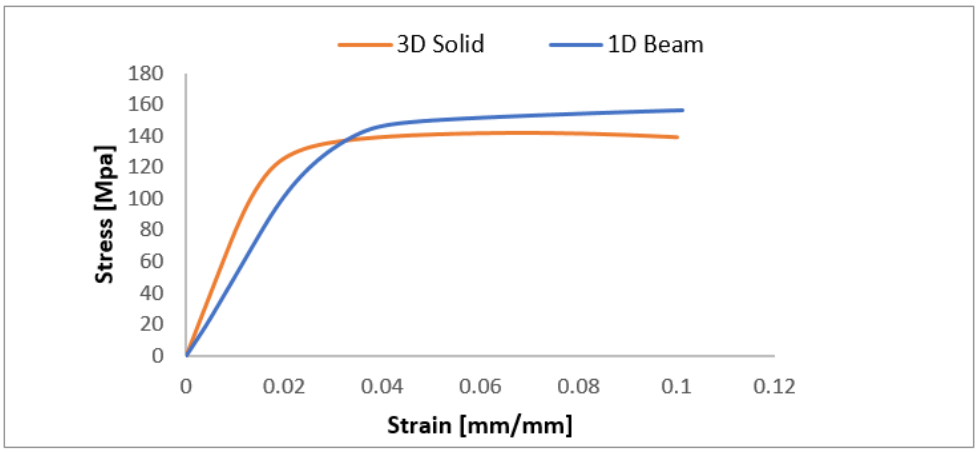

Figure 47: Stress-strain diagram of manufactured dimension: octet-truss lattice structure

Table 12: Global mechanical properties, manufactured dimensions: Octet-truss lattice structure

	Cross section	Young's modulus [GPa]	Yield strength [MPa]	Maximum stress [MPa]	Plateau stress [MPa]
3D Solid	Circular	7.5	120.99	141.76	140.61
1D Beam	Circular	5.1	124.69	156.36	149.60

Diamond lattice structure

Figure 48 shows the stress-strain diagram of the new diamond lattice structure, modeled with the manufactured dimensions. It is seen here that the 1D beam structure is less stiff and less strong than the 3D solid structure. However, both structures show a positive slope in the plastic region. This is indicative of a higher strain energy absorption.

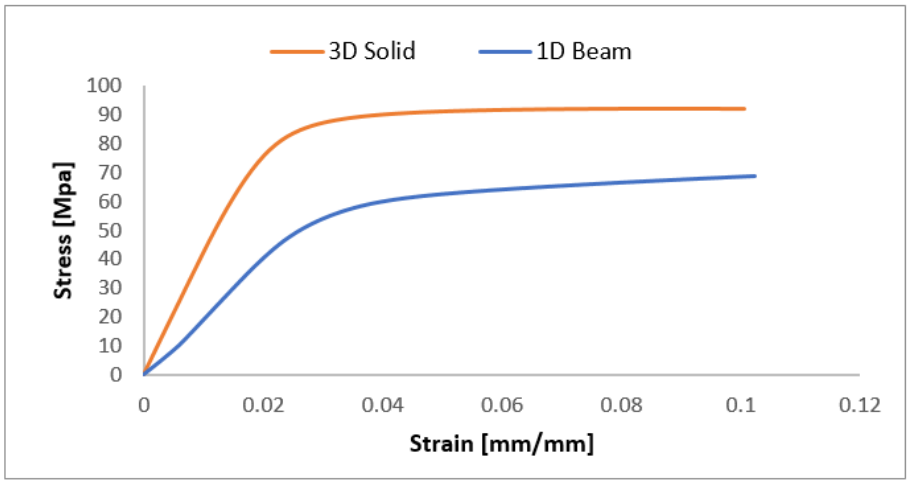

Figure 48: Stress-strain diagram of manufactured dimension: 3D solid and 1D beam diamond lattice structure

Stellenbosch University https://scholar.sun.ac.za

Table 13 shows the global mechanical properties of the diamond lattice structure as modeled with the manufactured dimensions.

Table 13: Global mechanical properties, manufactured dimensions: diamond lattice structure

	Cross-section	Young's modulus [GPa]	Yield strength [MPa]	Maximum stress [MPa]	Plateau stress [MPa]
3D Solid	Circular	3.9	79.9	92.30	91.3
1D Beam	Circular	2.1	49.6	80.5	62.2

4.5 Mechanical compression testing

This section describes the procedure followed in conducting the mechanical testing of the manufactured lattice structures and in the computation of their mechanical properties.

4.5.1 Testing procedure

The mechanical testing was conducted following the testing method presented in ISO standard (13314). Mechanical compression test rigs were manufactured out of steel as seen in Figure 49. The surfaces of both the top and bottom test rigs were ensured to be completely flat.

The mechanical testing was conducted using an MTS criterion Model 44 with a 30 kN load cell. The crosshead was set to a displacement rate of 1 mm/min. The load cell and displacement data were exported in the text file format from the Test-Work 4 (TW4) software package. This software package is used to control the testing machine and the hardware connected to it. Figure 49 shows the experimental set-up for mechanical compression testing.

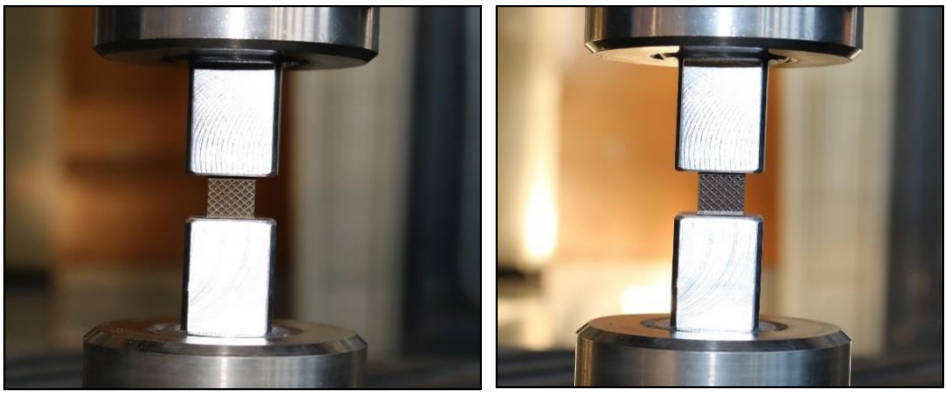

Figure 49: Experimental set-up for compression testing of the octet-truss (left) and diamond (right) lattice structures

Stellenbosch University https://scholar.sun.ac.za

4.5.2 Deformation and failure mechanisms

The deformation and failure mechanisms of the tested lattice structures are shown in Figure 50 and Figure 51 for the octet-truss and diamond lattice structures, respectively. Initially, the octet-truss shows strut bending along a diagonal plane 45° to the horizontal plane, then the bending of struts was also seen in the cross-diagonal plane 135° to the horizontal plane. Stretching was observed in almost all the horizontal struts in the fully compressed samples causing these struts to fail along their lengths.

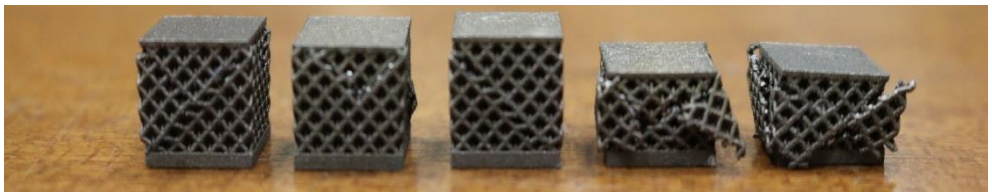

Figure 50: Failed octet-truss lattice structure samples.

Crushing or brittle fracture of struts was observed at the bottom of the structure adjacent to the bottom compression platen.

For the diamond lattice structure, a single dominant mode of failure was observed in many tested samples. Bending of struts along diagonal planes 45° to the horizontal plane occurred. Failure was seen to initiate at the strut joint. Struts were mostly seen to be bending about the strut joints.

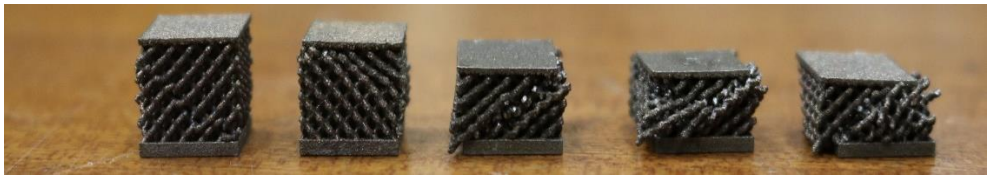

Figure 51: Failed diamond lattice structure samples.

4.5.3 Mechanical properties

The mechanical properties of the tested samples were obtained as prescribed in ISO standard (13314). The evolution of the mechanical properties for both structures is as seen in Figure 52.

Stellenbosch University https://scholar.sun.ac.za

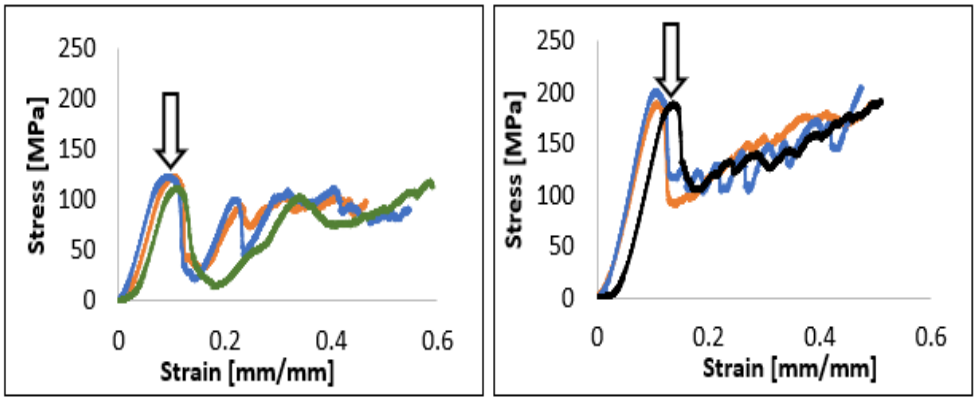

Figure 52 Stress-strain diagram for the mechanical testing result: diamond (left) and octet-truss (right) lattice structure

The global mechanical properties of both tested structures are as presented in Table 14.

Table 14: Global mechanical properties of fully compressed octet-truss and diamond lattice structures

Topology	Young's modulus [GPa]	Yield strength [MPa]	Maximum stress [MPa]	Plateau stress [MPa]
Octet-truss	2.4	184.06	196.60	188.97
Diamond	1.8	107.10	121.11	117.49

Stellenbosch University https://scholar.sun.ac.za

5 Results and Discussions

In the following chapter, the compressive behavior of LPB-F lattice structures, as predicted by the FEM simulation, is discussed. A comparison of the FEM results and mechanical testing results constitutes the main part of this chapter. The influence of manufacturing process parameters is also discussed.

5.1 Effect of strut cross-sections on lattice structure behavior

The preliminary FEM results show minor differences in the mechanical properties between the rectangular and circular strut designs. A difference of 5% or less was observed between the rectangular and circular lattice structures. This was found to be common in both the 3D solid and 1D beam elements FEA simulations.

Figure 53 shows the stress-strain diagram of both the 1D beam circular and rectangular octet-truss lattice structure. It is seen that the rectangular structure is stiffer, stronger than the circular structure.

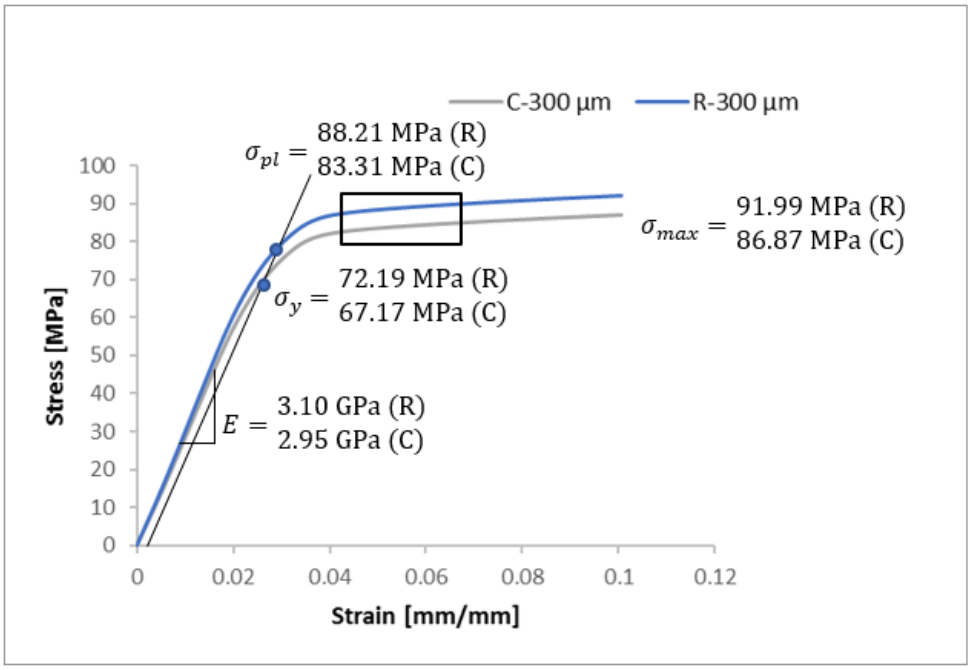

Figure 53: Effect of strut cross-section on the mechanical properties of 1D beam octet-truss lattice structures

This trend is repeated for other structures modeled as a 3D solid or 1D beam. Table 15 and Table 16 highlight the minor differences between the mechanical properties of the rectangular and circular cross-sections of both lattice structures.

Stellenbosch University https://scholar.sun.ac.za

Table 15: 1D beam circular and rectangular octet-truss and diamond lattice structures

Topology	Cross-section	Young's modulus [GPa]	Yield strength [MPa]	Maximum stress [MPa]	Plateau stress [MPa]
Octet-truss	Rectangular	3.10	72.19	91.99	88.21
	Circular	2.95	67.17	86.87	83.31
Diamond	Rectangular	1.40	33.66	44.60	41.17
	Circular	1.40	31.66	45.10	40.52

Table 16: 3D solid circular and rectangular octet-truss and diamond lattice structures

Topology	Cross-section	Young's modulus [GPa]	Yield strength [MPa]	Maximum stress [MPa]	Plateau stress [MPa]
Octet-truss	Rectangular	4.32	74.70	93.22	87.92
	Circular	4.20	75.35	92.57	86.60
Diamond	Rectangular	2.38	51.10	65.01	60.38
	Circular	2.46	54.48	68.89	63.80

5.2 Effect of Ti6Al4V material properties on FEM results

Material properties in material libraries of FEM software packages are usually those of the wrought material and not additively manufactured material. Research studies have shown that additively manufactured Ti6Al4V material will have different material properties depending on what heat treatment process it is subjected to [1,2]. This is crucial information when attempting to predict the global mechanical properties of additively manufactured Ti6Al4V lattice structures. Lattice structures in the present study were additively manufactured (SLM) from Ti6Al4V powder. These structures were subjected to a stress relief heat treatment. Therefore, the material properties of stress relieved Ti6Al4V were used.

In order to determine the sensitivity of FEM compression simulations to material property variations, two sets of data were used. First, a wrought Ti6Al4V material yield strength of 950 MPa [60] was used and then stress relieved SLM Ti6Al4V material yield strength of 1145 MPa [58] was used. In both cases, the global mechanical properties of the lattice structure were determined. A significant difference was observed in the results.

A percentage error of about 15.81% between the maximum stresses, 7.5% between Young's moduli, 13.4% between the yield strengths of the diamond structures was observed using a 1D beam element simulation. For the 3D solid diamond lattice structure, a percentage error of 14.16% between the maximum stresses, 14.6% for the yield strengths and 8% for Young's moduli was observed. This is seen in Figure 54 below.

Stellenbosch University https://scholar.sun.ac.za

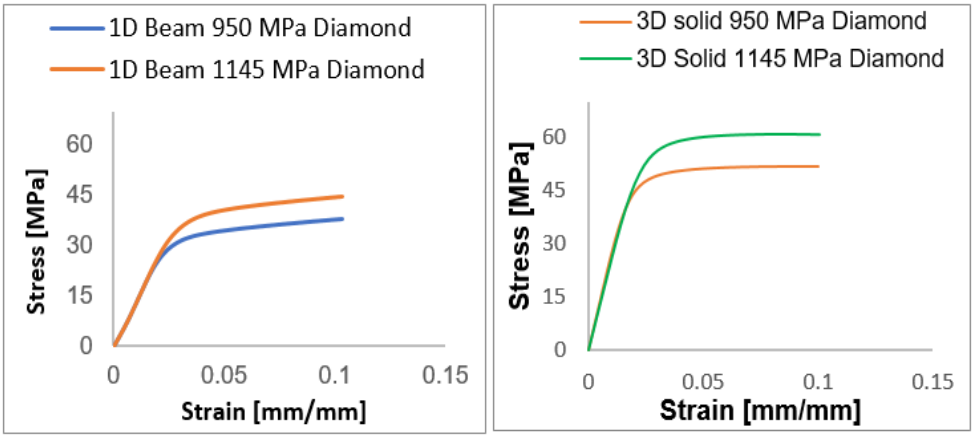

Figure 54: Effects of Ti6Al4V material properties on FEM results: 1D beam (left) and 3D solid (right) diamond lattice structure

Similar trends were observed for the octet-truss lattice structure as seen in Figure 55. For the 1D Beam structure, a percentage error of 8.8% for Young's moduli, 10.45% between the yield strengths and 16% between the maximum stresses was observed. For the 3D solid structure, a percentage error of 2.2% between Young's moduli, 15.97% percentage error in the yield stresses, 9.68% between the maximum stresses was observed. This speaks to the importance of specifying the right material properties for FEM simulation purposes. The material properties of stress relieved Ti6Al4V were used for all further simulations, as reported in Chapter 4 section 4.2, as they more closely matched the experimental results.

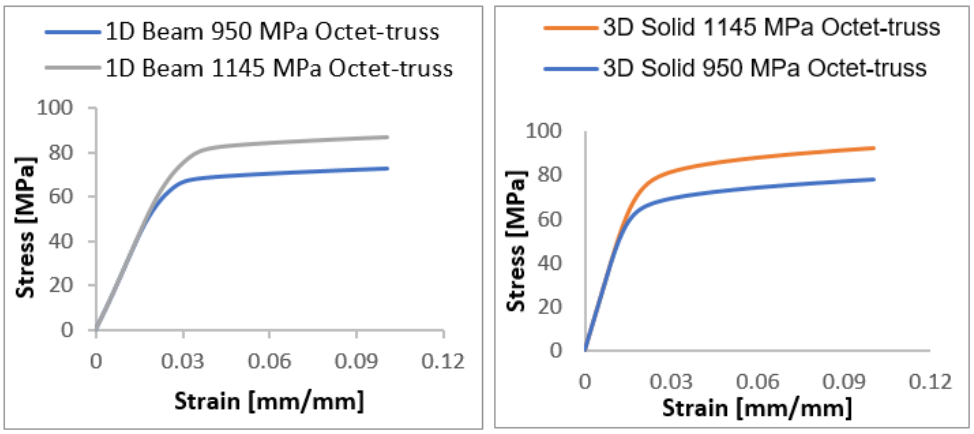

Figure 55: Effects of Ti6Al4V material properties on FEM results: 1D beam (left) and 3D solid (right) octet-truss lattice structure

Stellenbosch University https://scholar.sun.ac.za

5.3 Effect of dimensional variations of strut thickness on FEM analysis

As reported in Chapter 4, section 4.4, the struts of manufactured lattice structures were, on average, larger than that specified in the 3D CAD design. A mean deviation margin of 78.9 µm and 65.9 µm was observed across a range of struts for the octet-truss and diamond structures, respectively. This is an increase in the strut thickness of 29.0% and 15.6% for the octet-truss and diamond lattice structure, respectively. This results in an increase in the relative density of the structures. The global behavior of the structure is expected to increase proportionately with this increase in the relative density. Table 17 and Table 18 shows the global mechanical properties of the diamond and octet-truss lattice structures, respectively. The percentage error is also reported.

Table 17: Comparison of FEM predictions of designed dimensions (nominal) and produced dimensions (actual): 1D Beam and 3D Solid Diamond lattice structure

Diamond Lattice structure						
Dimension	FEM element	Relative Density [%]	Young's modulus [GPa]	Yield strength [MPa]	Maximum stress [MPa]	Plateau stress [MPa]
Nominal	3D Solid	20.12	2.5	54.5	68.89	63.79
Actual	3D Solid	26.00	4.43	81.21	102.44	95.91
% Error			43.57	32.89	32.75	33.49
Nominal	1D Beam	24.30	1.4	31.67	45.1	40.52
Actual	1D Beam	32.66	2.1	49.56	80.46	62.21
% Error			33.33	36.1	43.95	34.87

Figure 56 and Figure 57 show the predicted global stress-strain diagrams for both diamond and octet-truss structures, respectively, using both 1D beam and 3D solid element FEM. It can be seen that the CAD models used as input to the production machine, are less stiff, less strong than the CAD models designed using the actual dimensions (produced dimensions). This is crucial information in studying the accuracy of FEM predictions of the global behavior of lattice structures.

Stellenbosch University https://scholar.sun.ac.za

Table 18: Comparison of FEM predictions of designed dimensions (nominal) and produced dimensions (actual): 1D Beam and 3D Solid Octet-truss lattice structure

Octet-truss Lattice structure						
Dimension	FEM element	Relative Density [%]	Young's modulus [GPa]	Yield strength [MPa]	Maximum stress [MPa]	Plateau stress [MPa]
Nominal	3D Solid	21.50	4.2	72.38	92.57	86.59
Actual	3D Solid	33.66	7.4	128.1	157.61	147.25
% Error			43.24	43.5	41.27	41.2
Nominal	1D Beam	26.33	2.95	67.17	86.87	83.31
Actual	1D Beam	44.39	5.1	127.34	156.36	149.6
% Error			42.16	47.25	44.44	44.31

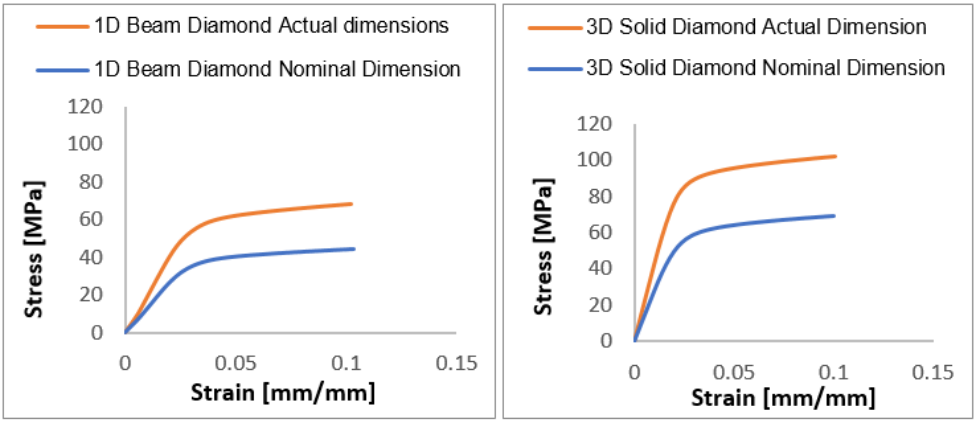

Figure 56: Comparison between the FEM global response of the designed dimension (nominal) and produced dimension (actual): diamond lattice structure

Stellenbosch University https://scholar.sun.ac.za

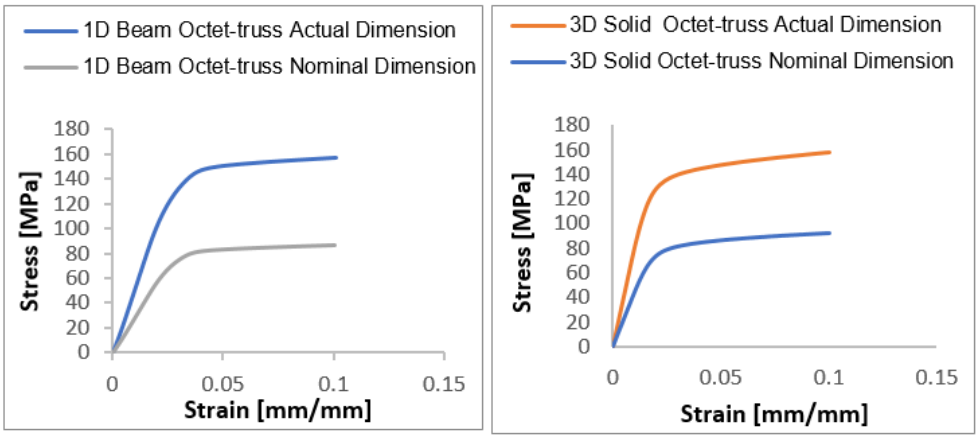

Figure 57: Comparison between the FEM global response of the designed dimension (nominal) and produced dimension (actual): Octet-truss lattice structure

5.4 Lattice structure deformation mechanisms

In order to determine the deformation mechanisms of lattice structures, we considered geometric non-linearity for the FEM simulations. This was considered together with the material non-linearity.

With geometric non-linearity, it was possible to determine how and where the structures would fail. Geometric non-linearity, in the FEM simulation, tracks changes in the geometry of the structures. These geometric changes can indicate regions of high-stress concentration and deformation initiation sites in the structures.

Such FEM simulations were conducted and predictive information about the deformation mechanisms of both structures was obtained.

For both the diamond and octet-truss lattice structures, the plastic strain results were obtained from the 3D solid FEM simulation. These results give an indication of the first signs of yielding in the structure.

For the diamond lattice structure as seen in Figure 58, strut joints are the regions of high plastic strains. Yielding is to be expected in these regions. As mentioned in section 4.2.2, these strut joints are oriented in 45° planes with the horizontal plane. This forms 45° shear bands across these planes.

Stellenbosch University https://scholar.sun.ac.za

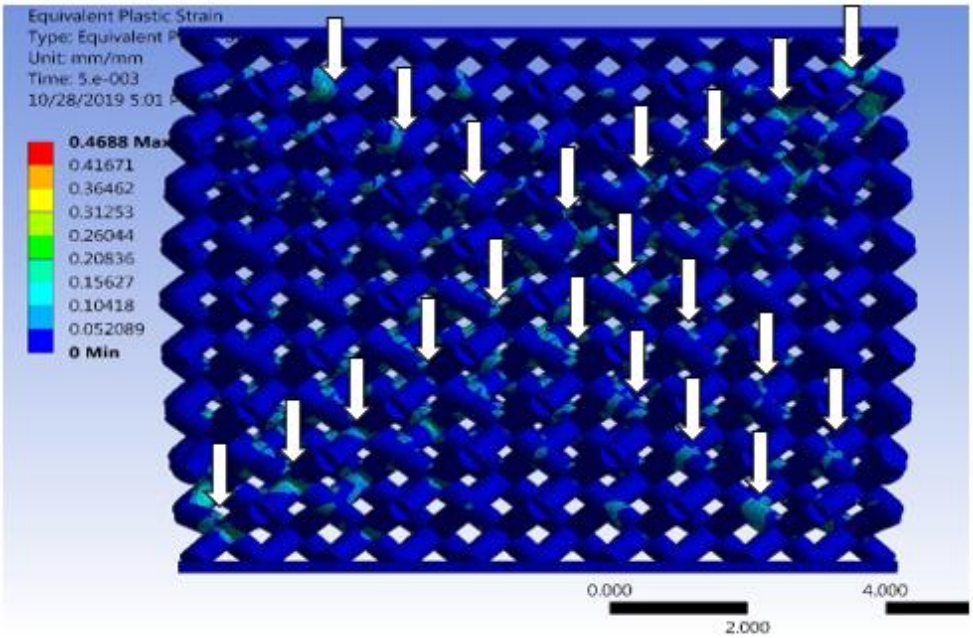

Figure 58: Deformation mechanism and failure initiation sites: Diamond lattice structure

The localization of high plastic strains at the strut joints can be related to the maximum principal stress distribution results of the 1D beam simulation reported in section 4.2.3. These results show the struts subjected to high tensile and compressive stresses on the top and bottom surface of the cross-section. It is mentioned in the same section that this is indicative of strut bending about the strut joints. These strut joints are subjected to high tensile stresses. This causes yielding to occur in these regions as is seen in Figure 58. Figure 59 shows the actual deformation mechanism of the diamond lattice structure. It is seen from all 5 samples in the figure that there is a common pattern of 45° shear bands forming until the structure is fully compressed.

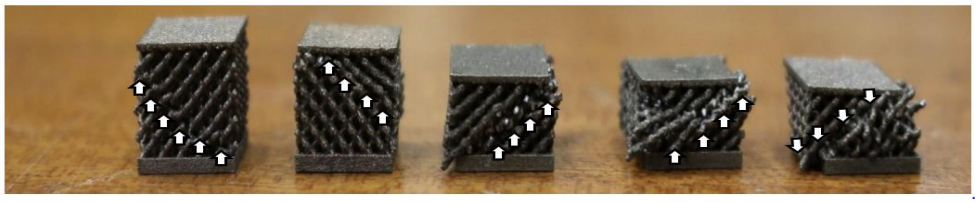

Figure 59: Actual deformation mechanism of the diamond lattice structure

Figure 60 shows the deformation mechanism of the octet-truss lattice structure as predicted by the distribution of the equivalent plastic strain across the entire network of struts. In section 4.2.2 and section 4.2.3, the maximum principal stress distribution is described for the 3D Solid and 1D Beam structure, respectively. In these results, it is observed that the highest

Stellenbosch University https://scholar.sun.ac.za

stresses were the tensile stresses induced in the horizontal strut of the octahedral section of the lattice structure. In addition to those results, is the distribution of the equivalent plastic strain in the strut. These results provide information about the deformation behavior of the structure. As seen in Figure 60 below, regions of high plastic strain as indicated by the arrows are indeed the horizontal struts of the octahedral section of the structure. A cross-diagonal picture is drawn as seen in Figure 60 which is the deformation mechanism.

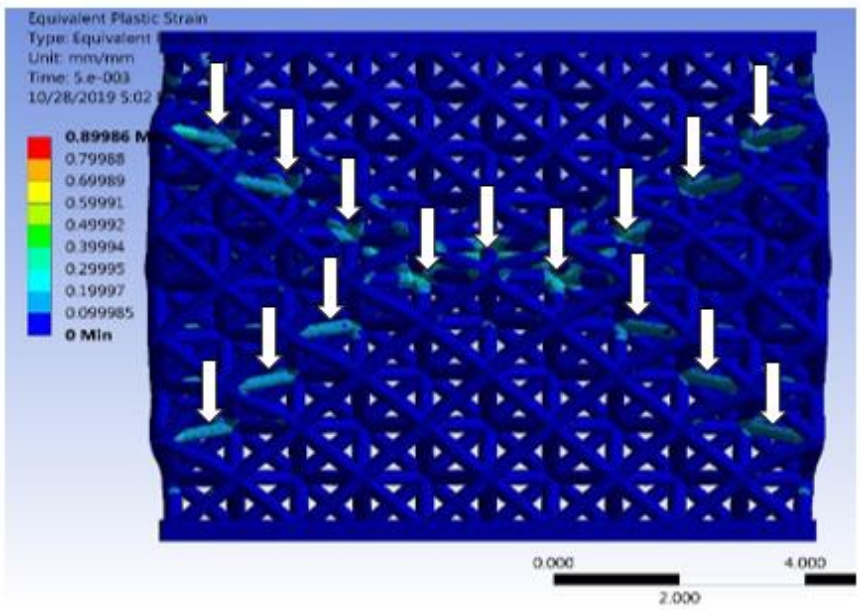

Figure 60: Deformation mechanism and failure initiation sites: Octet-truss lattice structure

Figure 61 shows the actual deformation mechanism of the octet-truss samples. It is seen from the first picture that the cross-diagonal pattern reported above is forming. The second picture shows the top triangular block of the cross-diagonal collapsing. The last 2 pictures of the figure clearly show the complete deformation mechanism of the octet-truss lattice structure as predicted by the FEM results.

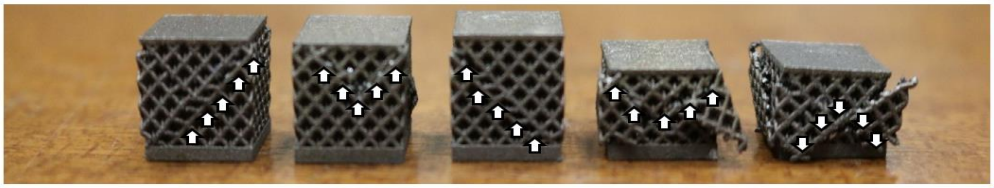

Figure 61: Actual deformation mechanism of the octet-truss lattice structure

Stellenbosch University https://scholar.sun.ac.za

With the equivalent plastic strain distribution results, the maximum principal stress distribution, it is possible to predict the deformation mechanism of lattice structures.

In order to further confirm the maximum stress distribution as predicted by FEM analysis, a network of struts from the fully compressed diamond lattice structure was CT-scanned. The results as seen in Figure 62, show cracks initiating at strut joints. This agrees with the FEM maximum principal stress distribution and equivalent plastic strain results.

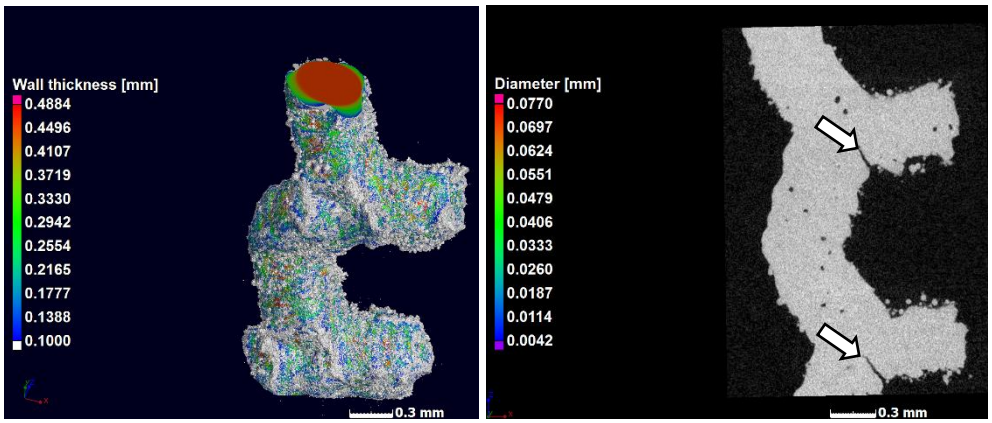

Figure 62: CT Scan of a series of struts showing the crack propagation at the strut joints.

5.5 FEM and experimental global mechanical properties of lattice structures

A comparison of the global mechanical properties from the mechanical testing results and those obtained from the FEM simulation is presented here. The red region in Figure 63 (left) and Figure 64 (left) represent the FEA simulated behavior up to 0.1 strain.

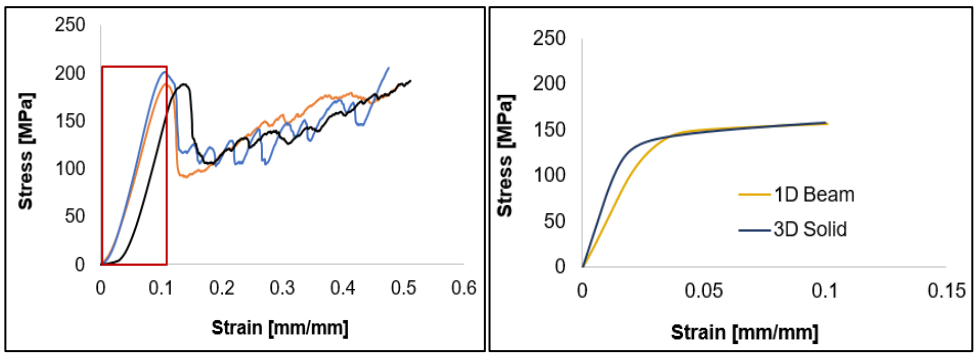

Figure 63: Stress-strain diagram of the octet-truss lattice structure: mechanical testing (left) and FEM (right)

Stellenbosch University https://scholar.sun.ac.za

Table 19 and Table 20 show the global mechanical properties of the octet-truss and diamond lattice structures, respectively. For the octet-truss lattice structure, both the 3D solid and 1D beam FEM predictions report approximately the same mechanical behavior as seen in Figure 63 and the numerical values in Table 19. This is true for the prediction of the structure yield strength, maximum stress, plateau stress, where both registered the same percentage error. However, the predicted Young's modulus by both 3D Solid and 1D Beam element FEM simulations are higher than the actual Young's modulus by 208.33% and 112.5%, respectively.

Table 19: FEM predictions and actual mechanical properties: Octet-truss lattice structure

Octet-truss Lattice structure						
Parameter		Strut Thickness [µm]	Young's modulus [GPa]	Yield strength [MPa]	Maximum stress [MPa]	Plateau stress [MPa]
Physical Testing			2.4	184.06	196.6	188.97
FEM	3D Solid	347	7.4	128.1	157.61	147.25
% Error			208.33	-30.4	-19.83	-22.08
FEM	1D Beam	347	5.1	127.34	156.36	149.6
% Error			112.5	-30.82	-20.47	-20.83

For the diamond lattice structure, the 3D Solid results are within acceptable error range whereas the 1D beam results are off by large amount as compared to the actual properties of the structures. The 3D solid predicted yield strength, plateau, and maximum stresses are all within less than 25% error whereas, for the 1D beam, the percentage error is more than 30%. Similar to the octet-truss, the FEM predicted stiffness is higher than the actual stiffness of the structure for the 3D Solid by 146.11% whereas for the 1D beam the predicted stiffness is higher by just 16.67%. This is seen in Figure 64 and the numerical values in Table 20.

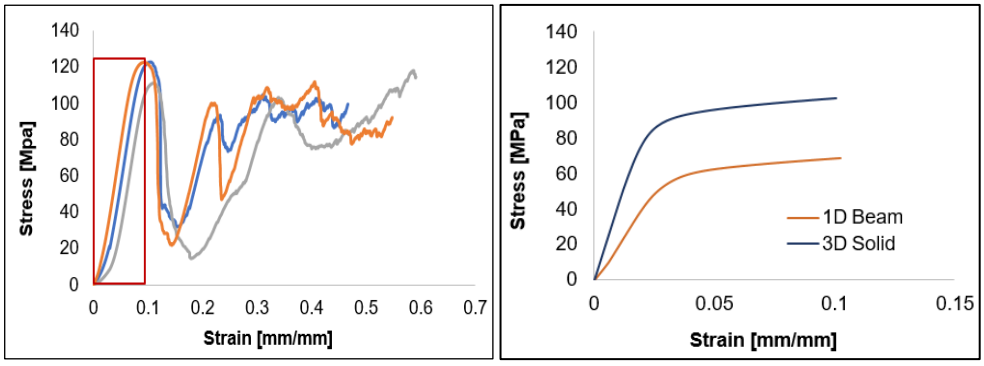

Figure 64: Stress-strain diagram of the diamond lattice structure: mechanical testing (left) and FEM (right)

Stellenbosch University https://scholar.sun.ac.za

Table 20: FEM predictions and actual mechanical properties: Diamond lattice structure

Diamond Lattice structure						
Dimension		Strut Thickness [µm]	Young's modulus [GPa]	Yield strength [MPa]	Maximum stress [MPa]	Plateau stress [MPa]
Physical Testing			1.8	107.1	121.11	117.49
FEM	3D Solid	489	4.43	81.21	102.44	95.91
% Error			146.11	-24.17	-15.42	-18.37
FEM	1D Beam	489	2.1	49.56	80.46	62.21
% Error			16.67	-53.73	-33.56	-47.05

The over-estimation of the stiffness in simulations as reported above can be attributed to various factors such as imperfections induced by the production technique. These imperfections include pores in struts, uneven and rough strut surface and the role of microstructure. The CAD model of the structure used in the FEM simulation is a perfect structure with an even strut surface, fully dense struts with no defects.

Stellenbosch University https://scholar.sun.ac.za

6 Conclusion and recommendation

6.1 Conclusion

The assessment of the FEA approaches in the prediction of the mechanical behavior of the Ti6Al4V octet-truss and diamond lattice structures, produced through laser powder bed fusion, was the main objective of the present research project. Octet-truss and diamond lattice structures of fixed porosity and strut thickness were selected and designed using an iterative process of calculating the strut volume as a function of thickness until the desired structure was obtained. Design equations were derived, that were based on this process. FEA compression simulations were conducted using ANSYS academic research Mechanical and CFD (structural/LS-Dyna).

Preliminary FEA results show that the selected Ti6Al4V material properties and plasticity model predicted the mechanical properties within a reasonable error margin. The selected material properties and plasticity model gave ample information about the stress and strain distribution across each strut in the structure in order to assess the critical regions in terms of predicting failure. This information and theories relating to solid mechanics were used to predict the deformation mechanisms of the entire structures. These agreed with the deformation mechanisms observed during mechanical testing.

Following critical factors were observed for each lattice topology:

1. The prediction of the mechanical properties of diamond lattice structures was achieved using the 3D solid elements. A percentage error of less than 25% was reported on the plateau, yield and maximum stress. On the other hand, the 1D beam elements could not predict these properties within that error margin. Using the maximum principal stress distribution from both simulation methods (3D solid and 1D beam methods), the nature of failure in the struts was determined. The diamond was confirmed to be bending dominated, as is predicted by the Maxwell criterion for this lattice design. This was determined by studying the stress distribution across each strut. Maximum compressive and tensile stress occurred on opposite sides of the strut. This trend was uniform across each strut. From solid mechanics, this stress distribution aligns with the behavior of a beam under a bending load. From the plastic strain result, regions of high-stress concentration were found at the strut joints. The stresses at these joints were tensile. These high stresses induced high distortion in these strut joints.
2. The octet-truss lattice structures mechanical properties were successfully predicted by both the 3D solid and 1D beam elements within an error margin of less than 30 %. In the following case, preference is given to the 1D beam model since the computation time was less than the 3D solid model. The maximum principal stress distribution across each strut was studied to determine the deformation mechanism of the structure. The failure initiation regions were mostly in the horizontal struts of the structure. These struts were mostly subjected to high tensile stresses. The equivalent plastic strain results from the 3D

Stellenbosch University https://scholar.sun.ac.za

solid model gave a clear indication of the regions sustaining extreme distortion during the loading process. Horizontal struts in unit cells located at 45° and 135° to the horizontal plane experience high distortion.

It is important to note that in both cases, the structure's stiffness, as evaluated by Young's modulus, was over-estimated by both FEA approaches and did not match the experimentally measured stiffness. This can be attributed to factors such as strut surface roughness and waviness, strut uneven thickness, strut porosity. No further investigation was conducted in determining the underlying cause of this and this remains an area for further study.

To arrive at these conclusions about the mechanical properties and deformation mechanisms of lattice structures, different design, and FEA techniques were employed. Figure 65 shows the flowchart of the successful technique used in the study for the analysis of the mechanical behavior of lattice structures. This can be applied for the analysis of the compressive behavior of other lattice structures.

Stellenbosch University https://scholar.sun.ac.za

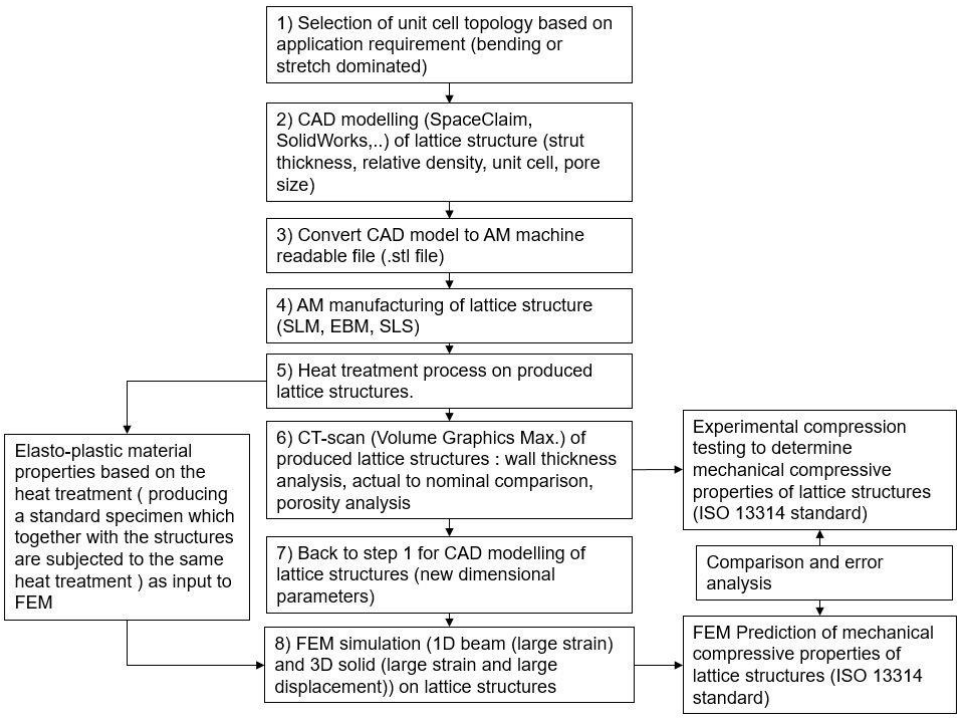

Figure 65: Flowchart for the FEM analysis of mechanical properties of lattice structures

6.2 Recommendation

The production of lattice structures is possible through additive manufacturing technologies. This process can yield good structural integrity. It is then important to understand their behavior to various load conditions. This study only considered their behavior to compressive load. More studies are required to understand their behavior under different loading conditions.

It is also known that lattice structures do not perform well under dynamic loading. More studies are required on their design for dynamic loading and their dynamic behavior.

More studies on the influence of process parameters on their mechanical behavior are required.

CAD designs that can incorporate factors such as strut surface roughness and waviness, uneven strut thickness need to be investigated.

Stellenbosch University https://scholar.sun.ac.za

7 References

[1] L. J. Gibson and M. F. Ashby, *Cellular solids : structure and properties*. Cambridge University Press, 1997.

[2] C. Neff, N. Hopkinson, and N. B. Crane, “Experimental and analytical investigation of mechanical behavior of laser-sintered diamond-lattice structures,” *Addit. Manuf.*, vol. 22, no. March, pp. 807–816, 2018.

[3] L. Zhu, N. Li, and P. R. N. Childs, “Light-weighting in aerospace component and system design,” *Propuls. Power Res.*, vol. 7, no. 2, pp. 103–119, 2018.

[4] L. E. Murr *et al.*, “Next-generation biomedical implants using additive manufacturing of complex cellular and functional mesh arrays,” *Philos. Trans. R. Soc. A Math. Phys. Eng. Sci.*, vol. 368, no. 1917, pp. 1999–2032, 2010.

[5] A. du Plessis, I. Yadroitsava, and I. Yadroitsev, “Ti6Al4V lightweight lattice structures manufactured by laser powder bed fusion for load-bearing applications,” *Opt. Laser Technol.*, vol. 108, pp. 521–528, 2018.

[6] A. Burakowski *et al.*, “Surface Modification of Ti6Al4V Open Porous Structures Produced by Additive Manufacturing,” *Adv. Eng. Mater.*, vol. 14, no. 6, pp. 363–370, 2012.

[7] S. R. Johnston, D. W. Rosen, M. Reed, and H. V. Wang, “Analysis of Mesostructure Unit Cells Comprised of Octet-truss Structures,” pp. 421–432, 2006.

[8] M. Smith, Z. Guan, and W. J. Cantwell, “Finite element modelling of the compressive response of lattice structures manufactured using the selective laser melting technique,” *Int. J. Mech. Sci.*, vol. 67, pp. 28–41, 2013.

[9] M. Suard *et al.*, “Mechanical equivalent diameter of single struts for the stiffness prediction of lattice structures produced by Electron Beam Melting,” *Addit. Manuf.*, vol. 8, no. September 2018, pp. 124–131, 2015.

[10] J. Kadkhodapour *et al.*, *Failure mechanisms of additively manufactured porous biomaterials: Effects of porosity and type of unit cell*, vol. 50, no. December 2018. Elsevier, 2015.

[11] L. J. Gibson, “Biomechanics of cellular solids,” *J. Biomech.*, 2005.

[12] I. Standard, “INTERNATIONAL STANDARD Mechanical testing of metals — Ductility testing — Compression test for porous and cellular

Stellenbosch University https://scholar.sun.ac.za

metals," *Int. Stand.*, vol. ISO 13314, no. 1, 2011.

[13] ASTM INTERNATIONAL, "ASTM F2792-12a," *Rapid Manuf. Assoc.*, pp. 1–3, 2013.

[14] T. DebRoy *et al.*, "Additive manufacturing of metallic components – Process, structure and properties," *Prog. Mater. Sci.*, vol. 92, pp. 112–224, 2018.

[15] "Bridging the gap with 3D printing." [Online]. Available: https://www.airbus.com/newsroom/news/en/2018/04/bridging-the-gap-with-3d-printing.html. [Accessed: 02-Jul-2018].

[16] A. du Plessis *et al.*, "Beautiful and Functional: A Review of Biomimetic Design in Additive Manufacturing," *Addit. Manuf.*, vol. 27, no. March, pp. 408–427, 2019.

[17] B. P. Conner *et al.*, "Making sense of 3-D printing: Creating a map of additive manufacturing products and services," *Addit. Manuf.*, 2014.

[18] S. Bremen, W. Meiners, and A. Diatlov, "Selective Laser Melting: A manufacturing technology for the future?," *Laser Tech. J.*, vol. 9, no. 2, pp. 33–38, 2012.

[19] A. du Plessis, "Effects of process parameters on porosity in laser powder bed fusion revealed by X-ray tomography," *Addit. Manuf.*, vol. 30, no. June, p. 100871, 2019.

[20] B. Vrancken, L. Thijs, J. P. Kruth, and J. Van Humbeeck, "Heat treatment of Ti6Al4V produced by Selective Laser Melting: Microstructure and mechanical properties," *J. Alloys Compd.*, vol. 541, pp. 177–185, 2012.

[21] L. Thijs, F. Verhaeghe, T. Craeghs, J. Van Humbeeck, and J. P. Kruth, "A study of the microstructural evolution during selective laser melting of Ti-6Al-4V," *Acta Mater.*, vol. 58, no. 9, pp. 3303–3312, 2010.

[22] L. E. Murr *et al.*, "Microstructure and mechanical behavior of Ti-6Al-4V produced by rapid-layer manufacturing, for biomedical applications," *J. Mech. Behav. Biomed. Mater.*, vol. 2, no. 1, pp. 20–32, 2009.

[23] L. Facchini, E. Magalini, P. Robotti, A. Molinari, S. Höges, and K. Wissenbach, "Ductility of a Ti-6Al-4V alloy produced by selective laser melting of prealloyed powders," *Rapid Prototyp. J.*, vol. 16, no. 6, pp. 450–459, 2010.

[24] P. Mercelis and J. P. Kruth, "Residual stresses in selective laser sintering and selective laser melting," *Rapid Prototyp. J.*, vol. 12, no.

Stellenbosch University https://scholar.sun.ac.za

5, pp. 254–265, 2006.

[25] B. Vrancken, L. Thijs, J. Kruth, and J. Van Humbeeck, “Heat treatment of Ti6Al4V produced by Selective Laser Melting : Microstructure and mechanical properties,” *J. Alloys Compd.*, vol. 541, pp. 177–185, 2012.

[26] F. W. Zok, R. M. Latture, and M. R. Begley, “Periodic truss structures,” *J. Mech. Phys. Solids*, vol. 96, pp. 184–203, 2016.

[27] V. S. Deshpande, N. A. Fleck, and M. F. Ashby, “Effective properties of the octet-truss lattice material,” *J. Mech. Phys. Solids*, vol. 49, no. 8, pp. 1747–1769, 2001.

[28] S. J. Li *et al.*, “Influence of cell shape on mechanical properties of Ti-6Al-4V meshes fabricated by electron beam melting method,” *Acta Biomater.*, vol. 10, no. 10, pp. 4537–4547, 2014.

[29] H. E. Pettermann and J. Hüsing, “Modeling and simulation of relaxation in viscoelastic open cell materials and structures,” *Int. J. Solids Struct.*, vol. 49, no. 19–20, pp. 2848–2853, Oct. 2012.

[30] S. Hyun, A. M. Karlsson, S. Torquato, and A. G. Evans, “Simulated properties of Kagomé and tetragonal truss core panels,” *Int. J. Solids Struct.*, vol. 40, no. 25, pp. 6989–6998, Dec. 2003.

[31] A. J. Jacobsen, W. Barvosa-Carter, and S. Nutt, “Micro-scale truss structures formed from self-propagating photopolymer waveguides,” *Adv. Mater.*, vol. 19, no. 22, pp. 3892–3896, 2007.

[32] G. W. Kooistra, V. S. Deshpande, and H. N. G. Wadley, “Compressive behavior of age hardenable tetrahedral lattice truss structures made from aluminium,” *Acta Mater.*, vol. 52, no. 14, pp. 4229–4237, 2004.

[33] V. S. Deshpande, M. F. Ashby, and N. A. Fleck, “Foam topology: Bending versus stretching dominated architectures,” *Acta Mater.*, vol. 49, no. 6, pp. 1035–1040, 2001.

[34] M. F. Ashby, *Metal foams : a design guide*. Butterworth-Heinemann, 2000.

[35] S. Vajjala, A. M. Kraynik, and L. J. Gibson, “A cellular solid model for modulus reduction due to resorption of trabeculae in bone,” *J. Biomech. Eng.*, vol. 122, no. 5, pp. 511–515, 2000.

[36] V. Weißmann, R. Bader, H. Hansmann, and N. Laufer, “Influence of the structural orientation on the mechanical properties of selective laser melted Ti6Al4V open-porous scaffolds,” *Mater. Des.*, vol. 95, pp. 188–197, 2016.

Stellenbosch University https://scholar.sun.ac.za

[37] R. Wauthle *et al.*, “Effects of build orientation and heat treatment on the microstructure and mechanical properties of selective laser melted Ti6Al4V lattice structures,” *Addit. Manuf.*, vol. 5, pp. 77–84, 2015.

[38] J. C. Maxwell, “L. *On the calculation of the equilibrium and stiffness of frames*,” *London, Edinburgh, Dublin Philos. Mag. J. Sci.*, vol. 27, no. 182, pp. 294–299, Apr. 1864.

[39] A. Du Plessis, D.-P. Kouprianoff, I. Yadroitsava, and I. Yadroitsev, “materials Mechanical Properties and In Situ Deformation Imaging of Microlattices Manufactured by Laser Based Powder Bed Fusion,” 2018.

[40] A. du Plessis, I. Yadroitsev, I. Yadroitsava, and S. G. Le Roux, “X-Ray Microcomputed Tomography in Additive Manufacturing: A Review of the Current Technology and Applications,” *3D Print. Addit. Manuf.*, vol. 5, no. 3, pp. 227–247, 2018.

[41] A. du Plessis, I. Yadroitsava, I. Yadroitsev, S. G. le Roux, and D. C. Blaine, “Numerical comparison of lattice unit cell designs for medical implants by additive manufacturing,” *Virtual Phys. Prototyp.*, vol. 13, no. 4, pp. 266–281, 2018.

[42] A. Plessis and S. G. Roux, “X-RAY MICRO-CT SUPPORTING THE SOUTH AFRICAN ADDITIVE MANUFACTURING COMMUNITY A. du Plessis 1* , S.G. le Roux 2,” no. November, 2018.

[43] A. Plessis, S. G. Roux, and M. Tshibalanganda, “Advancing X-ray micro computed tomography in Africa : Going far , together,” vol. 3, 2019.

[44] A. du Plessis, C. Broeckhoven, A. Guelpa, and S. G. le Roux, “Laboratory x-ray micro-computed tomography: a user guideline for biological samples,” *Gigascience*, vol. 6, no. 6, pp. 1–11, Jun. 2017.

[45] L. Schoeman, P. Williams, A. du Plessis, and M. Manley, “X-ray micro-computed tomography (μCT) for non-destructive characterisation of food microstructure,” *Trends Food Sci. Technol.*, vol. 47, pp. 10–24, 2016.

[46] P. J. Arrazola, A. Garay, L. M. Iriarte, M. Armendia, S. Marya, and F. Le Maître, “Machinability of titanium alloys (Ti6Al4V and Ti555.3),” *J. Mater. Process. Technol.*, vol. 209, no. 5, pp. 2223–2230, 2009.

[47] T. Tancogne-Dejean, A. B. Spierings, and D. Mohr, “Additively-manufactured metallic micro-lattice materials for high specific energy absorption under static and dynamic loading,” *Acta Mater.*, vol. 116, pp. 14–28, 2016.

Stellenbosch University https://scholar.sun.ac.za

[48] M. Helou and S. Kara, “Design, analysis and manufacturing of lattice structures: An overview,” *Int. J. Comput. Integr. Manuf.*, vol. 31, no. 3, pp. 243–261, 2018.

[49] R. Hedayati, H. Hosseini-Toudeshky, M. Sadighi, M. Mohammadi-Aghdam, and A. A. Zadpoor, “Computational prediction of the fatigue behavior of additively manufactured porous metallic biomaterials,” *Int. J. Fatigue*, vol. 84, pp. 67–79, 2016.

[50] G. Dong, Y. Tang, and Y. F. Zhao, “Simulation of Elastic Properties of Solid-lattice Hybrid Structures Fabricated by Additive Manufacturing,” *Procedia Manuf.*, vol. 10, pp. 760–770, 2017.

[51] K. J. Bathe, *Finite element procedures. Second edition*. 2006.

[52] “17.7. POST1 - Error Approximation Technique.” [Online]. Available: https://www.sharcnet.ca/Software/Ansys/16.2.3/en-us/help/ans_thry/thy_post7.html#postechniqprob. [Accessed: 27-Mar-2019].

[53] J. Pointer, “Understanding Accuracy and Discretization Error in an FEA Model,” *Int. ANSYS Conf.*, 2004.

[54] T. Fiedler, M. Taherishargh, L. Krstulović-Opara, and M. Vesenjak, “Dynamic compressive loading of expanded perlite/aluminum syntactic foam,” *Mater. Sci. Eng. A*, vol. 626, pp. 296–304, 2015.

[55] S. Y. Choy, C. N. Sun, K. F. Leong, and J. Wei, “Compressive properties of functionally graded lattice structures manufactured by selective laser melting,” *Mater. Des.*, vol. 131, no. March, pp. 112–120, 2017.

[56] Z. S. Bagheri, D. Melancon, L. Liu, R. B. Johnston, and D. Pasini, “Compensation strategy to reduce geometry and mechanics mismatches in porous biomaterials built with Selective Laser Melting,” *J. Mech. Behav. Biomed. Mater.*, vol. 70, pp. 17–27, 2017.

[57] S. L. Sing, W. Y. Yeong, F. E. Wiria, and B. Y. Tay, “Characterization of Titanium Lattice Structures Fabricated by Selective Laser Melting Using an Adapted Compressive Test Method,” *Exp. Mech.*, vol. 56, no. 5, 2016.

[58] V. Cain, L. Thijs, J. Van Humbeeck, B. Van Hooreweder, and R. Knutsen, “Crack propagation and fracture toughness of Ti6Al4V alloy produced by selective laser melting,” *Addit. Manuf.*, vol. 5, pp. 68–76, 2015.

[59] M. Shunmugavel, A. Polishetty, and G. Littlefair, “Microstructure and mechanical properties of wrought and Additive manufactured Ti-6Al-

Stellenbosch University https://scholar.sun.ac.za

4V cylindrical bars," *Procedia Technol.*, vol. 20, no. July, pp. 231–236, 2015.

[60] M. Shunmugavel, A. Polishetty, and G. Littlefair, "Microstructure and mechanical properties of wrought and Additive manufactured Ti-6Al-4V cylindrical bars," *Procedia Technol.*, vol. 20, no. July, pp. 231–236, 2015.

Stellenbosch University https://scholar.sun.ac.za

Appendices

Appendix A Yield criteria and hardening laws for dense part

Considering the Von Mises criteria as the failure criteria for both the dense and porous parts. If the part is subjected to triaxial compression, then the stress tensor is given as below,

$$\sigma = \begin{pmatrix} \sigma_{11} & \sigma_{12} & \sigma_{13} \\ \sigma_{21} & \sigma_{22} & \sigma_{23} \\ \sigma_{31} & \sigma_{32} & \sigma_{33} \end{pmatrix}$$

According to the Von Mises yield criteria, yield occurs when the von mises effective stress σ_e reaches the yield stress value σ_y

$$2{\sigma_e}^2 = (\sigma_{11} - \sigma_{22})^2 + (\sigma_{22} - \sigma_{33})^2 + (\sigma_{33} - \sigma_{11})^2$$

Where σ_{11}, σ_{22}, and σ_{33} are the principal stresses.

The hydrostatic stress is then given by

$$\sigma_h = \frac{1}{3}(\sigma_{11} + \sigma_{22} + \sigma_{33}) = \frac{1}{3}\sigma_{ii}$$

The stress tensor can be expressed in terms of its hydrostatic stress tensor, σ_h, (i.e. mean stress) and its deviatoric stress tensor, σ'_{ij}, (i.e. shear stress) as below,

$$\sigma = \begin{pmatrix} \sigma_h & 0 & 0 \\ 0 & \sigma_h & 0 \\ 0 & 0 & \sigma_h \end{pmatrix} + \begin{pmatrix} \sigma_{11} - \sigma_h & {\sigma_{12}}' & {\sigma_{13}}' \\ {\sigma_{21}}' & \sigma_{22} - \sigma_h & {\sigma_{23}}' \\ {\sigma_{31}}' & {\sigma_{32}}' & \sigma_{33} - \sigma_h \end{pmatrix}$$

$$\sigma_{ij} = \sigma_h \delta_{ij} + \sigma'_{ij}$$

Where δ_{ij} is the Kronecker delta symbol which equals 1 when $i = j$ and zero when $i \neq j$.

Considering an incompressible part, $\sigma_h = 0$, the von Mises effective stress is given

$${\sigma_e}^2 = \frac{3}{2}\sigma'_{ij}\sigma'_{ij}$$

Now considering the strain rate, $\dot{\epsilon}_{ij}$, we have

$$\dot{\epsilon}_h = \frac{1}{3}(\dot{\epsilon}_{11} + \dot{\epsilon}_{22} + \dot{\epsilon}_{33})$$

Where $\dot{\epsilon}_h$ is the hydrostatic strain rate.

The plastic strain rate tensor is given by

Stellenbosch University https://scholar.sun.ac.za

$$\dot{\epsilon}_{ij}{}^{p} = \dot{\epsilon}_{h}{}^{p}\,\delta_{ij} + \dot{\epsilon}'_{ij}{}^{p}$$

For an incompressible part, $\dot{\epsilon}_{h}{}^{p} = 0$, the von mises effective strain rate is given by

$$\dot{\epsilon}_{e}{}^{2} = \frac{2}{3}\,\dot{\epsilon}'_{ij}{}^{p}\,\dot{\epsilon}'_{ij}{}^{p}$$

The factor $\frac{2}{3}$ is introduced so that $\dot{\epsilon}_e$ is equal to the plastic strain rate of a tension and compression test on an incompressible part.

Now considering the Prandtl-Reus plastic flow theory, the yield criterion is given by

$$\Phi \equiv \sigma_e - \sigma_y \leq 0$$

The plastic strain rate $\dot{\epsilon}_{ij}{}^{p}$ is normal to the yield surface Φ in the stress space and is given as below, for an incompressible part,

$$\dot{\epsilon}_{ij}{}^{p} = \frac{\partial \Phi}{\partial \sigma_{ij}}$$

The hardening rate is then given by

$$\dot{\epsilon}_e \equiv \frac{\dot{\sigma}_e}{k},$$

where k is the hardening modulus, which is the slope of the uniaxial stress versus plastic strain curve.

All the equations above describe the yield behavior of a solid (dense) part

Stellenbosch University https://scholar.sun.ac.za

Appendix B Lattice structures design equations

Octet-truss lattice structure

Core unit cell

$$v_{octahedron} = 12\,Al\frac{\sqrt{2}}{2}$$

$$v_{diagonal\ strut} = \frac{12Al\sqrt{2}}{2}$$

$$v_c = v_{diagonal\ strut} + v_{octahedron} = 12\sqrt{2}Al$$

Side unit cell

$$v_{octahedron} = 12\,Al\frac{\sqrt{2}}{2}$$

$$v_{diagonal\ strut} = 7Al\sqrt{2}$$

$$v_s = v_{diagonal\ strut} + v_{octahedron} = 13\sqrt{2}Al$$

Vertex unit cell

$$v_{octahedron} = 12\,Al\frac{\sqrt{2}}{2}$$

$$v_{diagonal\ strut} = 9Al\sqrt{2}$$

$$v_v = v_{diagonal\ strut} + v_{octahedron} = 15\sqrt{2}Al$$

Edge unit cell

$$v_{octahedron} = 12\,Al\frac{\sqrt{2}}{2}$$

$$v_{diagonal\ strut} = 8Al\sqrt{2}$$

$$v_s = v_{diagonal\ strut} + v_{octahedron} = 14\sqrt{2}Al$$

$$\bar{\rho} = \frac{v_l}{v_{tot}}$$

$$v_l = 27\,v_c + 54\,v_s + 8\,v_v + 36\,v_e$$

$$v_{tot} = 125\,l^3$$

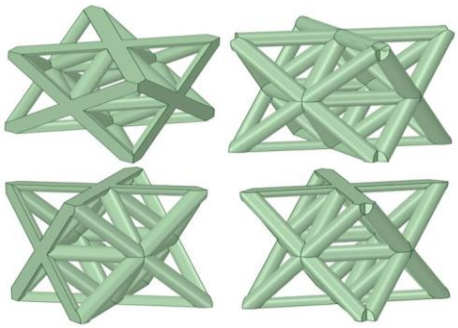

Diamond lattice structure

Stellenbosch University https://scholar.sun.ac.za

Core unit cell

$$\boldsymbol{v_{diagonal\ strut} = 16\frac{Al\sqrt{\sqrt{2}+1}}{4}}$$

$$\boldsymbol{v_c = 16\frac{Al\sqrt{\sqrt{2}+1}}{4}}$$

Side unit cell

$$\boldsymbol{v_{diagonal\ strut} = 16\frac{Al\sqrt{\sqrt{2}+1}}{4}}$$

$$\boldsymbol{v_s = 16\frac{Al\sqrt{\sqrt{2}+1}}{4}}$$

Vertex unit cell

$$\boldsymbol{v_{diagonal\ strut} = 16\frac{Al\sqrt{\sqrt{2}+1}}{4}}$$

$$\boldsymbol{v_v = 16\frac{Al\sqrt{\sqrt{2}+1}}{4}}$$

Edge unit cell

$$\boldsymbol{v_{diagonal\ strut} = 16\frac{Al\sqrt{\sqrt{2}+1}}{4}}$$

$$\boldsymbol{v_e = 16\frac{Al\sqrt{\sqrt{2}+1}}{4}}$$

$$\boldsymbol{\overline{\rho} = \frac{v_l}{v_{tot}}}$$

$$\boldsymbol{v_l} = 27\,\boldsymbol{v_c} + 54\,\boldsymbol{v_s} + 8\,\boldsymbol{v_v} + 36\,\boldsymbol{v_e}$$

$$\boldsymbol{v_{tot}} = 125\ l^3$$

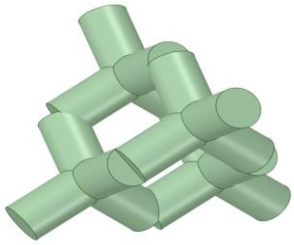

Stellenbosch University https://scholar.sun.ac.za

Appendix C Ti6Al4V chemical composition

Certificate of Analysis & Certificate of Conformity

PRAXAIR
SURFACE TECHNOLOGIES
1555 Main Street, Indianapolis, IN 46224

Product Name: TI-123-1
Customer:
Ship Date: 04/25/2019

Praxair Spec: 038021-BK
Shipping Order #: 915041899
Printed Date: 25/APR/2019

Item Number 038021-2K
Customer PO #: 116418

Lot Number: 52
Quantity: 30 UM: KG

All elements measured in weight percent unless otherwise specified. Sampling Method per ASTM B215.

Apparent Density	Test Method	Test Lab	Min	Max	Result	OK
Apparent Density (g/cm3)	ASTM B417	Praxair		Report	2.2	Yes
Chemistry	**Test Method**	**Test Lab**	**Min**	**Max**	**Result**	**OK**
Aluminum	XRF	Praxair	5.5	6.50	6.32	Yes
Carbon (total)	Leco	Praxair		0.08	0.01	Yes
Iron	XRF	Praxair		0.25	0.05	Yes
Hydrogen	Leco	Praxair		0.012	0.002	Yes
Nitrogen	Leco	Praxair		0.05	0.03	Yes
Oxygen	Leco	Praxair		0.13	0.11	Yes
Other Elements Each	XRF	Praxair		0.2	0.0	Yes
Titanium	By Diff	Praxair			Balance	Yes
Total All Other	XRF	Praxair		0.4	0.2	Yes
Vanadium	XRF	Praxair	3.5	4.50	4.06	Yes
Flow Rate	**Test Method**	**Test Lab**	**Min**	**Max**	**Result**	**OK**
Flow	ASTM B213	Praxair		Report	35.59	Yes
Mass (g)	ASTM B213	Praxair		Report	50	Yes
Microtrac per ASTM B822	**Test Method**	**Test Lab**	**Min**	**Max**	**Result**	**OK**
-20	ASTM B822	Praxair		10	10	Yes
Sieve per ASTM B214	**Test Method**	**Test Lab**	**Min**	**Max**	**Result**	**OK**
+270	ASTM B214	Praxair		5	2	Yes
Tap Density	**Test Method**	**Test Lab**	**Min**	**Max**	**Result**	**OK**
Tap Density (g/cm3)	ASTM B527	Praxair		Report	2.8	Yes

PST: 194429 C-124112

Spec ranges shown above in italics are target or nominal specifications only.

* indicates test is not required for routine acceptance.

** Denotes third-party materials testing laboratory accredited by Nadcap.

(317) 240-2650
Telefax (317) 240-2225
Toll-Free Telefax 1-800-234-6738 U.S.A

AS9100 Registered Quality System

This report is confidential and proprietary, and intended for the recipient of the product. If you receive in error you are prohibited from disclosing, copying, distributing, or using any of the information. The test report shall not be reproduced except in full, without the written approval of the laboratory. Please contact our office for instructions. The recording of false, fictitious, fraudulent statements or entries on the certificate may be punished as a felony under federal law. All elements measured in percent unless otherwise specified. Rounding is per ASTM E29.

Estimated uncertainty of measurement is available upon request. 1 of 2

Stellenbosch University https://scholar.sun.ac.za

Appendix D M2 Cusing machine specifications

M2 Cusing machine specifications	
Build envelope	250 x 250 x 280 mm (x, y, z)
Layer thickness	20 - 50 µm
Production speed	2 – 20 cm3/h (depending on material)
Laser system	Fibre laser 200 W (cw)
Max. scanning speed	7 m/s
Focus diameter	70 – 200 µm
Reference clamping system	EROWA, System 3R
Power consumption	7.0 kW
Power supply	3/N/PE AC 400 V, 32 A
Compressed air	5 bar
Inert gas consumption	< 2.5 m3/h
Dimensions	2440 x 1630 x 1992 mm (W x D x H)
Weight	1500 kg
Operating conditions	15 - 35°C

.

Stellenbosch University https://scholar.sun.ac.za

Appendix E CAD modeling of lattice structures

Modeling software: SpaceClaim

- Step 1

Creating unit cells for both 3D solid and 1D beam structures of a fixed unit cell length of 2 mm

1D beam structure

Under the Design tab, line bodies of the unit cell are created using the line command  , the new plane command  , and the coordinate system command 

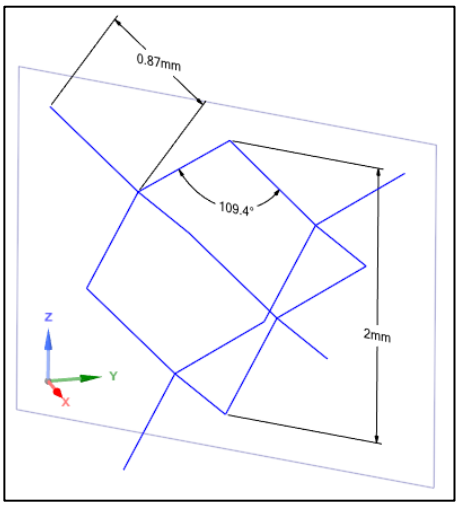

3D solid structure

Under the Design tab, 3D solid unit cell is created by using the same line bodies and either using the cylinder command 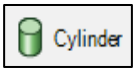

and assign the cylinder to the lines for the circular cross-section or by drawing a surface with the command  for the square cross-section or  for the circular cross-section which can then be extruded using the pull command 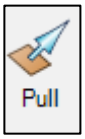

to create the solid structure.

Stellenbosch University https://scholar.sun.ac.za

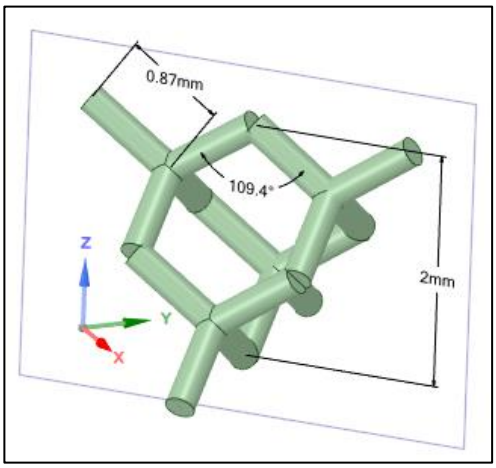

- Step 2

The pattern of the 3D solid and 1D unit cells through the linear pattern command  through a pitch distance of 2 mm 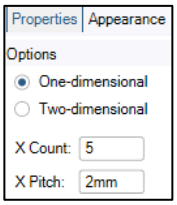

to obtain the lattice structure.

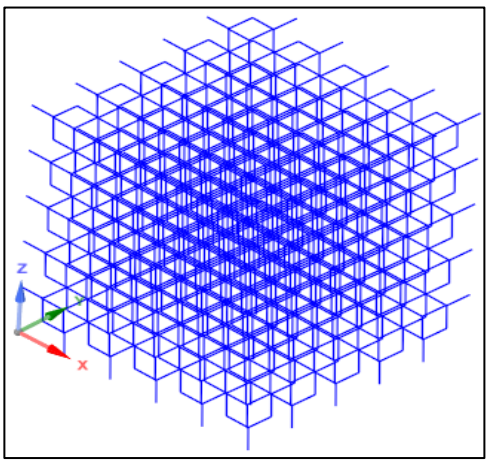

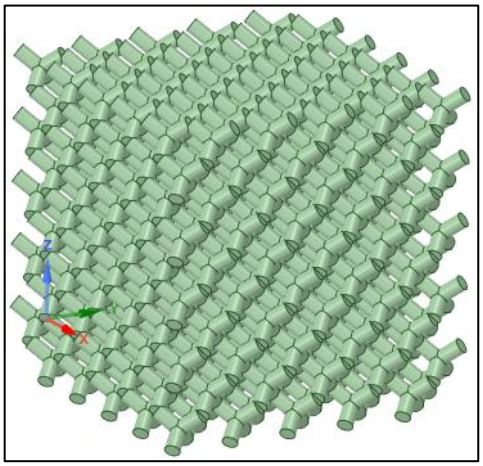

For the beam structure, under the Prepare tab, choose a beam cross-section under profiles 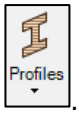

.and assign it to the line bodies using the create command 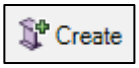

to obtain the beam structure.

Stellenbosch University https://scholar.sun.ac.za

Connect the beam with the connect command 

and under the Workbench tab, use the share command 

to share the topology.

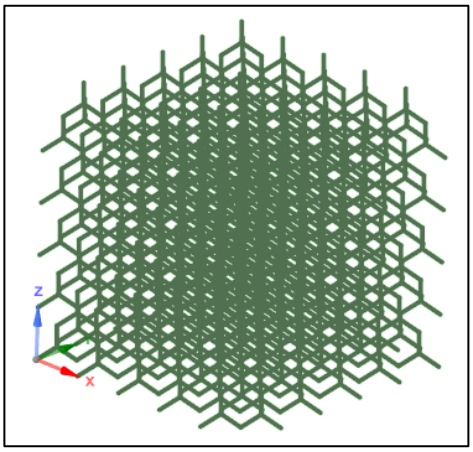

Under the Design tab, model the top and bottom platens. For the beam structure, under the Workbench tab, share the topology again for connection between the beam edges and the surface of the platens. For the solid structure, under the Design tab, use the combine command 

to merge the entire structure.

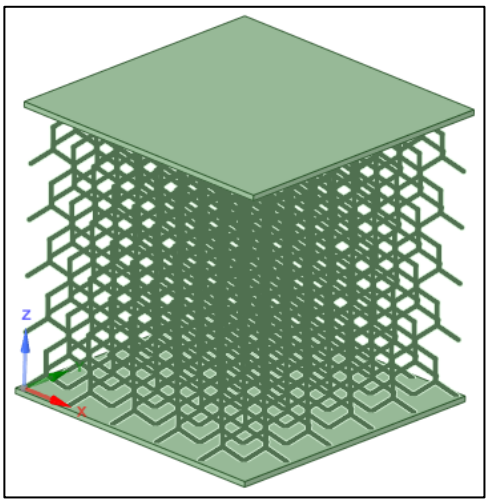

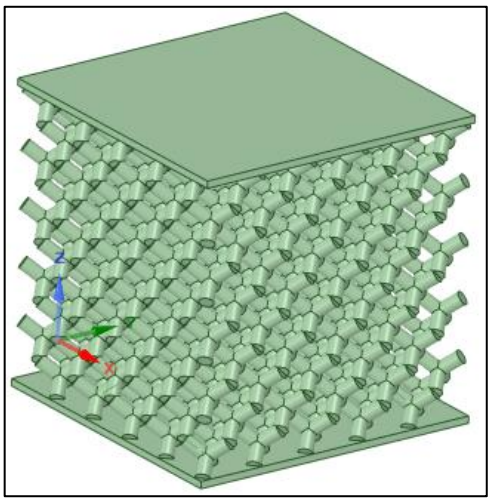

Stellenbosch University https://scholar.sun.ac.za

Appendix F Finite element simulation methodology

The following procedure was employed in conducting a non-linear static analysis.

Within the ANSYS Workbench environment, under the Analysis system, drag the static structural module, define material properties in Engineering data, import the CAD design under Geometry.

For the FEM Model, open Ansys Mechanical under Model

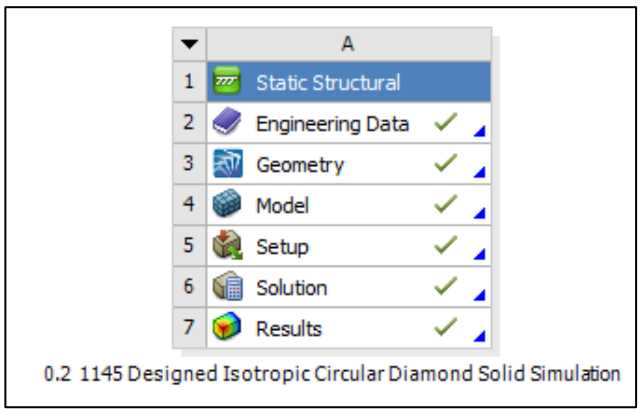

Within Ansys Mechanical, there is a model tree as seen below,

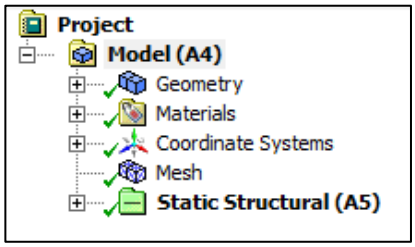

Proceed top to bottom.

Expand Geometry and select the CAD model by clicking on it. This allows, at the bottom left corner of the screen window, to switch material non-linearity on, as seen below,

Material	
Assignment	Titanium Alloy NL
Nonlinear Effects	Yes
Thermal Strain Effects	No

Under Mesh, chose the element type, element order, element size, and the physic preference, as seen below,

Stellenbosch University https://scholar.sun.ac.za

Defaults	
Physics Preference	Mechanical
Element Order	Program Controlled
Element Size	0.2 mm
Sizing	
Quality	
Inflation	
Advanced	
Statistics	

Under Static Structural, apply the boundary conditions by right-clicking on Static structural and choose the boundary condition and the load, and under Solution, select the desired solution of the simulation, as seen below,

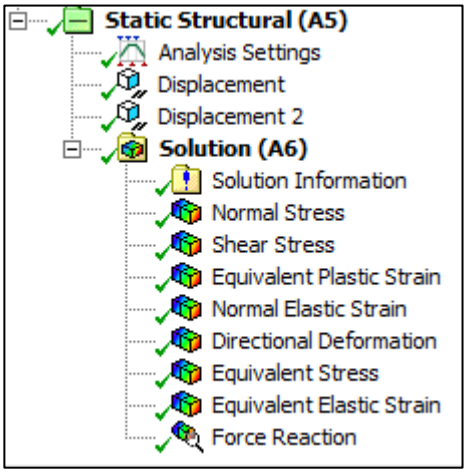

Under static structural, click on analysis settings, this where the solution process is set-up, settings such as the step controls which controls how often the matrix is updated; other setting such as the solver controls which controls the solver type and the stability of the stiffness matrix, also this is where geometric non-linearity is activated, as seen below,

Step Controls	
Number Of Steps	1.
Current Step Number	1.
Step End Time	5.e-002 s
Auto Time Stepping	On
Define By	Substeps
Initial Substeps	50.
Minimum Substeps	50.
Maximum Substeps	250.

Stellenbosch University https://scholar.sun.ac.za

Solver Controls	
Solver Type	Program Controlled
Weak Springs	Program Controlled
Solver Pivot Checking	Program Controlled
Large Deflection	On
Inertia Relief	Off

For the beam structure, the project tree include the cross-sections and the connections, as seen below,

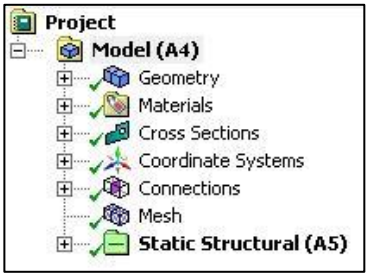

Under connections, create the connection between your objects, here we created a bonded connection between the top and bottom platens with the beam edges, as seen below,